Robust Optical Engineering for a Trapped Ion Quantum Computer

by

Ali Binai-motlagh

A thesis
presented to the University of Waterloo
in fulfillment of the
thesis requirement for the degree of
Master of Science
in
Physics (Quantum Information)

Waterloo, Ontario, Canada, 2022

Author's Declaration

I hereby declare that I am the sole author of this thesis. This is a true copy of the thesis, including any required final revisions, as accepted by my examiners.

I understand that my thesis may be made electronically available to the public.

Abstract

Trapped ions are one of the leading platforms for the implementation of quantum information processing (QIP), exhibiting one of the highest reported quantum gate and measurement fidelities. The challenge for the platform now is to maintain these high quality operations while expanding the system size beyond the $\sim$10-30 qubits that are available in today's devices. Currently we are near completion of the construction of our trapped ion quantum computer that will incorporate multiple isotopes of barium as qubits/qudits. Barium has several favourable properties that make it the ideal ion for QIP and the aim of our device in the near future is to develop this species into the premiere ion for QIP. The device in the future is hoped to serve as a cloud based resource for the Waterloo research community, fostering collaborations between algorithms, error correction and atomic physics researchers, that is ultimately hoped to expedite the development of trapped ion QIP. This thesis discusses the robust optical engineering that went into the construction of this trapped ion quantum computer. We describe the details of the continuous wave optical subsystems used for ion initialization, cooling, and measurements of the quantum states, including the imaging system used to collect ion fluorescence. In addition, this thesis discusses the unique individual addressing system that we have designed and built for performing single and two-qubit gates based on Raman transitions. With this system we attain a relative intensity crosstalk between neighbouring ions on the order of 10^{-4}. This is comparable to the best currently available implementations but our system provides additional optical frequency and phase control knobs that allow for more control over quantum simulation and computation experiments. Finally we will discuss the trap, its associated electronics and the vacuum system that houses our ions and atomic source.

Acknowledgements

The two years of my Master's were filled with many personal struggles heightened by the Covid-19 pandemic. Rajibul and the team's kindness and understanding helped me come out of the other end victorious and finish my thesis on time. Many brilliant people made my time at Waterloo memorable and productive. I want to thank Nik for helping me onboard into the group and catch up on the current state of the QuantumIon project. I want to thank both Nik and Matt for the awesome work they did on the individual addressing system before I took over. Thank you Nikhil for teaching me about RF electronics during our time working on the trap circuity. I wish for your swift recovery from the back injury and hope to see you back in peak physical form! Thank you Sainath (Ψ_0) for making the process of joining QITI lab seamless and for useful discussions and advice regarding the various experiments.

Thanks to everyone who participated in our weekly journal discussions, I certainly learned a lot from them. A huge thanks to Noah, with whom I worked most closely with on the QuantumIon project. We worked together on the CW optics, vacuum system, ablation target development and many other problems. It was a great pleasure working along and learning from you. The lab is in great hands with you, Hawking and Collin. I shall be back and we shall trap some ions together! Thank you Elijah for taking up the selfless act of making all those coax cables for the controls system. I wish you the best at your new job at Quantinuum.

Thank you Anthony for being a wonderful roommate, I'm certain you, Gilbert, Nikhil, Sainath, Monica and the rest of the Quantum Simulation team will do great things with the new Blade trap system. Thank you to Pei Jiang, Brendan and Yvette for sharing the qudit lab space with us when we had no where else to go. Special thanks to Yvette for accompanying me in our late night struggles through problem sets!

I wanted to pursue a career in physics ever since I learned about quantum physics and quantum information in high-school. So when the opportunity to work on building the QuantumIon trapped-ion quantum computer presented itself, I immediately seized it. I owe a huge debt of gratitude to my supervisor Rajibul Islam for bringing me into this project and giving me the great privilege of working on such a complex yet rewarding problem. I want to thank Crystal, my unofficial co-supervisor, for the useful discussions during our many meetings and for teaching the trapped-ion reading course from which I greatly benefited. Thank you to Professor Alan Jamison and Professor Raffi Budakian for taking the time to be a part of my Master's committee and reviewing this thesis.

Finally, a shout out to all the mechanical/mechatronics/electrical engineering undergraduates (Mark, Stephen, Levi, Tim, Nathan, Johan and Lana) for making this work

possible.

Dedication

To Sara.

Table of Contents

List of Figures x

List of Tables xviii

1 Introduction 1

1.1 Quantum Computing Platforms . . . 1

1.2 Review: Quantum Computing with trapped-ions . . . 2

1.3 The choice of ion . . . 6

1.4 The QuantumIon Project . . . 8

1.5 Thesis Outline . . . 9

2 Fundamentals of quantum computing with ions 10

2.1 Atomic source . . . 10

2.2 Trapping an ion . . . 12

2.3 Making a chain . . . 15

2.4 Cooling a chain . . . 18

2.5 Single qubit gates . . . 19

2.6 Two-qubit gates . . . 20

2.7 Analog Quantum Simulation . . . 26

2.8 Conclusion . . . 28

3 The CW and imaging subsystems 29

3.1 Overview of the CW light sources and their role 29

3.2 The trap 31

3.3 Optomechanical Design 32

  3.3.1 The laser rack 32

  3.3.2 Beam delivery boards 37

  3.3.3 Overview of the imaging system 43

3.4 Basic Manipulation of the Ba^+ ion 47

3.5 Beam delivery telescopes 52

  3.5.1 High dynamic range beam profiling 52

  3.5.2 Telescope design and characterization 54

3.6 Conclusion 58

4 The Raman individual addressing system 59

4.1 Coherent control with Raman transitions 59

4.2 Review of techniques for site-resolved addressing of ions 64

4.3 Raman System Overview 68

  4.3.1 The Global beam telescope 69

  4.3.2 FLDW Waveguide Splitter 70

  4.3.3 IA telescope 74

  4.3.4 The micro lens array 75

  4.3.5 Crosstalk Characterization 80

  4.3.6 System insertion loss 83

  4.3.7 Pulse Arrival times 84

4.4 Quantum dynamics 87

4.5 Conclusion 88

5 Vacuum system and Trapping Electronics 90

5.1 The Vacuum system 90

5.2 Generating Ultra-high Vacuum 91

5.3 The Vacuum Chamber 92

5.3.1 The Diagnostic chamber and the gauges 92

5.3.2 The Five-Way Cross and The Pumps 94

5.3.3 The Experimental Chamber 96

5.4 Heat Treatment of Vacuum Components 96

5.5 Trapping Electronics 99

5.6 Conclusion 102

6 Conclusion and Outlook 103

References 107

List of Figures

1.1 Comparison of the energy level structure of the two spin 1/2 isotopes of Barium and Ytterbium. Ytterbium diagram taken from [120]. 7

2.1 Energy level structure of neutral barium highlighting our two-step photoionization process using two lasers near 553 nm and 405 nm. Figure adapted from [116]. 12

2.2 (a) Ion positions for a chain of 10 ions in an axial potential with $\nu_z = 150$ kHz. The average spacing is $6.0 \pm 0.7\mu m$. (b) Frequency of the transverse (Radial) and axial normal modes for a chain of 10 ions with ν_z same as (a) and $\nu_{x,y} = 10\nu_z$. The axial modes have approximately equidistant frequencies while the radial modes bunch up together. (c) Graphical depiction of the normal mode eigenvectors $\boldsymbol{b}_m$ for the transverse direction. 17

2.3 Implementing the Controlled phase (top) and the CNOT gate (bottom) using an ion trap computer's native gate set. $s_{ij} = \pm 1$ denotes the sign of χ_{ij} which depends on what two ions in the chain are participating in the gate [37]. 23

2.4 Top: The detuning μ is placed half way between the center of mass and tilt radial frequencies of the chain. Bottom: Phase space trajectories for the two modes, resulting from the interaction in equation 2.19. By picking the gate duration $\tau = \frac{2\pi}{\delta} \cdot n$ where $n \in \mathbb{Z}^+$, both motional modes return to the origin in phase space. 24

2.5 (a) Position of the laser detuning (green) relative to all the axial modes of the chain participating in the interaction (red). (b) The 200 μs 11 segment pulse used to close the phase space trajectories at the end of the interaction. (c) The resulting phase space trajectories for two of the five modes. The colors of each curve segment is the same as the color of the corresponding pulse segment in (b). The black dot denotes the final position of $\alpha_{i,m}(t)$, which as desired is at the origin of phase space. The normal mode frequency and eigenvectors for these simulations were calculated using code written by Yi Hong Teoh. 25

2.6 Dependence of the J_{ij} matrix given in equation 2.30 for several detunings μ. The red vertical bars denote the radial frequencies and the black dashed lines denote the detunings. The rabi frequencies, Ω_i, are taken to be 500 kHz. The trapping frequencies are chosen to be 170 kHz in the axial direction and 3.5 MHz in the radial direction, for a chain of 10 ions. 28

3.1 Energy level structure of the 3 isotopes of barium that are used in our system. 30

3.2 (a) Optical image [141] and (b) Schematic [112] of the Pheonix trap. The blue region highlights the RF electrode and the red regions highlight the inner DC control electrodes. The inner electrodes have a pitch of 70 μm and the width of the slot in the quantum zone is 60 μm, providing a 0.25 NA opening for an optical beam. (c) Zoomed out image of the trap. 32

3.3 Overview of the experiment. The experiment is housed inside an environmental chamber that provides temperature and humidity stability. All the continuous wave lasers, modulators, doublers, and other optics are housed inside the laser rack. This light is delivered to the optics table, where the vacuum chamber resides, using several fiber cables. The electronics rack outside the environmental chamber holds components of the control system. Signals are exchanged between the experimental equipment (lasers, vacuum gauges, EOMs, AOMs, etc.) and the control system through patch panels in the wall of the environmental chamber. 33

3.4 (a) Setup used to fiber couple light from each of our CW lasers. The picture shown is for the 1107 nm laser (doubled to 553 nm). There are 3 other similar boards for 493, 650 and 1228 nm. The black and white graphics superimposed on the image are placeholders for missing equipment. (b) Optical schematic for the setup shown in (a). This was adapted from the schematic made by master's student Nikolay Videnov. 35

3.5 Schematic of the beam-prep drawer of the laser rack. The lines denote fiber optic cables, colored to reflect the wavelength of light propagating down each. The splitting is done using fiber based evanescent beam splitters. Light from each of the 4 CW lasers is brought to this drawer through fibers. EOMs add sidebands for addressing several transitions between hyperfine states simultaneously and the AOMs provide high bandwidth amplitude modulation. Part of the light from each laser is split off and sent to the wavemeter section of the rack for frequency stabilization. The sidebands of the EOMs are monitored using a set of scanning Fabry-Perot cavities. The light is then sent through fibers to several beam path on the optics table, to be then focused onto the ions. 37

3.6 (a) Board for focusing and positioning laser beams onto the ions. Light is delivered to each board through fibers from the laser rack. The board shown here delivers circularly polarized 493 nm light to the quantum zone and 405 nm light to the loading zone. The black and white graphics superimposed on the image are placeholders for missing equipment. (b) Optical schematic for the setup shown in (a). This was adapted from the schematic made by PhD student Noah Greenberg. 39

3.7 Left: Schematic of the experimental chamber and all the beams being focused onto ions in the loading zone (left) or quantum zone (right) of the trap. Right: Available NA at each of the three re-entrants windows. Re-entrants are used to bring the objectives as close as possible to the ions in-order to maximize the NA. Bringing the Raman re-entrants any closer would cause the CW beams entering through the other ports to clip the re-entrant. The proximity of the imaging re-entrant is constrained by the need of having a grounding shield around the trap. This is to nullify the effect of any stray fields at the ions due to charge build up on the window. 42

3.8 Schematic of our imaging system used to collect ion (493 nm) and neutral atom (553 nm) fluorescence. The beam at 650 nm is sent up through the imaging system and used for micromotion compensation. This figure was adapted from one made by Dr. Matt Day and master's student Nikolay Videnov. 43

3.9 Left: Details of the 493 nm arm of the imaging system, consisting of the imaging camera, PMTs and a fiber array for sending light from the ions to an array of avalanche photodiodes (fiber array stage and APDs currently missing from setup). Right: The 650 nm and alignment arms of the imaging system. The former we use for micromotion compensation by sending 650 nm light up to the ions and the latter we primarily use for detecting 553 nm neutral fluorescence during photoionization. 44

3.10 Details of the microscope objective alignment system. 45

3.11 Basic manipulation of the 133 and 137 isotopes of Ba^+. The blue (red) arrows denote the required sidebands for 493 nm (650 nm) light. 49

3.12 Positions of the hyperfine transitions in $^{133}\mathrm{Ba}^+$ (green) and $^{137}\mathrm{Ba}^+$ (purple) relative to the $^{138}\mathrm{Ba}^+$ transition frequency, ω_0. (a) Denotes the frequencies for the 493 nm transition. The transparent blue vertical lines, placed symmetrically about the carrier ($\omega = \omega_0$) denote the required sidebands, imparted by the EOM, for cooling $^{133}\mathrm{Ba}^+$. (b) Shows the required sidebands on the 650 nm repump transition for cooling $^{133}\mathrm{Ba}^+$. (c) Shows the required sidebands on the 493 nm transition if we instead wanted to cool $^{137}\mathrm{Ba}^+$, for comparison with (a). 51

3.13 Camera response as a function of laser beam power for several exposure times. The slope for each exposure time can be used to relate the intensity measured by the camera in ADU to physical units. This can then be used to stitch the profiles from each exposure time together into a single profile. 53

3.14 An example of a high dynamic range beam profile before and after calibration. 54

3.15 (a) Schematic of the achromatic cylindrical telescope used to elliptically shape the beam profile so that all 16 ions in the chain experience approximately the same intensity. This design is used for the loading, optical pumping and CRM beam paths. (b) Schematic of the telescope used for the second photoionization beam (405 nm). 56

3.16 (a) Beam profile of 650 nm and 493 nm light at the ion plane, focused by one of the achromatic cylindrical telescopes. Since the beam waist at the focus $\omega_0 \propto \lambda$, the 650 nm beam is larger. (b) Beam caustic near the ion plane, measured along the tightly focused direction (orthogonal to the chain). A fit to the data yields a Rayleigh range of 1.49 mm. (c) HDR cross-sections of the beam profile along (left) and orthogonal (right) to the ion chain. . . 57

4.1 (a) Simplified Ba^+ level diagram depicting how a Raman transition can be performed. (b) Pulse train and it's Fourier transform. The bandwidth of the pulse in frequency domain is inversely proportional to the duration of a single pulse, τ in the train. The period of the pulse train is the inverse of the repetition rate f_{rep}. f_{rep} gives the distance between the comb teeth in frequency domain. The width of each tooth is inversely proportional to f_{rep}/N where N is the number of pulses in the pulse train. 61

4.2 Raman transitions can be done by using a pair of detuned frequency combs generated by the same laser. By shifting one comb with respect to the other using a pair of AOMs, the beat note generated as the two beams interfere at the ions, can be made to satisfy the two-photon resonance. A typical comb has many more peaks than that depicted here. Our laser produces a 10 ps pulse train at a repetition rate of 104 MHz. This translates to around 480 comb teeth within the bandwidth of the light. 62

4.3 (a) By shining light on two specific ions in the chain, the Mølmer–Sørensen interaction can be used to implement a two-qubit unitary between those ions. (b) Control over the amplitude and frequency of each beam shining on the ions can be used to realize arbitrary spin models in any dimension. The graphs on the right show how a two-dimensional triangular lattice can be realized by turning on specific connections between the ions. 64

4.4 Previous implementations of individual addressing discussed in [46, 37, 108, 71, 122]. 67

4.5 Simplified schematic of our optical setup for using Raman transitions for site-specific coherent qubit manipulation. 68

4.6 (a) Schematic of the global Raman beam path focusing optics. (b) The resulting beam profile at the position of the ions. 70

4.7 (a) Schematic of the waveguide splitter chip [35]. Light is coupled on the right side into the waveguide, divided into 17 channels using a series of cascaded evanescent splitters and exits the waveguide on the left. (b) Image of the actual device used in the experiments. The piece of glass is around 2 cm in length. The device was designed by Dr. Matthew L. Day and manufactured by OptoFab at Macquarie University. 72

4.8 (a) Power out of each channel of the splitter chip for a range of temperatures. (b) Waveguide splitter chip inside a temperature-controlled case. On the right a microscope objective focuses light into the input waveguide mode and on the left the 17 fibers exit the case. The blue jacketed fibers are the 16 single mode fibers (PM460-HP) and the single white fiber at the end is the multi-mode fiber. The case is placed on a 3-axis linear translation stage with piezo motor control for alignment. 73

4.9 The individual addressing path telecentric imaging system. This is used to map the beam foci after the MLA, separated by 250 μm, to the 4 μm separation at the ions. 75

4.10 (a) Schematic of the chief (red) and marginal (purple) rays in object and image space. The optical invariant requires the product of these two quantities at conjugate planes to be conserved but this cannot be done using bulk optical elements. The pitch of the fiber array is 250 μm and the NA of each fiber is 0.1. In image space, the maximum available NA is 0.37 and the pitch between the ions is 4 μm. To satisfy the constraints we have on the beam in image space, we reduce the NA of the beams out of the fibers by using a series of microlenses placed at the facet of the fibers. (b) Image of the MLAs used in our IA setup. In the experiment, only a single row is used. Multiple rows were manufactured to account for fabrication inaccuracies. . 76

4.11 The optical invariant can be satisfied by using a FLDW pitch reduction waveguide. The low index contrast of laser written waveguides yields significant crosstalk at the required waveguide pitch so this solution was abandoned. Figure adapted from [137]. 77

4.12 (a) Theoretical/design surface profiles obtained from Zemax using equation 4.4. (b) Actual surface profiles of the manufactured lenses as measured by an optical profilometer. (c) Normalized difference between the radii of curvature of the designed and manufactured lenses. The manufactured lenses have a radii of curvature that is on average 2% shorter than the design, as indicated by the green line. 79

4.13 (a) Beam profiles measured after the MLA by imaging the beams with a single 250 mm focal length lens, providing a magnification of 0.5x, onto a camera. (b) Relative rabi rate of an unaddressed channel when the light on its nearest-neighbours are turned on. Due to the non-zero intensity at the location of the unaddressed ion, this ion also undergoes a slight Rabi rotation. An error of 1% corresponds to a rotation angle that is 100 times smaller compared to the addressed ions. (c) Simulated profile of one of the IA beams at the position of the ions, after the IA telecentric imaging system (62.5x demagnification). This was obtained using physical optics propagation in Zemax. (c) Actual beam profile at the location of the ions, measured using a camera with $\sim 1\ \mu$m $\times$ $1\ \mu$m pixels. The red horizontal line denotes where the intensity is at 10^{-4} of the peak and the black vertical bars denote positions that are 4 μm away from the peak. 82

4.14 (a) Insertion loss for the major components of the individual addressing system. (b) The power per channel (red) and the total insertion loss (black) as a function of the number of channels included in the IA system. The channels are placed in increasing order from best performing (highest output power) to worst performing (lowest output power). As channels are removed, the power per channel increases since the AOMs must compensate for a smaller variation in the optical power. 84

4.15 (a) Single pulse from the Raman laser measured using a fast photodiode and oscilloscope. The 10 ps pulses are broadened and asymmetric due to the limited bandwidth of both the oscilloscope and photodiode. (b) Images of the interference pattern formed when two channels from the VGA are sent through the IA telescope. The fringe contrast can be used as feedback for moving the fiber delay lines to improve temporal overlap between the two channels. 86

4.16 (a) Rabi frequency for single qubit gates driven by a pair of Raman beams in the lin-perp-lin configuration. Δ is the detuning from the $P_{1/2}$ excited state. The dashed red line denotes the position of our 532 nm pulsed laser and the two black lines denote the position of the $P_{1/2}$ and $P_{3/2}$ transitions. For our choice of laser frequency, power, and beam size, the rabi rate is around 0.9 MHz. (b) blue: The probability of spontaneous emission during a π pulse as a function of detuning. Black: The differential AC stark shift, in units of the rabi frequency. For our experimental parameters, the spontaneous emission probability is around 5e-6. This sets a fundamental limit on the possible gate fidelity. 88

5.1 left: Image of the exterior of our vacuum chamber. The top stainless steel Kimball chamber is where all the diagnostic equipment are mounted (extractor gauge, full range gauge and RGA). The five-way cross mounts the ion pump and TSP (not shown) at two of its ports and the two Kimball chambers at the other two. The final port is left blank. Right: Inside the experimental chamber, showing the trap, electric field shield, ablation targets and the imaging re-entrant. 94

5.2 Left: Stainless steel vacuum components involved in the medium temperature bake process. Right: The fully assembled prebaking setup. Several electrical heating tapes are used to control the temperature of the chamber. Each tape is wrapped near one thermocouple on the chamber and the temperature reading from these sensors are used as the feedback for temperature control. Aluminum foil and Fiberglass are used for thermal insulation. . . . 98

5.3 (a) Schematic of a helical coil resonator. The device consists of a larger coil, grounded at one end to a cylindrical shield surrounding it. A smaller coil is used to couple RF power into the circuit from an amplifier as well as to impedance match the 50 Ω resistance of the source to the trap. (b) Images of our resonator and (c) plot of the signal reflected from the resonator as measured on a spectrum analyzer. The resonance frequency is around 74 MHz. The dashed red line is used to mark the full width at half maximum (FWHM) point (-3 dB). The FWHM is around 217 kHz, yielding a Q factor of 340. 102

List of Tables

4.1 Radii of curvature of the design and manufactured lenses, along with the effective focal lengths of the fabricated lenses. 80

Chapter 1

Introduction

In the 20th century, the discovery of the laws of physics that govern the behaviour of matter at the atomic scale, led to what is now known as the first quantum revolution. This new understanding allowed the invention of devices such as lasers, transistors and solar cells that are now an inextricable part of our lives. Today, we are in the midst of a second quantum revolution where the behaviour of single quantum systems, rather than the average behaviour of many, are being explored and exploited to develop useful technologies [115]. The properties of coherence and entanglement of these individual quantum systems are being explored to build more secure cryptographic protocols for communication, sensors with precision beyond any classical device, and finally specialized computing devices known as quantum computers and simulators. These devices are poised to surpass modern classical computers on specific tasks such as simulation of quantum mechanical systems, computation of ground state energies of complex molecules and possibly problems in machine learning and artificial intelligence [55, 85]. Computational speed ups in these areas will help provide further insight into the laws that govern our universe as well as facilitate advancement in other areas of science such as biology and chemistry [100].

1.1 Quantum Computing Platforms

The research of Peter Shor, David Deustch and others, from over two decades ago, elucidated the potential of a computer that used the unique phenomena described by quantum mechanics as a resource [124, 123, 41]. This pioneering theoretical work sparked an initial attempt towards the construction of such devices. This effort has only intensified today and scientists are now working on many different competing platforms for performing quantum information processing. These include artificial atoms created from superconducting circuits [70], quantum dots [86], cold and trapped atoms or ions [81, 144], defects in crystals such as diamond or silicon [44, 78], and photons [13]. Of the platforms listed, trapped atomic ions and superconducting circuits are by far the most mature. Cirac and Zoller made the first proposal to use chains of trapped atomic ions for quantum computation [29]. In the same year, the Wineland group demonstrated single and two-qubit gates based on the Cirac-Zoller scheme [95]. A few years later, Nakamura et al. demonstrated single qubit control of the first superconducting qubit based on a cooper pair box [99]. Both platforms have moved beyond the demonstration phase and now there is an intense engineering effort, led by academic research labs as well as companies such as IonQ and Google, to simultaneously increase the number of qubits and the fidelity of quantum operations.

Currently we are in what has been dubbed the Noisy Intermediate Scale Quantum (NISQ) stage of this technology [109]. Intermediate scale refers to the fact that these devices possess only 10s of qubits. In contrast many of the useful algorithms that have sparked this field of research require more than one million qubits [109]. The term “Noisy” refers to the fact that quantum gates of current devices are imperfect, constraining the size of algorithms that can be run on current hardware. Because of these limitations, it is clear that near term discoveries on these devices will not be revolutionary in the broad sense however, advancements made at this stage on the hardware and algorithms that will run on the hardware will be a stepping stone towards the much coveted goal of an error corrected, fault tolerant quantum computer. Test-bed devices that allow the research community to quickly try out their ideas and algorithms will be instrumental to this goal. This thesis focuses on the construction of a small universal quantum computer, based on trapped atomic ions. We call this project QuantumIon and hope that this device will in the future serve as such a test-bed for the Waterloo research community.

1.2 Review: Quantum Computing with trapped-ions

In this section I will review the state of the art demonstrations of the elements of quantum information processing with trapped ions, including work and ideas on scaling the platform to large numbers of ions.

There are now several companies, including Google, IBM, Rigetti computing, Honeywell and IonQ that offer cloud-based access to their NISQ devices. These companies seldom release information about the inner workings of these devices and users have no access to hardware-level information. The eventual goal of the QuantumIon project is to build an open-access, remotely operable trapped-ion quantum computer. Open-access means that researchers will have free access to the device and importantly, the underlying hardware will be transparent to the users which can facilitate the design of hardware specific algorithms that are resilient to noise.

With one of the longest coherence times, highest fidelity state measurement and qubit operations, trapped-ions are a promising platform for scaling quantum computers into useful devices. To date, the longest coherence times, without the use of dynamical decoupling techniques, have been demonstrated with $^{43}\mathrm{Ca}^+$ ions [56]. The qubit, encoded in the hyperfine clock states of the $\mathrm{S}_{1/2}$ manifold was shown to have a memory coherence time of 50 s at room temperature. T_1 times for qubits encoded in two hyperfine levels of an ion are practically infinite due to the small spontaneous emission rate of these states. Decoherence is predominantly caused by magnetic field noise [139, 138, 129]. Other sources include heating of ion motional modes, leakage of microwave radiation and laser light, as well as phase noise in the microwave and laser fields used for quantum operations [138]. With the use dynamical decoupling, Wang et al. have extended the coherence times to more than one hour [138] in $^{171}\mathrm{Yb}^+$ hyperfine qubits. In addition to dynamic decoupling, to get such large coherence times, the authors surrounded their chamber with μ-metal magnetic field shielding to attenuate noise primarily from AC power lines, used $\mathrm{Sm_2Co_{17}}$ permanent magnets instead of coils, and sympathetically cooled the $^{171}\mathrm{Yb}^+$ memory qubit with a simultaneously trapped $^{138}\mathrm{Ba}^+$ ion.

Two qubit gate times in trapped ion systems can take up to a few hundred microseconds [14, 117], much longer than those in superconducting qubits which are on the order of 10-100 ns [69]. However, the roughly 100 μs coherence time of the widely used transmon qubit [69] limits the number of operations that can be executed within the coherence time of the qubit to around 10^4. For ions this is on the order of 10^6 [129]. The highest single qubit gate fidelitiy (99.9999%) has been demonstrated in $^{43}\mathrm{Ca}^+$ using microwave circuitry built into the trap [56]. The highest fidelity Raman-based single and two qubit gates have been reported in $^{9}\mathrm{Be}^+$ with a value of 99.996% and 99.91% respectively [49]. Similar figures have been reported in $^{43}\mathrm{Ca}^+$ with a value of 99.99% and 99.9% respectively [14]. A great advantage of ions compared to other platforms is that the long range coulomb interaction provides a fully connected interaction graph [84]. This means that each qubit or ion is connected to all other qubits in the system and entangling gates can be performed between arbitrary pairs of qubits. In contrast, superconducting qubits only possess nearest neighbour interactions. While this is sufficient for universal quantum computation, it necessitates the use of multiple SWAP operations to implement an equivalent two qubit operation that can be done in a single step with ions [17]. These additional operations can significantly reduce the fidelity of algorithms run on NISQ devices.

In terms of state preparation and measurement (SPAM), a fidelity of 99.93%, with a collection time of 11 μs, has been demonstrated using a ^{171}Yb^{+} hyperfine qubit. The authors achieved such fast detection times by using high numerical aperture (NA) collection optics and superconducting nanowire single photon detectors (SNSPDs) for detection [31]. The highest SPAM fideilities have been reported in ^{133}Ba^{+} (99.97%) [27] and ^{171}Yb^{+} (99.98%) [111] using the shelving detection method (see chapter 3). The researchers used relatively low NA optics and thus in the former case, required a relatively long collection time of around 4.5 ms for detection [27]. In the ^{171}Yb^{+} demonstration, dissipation via an E2 transition ($D_{5/2}$) from the $S_{1/2}$ manifold was used to prepare the very long lived ($\tau \sim 2$ years) $F_{7/2}$ state. The detection time in this case was instead limited by the time required to prepare the $F_{7/2}$ state ($\sim$ 100 ms). These fidelities were very recently surpassed by another barium isotope, ^{137}Ba^{+} (99.991 %) [12]. These operation infidelities are already lower than the $\sim$1% threshold for surface error correcting codes [48]. However, the overhead in terms of the number of physical qubits necessary to implement one logical qubit is a strong function of the error rate [48] so even higher operation fidelities should be sought after.

It should be noted that these cited state of the art demonstrations involve only a single or a few ions in a trap. For scalable quantum information processing, control over a larger number of ions is necessary. Currently, even with a modest number of ions in a chain, the fidelities drop significantly. For example, the two-qubit gate fidelity on IonQ's 11 qubit computer is 97.5% on average [144]. So the challenge now is to increase the number of ions while maintaining, if not exceeding, the high quality of quantum operations that have been demonstrated.

Ion trap QIP devices cannot be scaled by arbitrarily increasing the number of ions in a single trap for several reasons. (a) For a fixed axial trapping potential, as more ions are added the ion-ion separation decreases. Since the spacing in small traps of 10-20 ions is already small (around 3-5 μm), decreasing this further by adding more ions will make low cross-talk individual optical addressing of ions difficult. On a similar line, site resolved measurement will become difficult not only because of limits of the focusing optics, but also because fluorescence from the measured ion can decohere the information in its neighbours unless the information is shelved to some state far off resonance from the fluorescence. (b) The number of shared motional modes is proportional to the number of ions in the trap. For large N, the crowding of motional modes will make the stray excitation of unwanted modes more likely, thereby lowering the fidelity of entangling gates. Further, this crowding makes ground state cooling more difficult as there are more modes that need to be cooled. (c) The ion-motion coupling, characterized by the lamb-dicke parameter η, scales as $\frac{1}{\sqrt{N}}$. The weaker this coupling, the longer the gate times for a fixed rabi frequency and trapped-ion gate times are already relatively slow.

The obvious solution to this is to use many disjoint traps with a manageable number of qubits. Currently there are two techniques used to achieve inter-trap communication/entanglement. The first, dubbed the Quantum Charge Coupled Device (QCCD), stores multiple chains in a complex trap with many DC electrodes [67]. These electrodes are used to shuttle ions around in the trap, split off a chain or re-order ions through rotations [130, 18]. In this way, a series of small and separated chains can be created, where the high fidelity of quantum operations that have been reported in small chains can be preserved and performed simultaneously in each chain. If an ion needs to be measured, it is split off from the rest of the chain, and the operation can be done without perturbing the rest of the ions. Sympathetic cooling is used to remove heat from the memory ions that has accumulated during transport. For example, reference [107] pairs up a $^{171}\mathrm{Yb}^+$ hyperfine qubit with a $^{138}\mathrm{Ba}^+$ ion that acts as a coolant, performing Doppler and resolved sideband cooling.

Such an architecture will allow the construction of quantum processors with about 1000 ions, limited by the complexity of the controls required to quickly shuttle ions between different traps, the time it takes to distribute quantum information across a large device through shuttling, and the number of laser beams that can be sent through the device while avoiding significant diffraction [20].

To go beyond this limit, photons can be used to mediate communication between different trap modules which could be a QCCD device, consisting of multiple trapping zones on a single chip or a single linear chain [96]. In this scheme, the ions are divided into two categories: "communication" qubits that are involved in the photon mediated entanglement between devices and "memory" qubits that are used to store and manipulate quantum information within a single device. To entangle a pair of communication qubits in each trap, first a pair of pulsed lasers are used to induce each ion to emit a single photon by driving the qubit to a short lived excited state. Based on selection rules, the frequency or polarization of the emitted photon depends on whether the qubit was in $|0\rangle$ or $|1\rangle$ and this can be used to entangle the internal state of the ion with the frequency or polarization of the emitted photon after appropriate polarization filtering. Interfering the photon from the two communication qubits at a beam splitter allows the transfer entanglement from ion-photon to ion-ion, heralded by simultaneous detection at the output ports of the beam splitter [104, 32]. With current photon scattering rates, collection and detection optic efficiencies, ion-ion entanglement can be generated in a few milliseconds [23].

To make this scheme viable, one needs a way of separating out the communication and memory qubits, so as to avoid degradation of the information stored in the memory qubits during entanglement generation. This can be done by separating the two types of ions in space via shuttling, or by using two different species of ions for each task. The latter limits cross-talk by separating out the energy scales of the two types of ions. Such dual species approaches face several problems: (a) To be able to manipulate each species independently, roughly twice as many lasers are required. (b) The vacuum system needs to be designed with multiple sources in mind. (c) The transverse normal mode spectrum of the chain decouples into two sets, one where ions of one mass are strongly coupled and another where ions of the other mass are strongly coupled (the axial mode is less affected by this mismatch) [128, 36]. (d) The motional mode spectrum is dependent on the order of the ions in the chain and can be modified due to ion re-ordering events caused by collisions with background gasses. This decoupling makes efficient sympathetic cooling and interspecies entangling gates difficult due to the excessive power requirements needed to generate sufficient spin-motion entanglement [128].

One way around this is to use mixed-isotope chains. In this case only lasers for a single ion species are required and the smaller mass difference means that the transverse modes exhibit better participation from both species [36]. A third recently proposed solution uses only a single isotope of one ion. The spectral separation between communication/coolant and memory qubits is attained by dynamically changing the way a qubit is encoded in a single ion. In a single ion, a qubit can be encoded in the hyperfine ground states ("g-type" ion) or metastable states ("m-type" ion) of the ion. It can also be defined between the ground and metastable states, coupled via an optical transition ("o-type" ion). This scheme is referred to as the "omg" architecture [11]. For example, when a chain is to be sympathetically cooled using a g-type ion or a g-type ion is to be measured, storing the memory qubits using a pair of hyperfine states in the metastable manifold can prevent decoherence of this state by light scattered during the cooling or measurement process. Since the motional mode coupling is independent of which internal states of the ion are used to encode the qubit, the problems associated with multi-species chains are removed [11].

1.3 The choice of ion

For an ion to be useful for QIP, it should satisfy several requirements. Such an ion should possess two levels that can be used to define a high quality qubit. That is, they should have long lifetimes, high coherence times and be accessible for coherent control through external control fields. The ion should also have a third short lived level that is coupled to the qubit through an optical transition. This level is used for optically pumped state preparation and measurement through the detection of light scattered from this third level. These constraints significantly reduce the choice of elements to a handful of species [97, 131].

The list of ions that have been trapped and cooled thus far include Be$^+$ [53], Mg$^+$ [148], Ca$^+$ [108], Sr$^+$ [90], Ba$^+$ [26], Yb$^+$[104], Cd$^+$ [76], Hg$^+$ [21], Lu$^+$ [66], Al$^+$ [54] and In$^+$ [22]. Qubits can be encoded in the hyperfine or Zeeman sublevels of a ground or long lived metastable state of ions. For these two encoding, coherent manipulation can be done using microwave or radio frequency fields. Optical manipulation can be achieved through raman transitions using a third level that is optically coupled to the qubit. Another common encoding uses the ground state and a metastable state of the ion to define the qubit. The energy separation between such states is large enough to enable direct optical control. Restricting our search to ions with easily accessible transitions removes all the group 12 element candidates as well as Magnesium since these ions involve transitions in the deep UV. The highest fidelity operations have been demonstrated with qubits defined in the hyperfine structure of ions [56]. So if we narrow our focus to ions with the simplest hyperfine structure (spin 1/2 nucleus) that also possess long-lived metastable D or F states as well as easily accessible transitions, we can trim this list to only two ions: Barium and Ytterbium. The energy level diagram for the spin-1/2 isotope of both species is shown in 1.1.

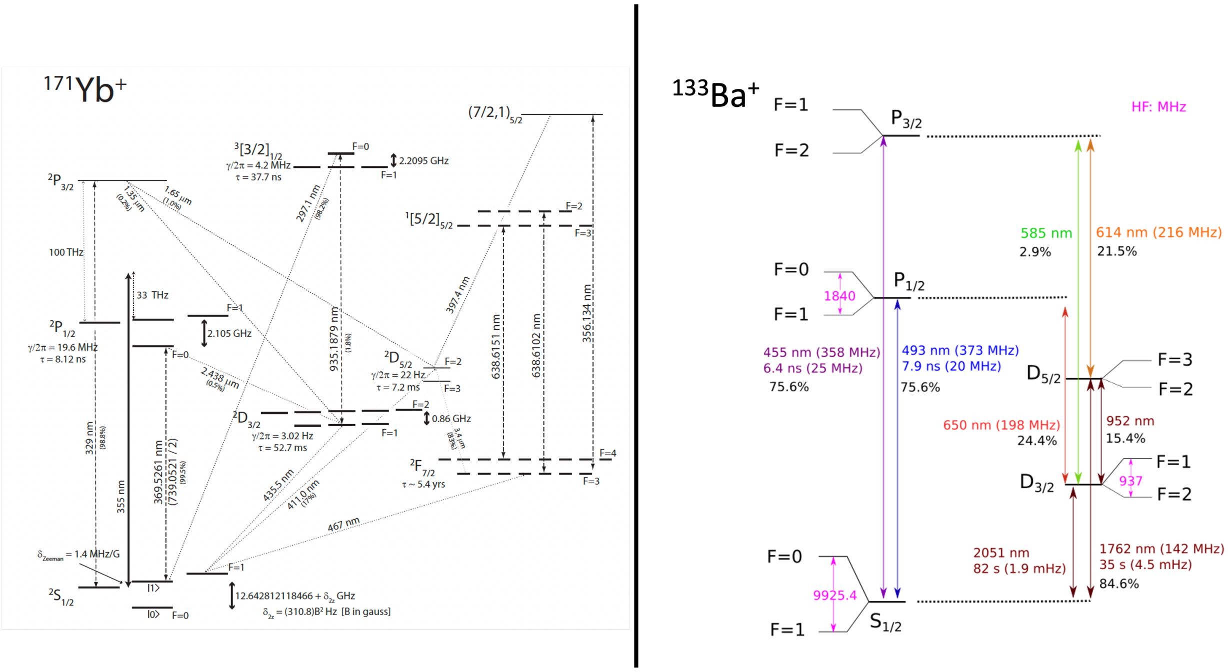

Figure 1.1: Comparison of the energy level structure of the two spin 1/2 isotopes of Barium and Ytterbium. Ytterbium diagram taken from [120].

Of these two choices, we decided on $^{133}\mathrm{Ba}^+$ for the following reasons: (a) The lasers required to address the relevant transitions in the ion are closely packed in the visible region of the spectrum with a few present in the near IR. This allows us to combine multiple wavelengths into a single fiber for delivering light to the ions, reducing the footprint of the setup. It also makes optical design easier as aberrations are more significant at shorter wavelengths. (b) With a spin 1/2 nucleus, it possesses the simplest possible hyperfine structure and qubits can be encoded in the magnetic field insensitive ($m_F = 0$) "clock states" of $\mathrm{S}_{1/2}$ ground state. (c) It possesses long-lived $\mathrm{D}_{3/2}$ and $\mathrm{D}_{5/2}$ metastable states with lifetimes on the order of 10s of seconds. In comparison, these lifetimes are on the order of milliseconds in Yb^+. These states can be used to encode a second qubit, in the corresponding hyperfine clock states, or a qudit in the many Zeeman sublevels. These advantages have also persuaded IonQ, one of the leading Quantum Computing companies, to make the switch to $^{133}\mathrm{Ba}^+$ [8].

1.4 The QuantumIon Project

While $^{133}\mathrm{Ba}^+$ possesses several advantages over $^{171}\mathrm{Yb}^+$ that make it a better choice for quantum information processing, it has not yet seen wide-scale adoption by the community. $^{133}\mathrm{Ba}^+$ is a synthetic radioactive isotope of barium with a half-life of around 10.5 years [26]. For this reason only a small amount of it ($< 10\ \mu$g in our case) can be used for loading ions. This makes the robust, efficient loading of long ion chains difficult. As a result, loading of long chains of this species, for the purpose of QIP has not yet been demonstrated. Our short term goals are to develop procedures for the trapping of $^{133}\mathrm{Ba}^+$ that allows for efficient loading of long chains and more generally makes this ion species easier to work with. Once this is fleshed out, our plan is to demonstrate the building blocks of quantum computation such as high fidelity site-selective qubit measurement and single and two qubit gates on arbitrary ions or ion pairs. In addition to a $^{133}\mathrm{Ba}^+$ source, we have included a natural abundance Barium target in the chamber as well. This will be used to load two other isotopes of Barium, namely $^{137}\mathrm{Ba}^+$ and $^{138}\mathrm{Ba}^+$. This will allow us to load chains of ions consisting of multiple isotope of Barium, enabling us to explore ways of making multi-isotope entangling gates more robust in practice. Further, while many of the primitives of the omg architecture have been demonstrated, entanglement between m-encoded qubits has not yet been shown. This is another question we can address with our system.

Another possible direction for the project is to explore the use of qudits for trapped-ion QIP. Beyond increasing the number of ions in a chain, another way of growing the dimensionality of a quantum processor's Hilbert space is to use qudits. A qu***d***it is a generalization of a qubit where each computational unit consists of more than two states. This is a natural generalization for atoms due to the many easily accessible hyperfine and zeeman levels [113]. ^{137}Ba^{+} is a particularly apt choice for this because its 3/2 nuclear spin provides a ground state $S_{1/2}$ manifold with up to 8 levels to encode the qudit. Further, the long-lived $D_{5/2}$ state provides a way of measuring the state of the qudits with high fidelity [19]. The QuantumIon machine has the capacity to address all these research questions and more. This thesis focuses on the build up of all the optical sub-systems that make these applications possible.

1.5 Thesis Outline

I will begin with a theoretical description of quantum computing with trapped ions in chapter 2. My main contributions to this project include the construction of the optical systems necessary for ion trapping, cooling, qubit initialization and measurement. These systems will be discussed in chapter 3. Chapter 4 discusses our unique scheme for performing single and two-qubit entangling gates on arbitrary pairs of ions. I was also involved in the construction of the ultra-high vacuum chamber built for the project. This, along with my work on the circuitry necessary for trapping ions will be discussed in chapter 5.

Chapter 2

Fundamentals of quantum computing with ions

This chapter provides an overview of the trapped-ion platform and how it can be used for quantum computation and simulation. We will start with how ions are trapped and prepared into a chain, and then discuss how this chain forms a universal quantum computer or an analog quantum simulator.

2.1 Atomic source

Atoms are loaded into a trap typically either through laser ablation or by an oven. In the oven approach, a chunk of the element of interest is placed into a stainless steel or tantalum tube inside the vacuum chamber. Current running through a piece of wire wrapped around the tube heats the element to the point of sublimation [51]. This sublimated cloud is then directed towards the electrodes of the ion trap. In the ablation approach, a pulsed laser beam is focused onto a specific spot on a target made from the element of interest to locally create a sublimated cloud. The orientation of the ablation beam does not matter, the directionality of the cloud is determined by the orientation of the surface normal of the target. The process of heating and cooling an oven to or below the sublimation point takes on the order of minutes so loading in this way is slow. It is also wasteful since the entire chunk of the element is heated up and it takes some time for the chunk to cool below the sublimation point, resulting in a large amount of atomic flux directed towards the trap, even after the desired ions have been loaded. On the other hand, loading with ablation is nearly instantaneous. Since only a small spot on the surface of the target is heated, the atomic flux is less dense and thus not as wasteful. One problem with ablation is that the laser pulse may have enough energy to also ionize the ablated atoms. This means that a second ionization step would not be required but it also makes isotope selectivity difficult. The laser power can be optimized to minimize ion generation while still creating a sufficiently dense plume of atoms [140]. In our experiments we only use laser ablation because the radioactive nature of $^{133}\mathrm{Ba}^+$ means that we can only have a small amount of it in our chamber and cannot afford to be wasteful.

Once a cloud of neutral atoms in the direction of the trap electrodes has been produced, the next step is to ionize a subset so that they can interact with the electric fields of the trap. This is most commonly done through photoionization as it can be isotope selective but ions can also be generated through electron impact [116]. To generate ions through photoionization we use a 1+1 resonance-enhanced multi-photon ionization scheme (REMPI) where a laser resonant with the $6s6p\ ^1P_1$ transition near 553 nm is used to excite the atom into that state and then a laser with wavelength shorter than 417 nm is used to eject the electron into the continuum [79]. We use a 405 nm laser for the second step. Since the second step is not a resonant process, the laser does not need to have a narrow bandwidth or be stabilized. The isotope shifts on the $6s6p\ ^1P_1$ line can be used to select only a specific isotope of barium to be ionized. In this way we can choose which isotope we load into the trap. There are many other paths to photoionization, for example, a single laser with wavelength shorter than 238 nm can be used or a 1+1 REMPI using a single 413 nm laser, with the $6s^2\ ^1S_0 \rightarrow 5d6p\ ^3D_1$ inter-combination transition as the intermediate step, can be used. The former is not isotope selective and the latter is a weak transition so they were not considered [116]. These transitions are highlighted in figure 2.1.

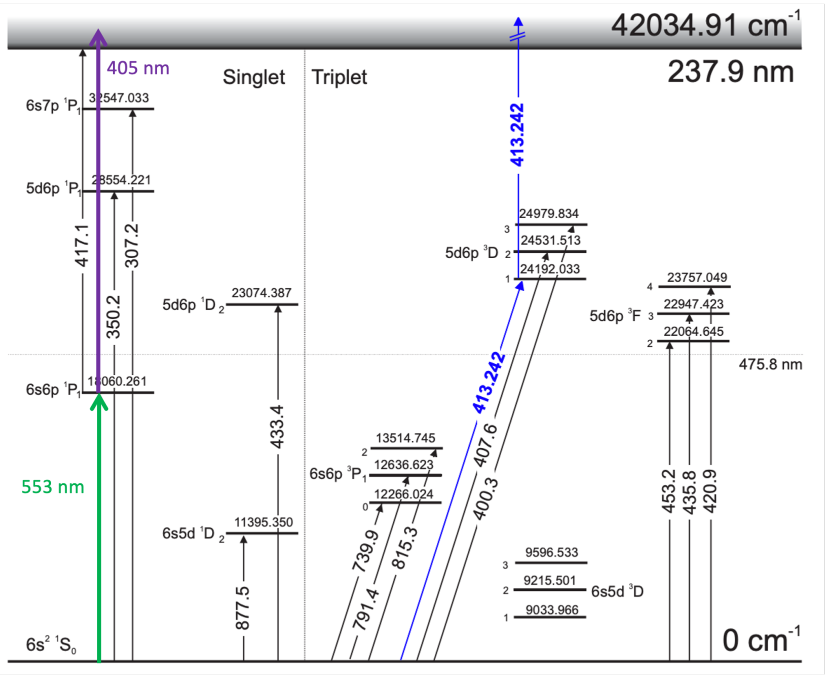

Figure 2.1: Energy level structure of neutral barium highlighting our two-step photoionization process using two lasers near 553 nm and 405 nm. Figure adapted from [116].

2.2 Trapping an ion

Solutions to Laplace's equation, $\nabla^2 V = 0$, only admit extrema at its boundaries and thus a static electric field cannot be used to trap charges in all three spatial dimensions. However, by combining static and time-dependent voltages, an effective time-average potential can be generated that is confining in all three dimensions; this is called a Paul trap. A typical Paul trap consists of two pairs of rods. A radio frequency voltage is applied to a pair of them and the other pair are grounded. This provides dynamic confinement perpendicular to the axis of the rods. To get confinement along the rod's axis, a static voltage can be applied to a pair of end cap electrodes. This configuration is called a 4-rod linear Paul trap. There are many different types of Paul traps but most create an approximately quadrupolar electric potential of the form:

$$\phi(x,y,z,t) = \frac{U}{2}(\alpha x^2 + \beta y^2 + \gamma z^2) + \frac{V}{2}(\alpha' x^2 + \beta' y^2 + \gamma' z^2) \cdot \cos(\Omega_{rf} t) \tag{2.1}$$

consisting of a static component and a dynamic component oscillating at Ω_{rf}, resulting from the radio frequency voltage applied to a pair of the electrodes. The coefficients $\alpha, \beta, \gamma, \alpha', \beta', \gamma'$ depend on the exact geometry of the trap. The Newton's equation of motion for a particle of mass m and charge e in this potential is given by $m\ddot{x}_i = -e/m\frac{\partial\phi}{\partial x_i}$. Since the equations are decoupled from each other and all have the same form, we'll only consider the x component:

$$\ddot{x} = \frac{-e}{m}(U\alpha + V\alpha'\cos(\Omega_{rf}t))x \tag{2.2}$$

With the change of variable $\eta \equiv \frac{\Omega_{rf}t}{2}$, this equation can be put into the form of the extensively studied Mathieu Differential Equation:

$$\frac{d^2x}{d\eta^2} + \big(a_x - 2q_x\cos(2\eta)\big) = 0 \tag{2.3}$$

where $a_x = \frac{4eU\alpha}{m\Omega_{rf}^2}$ and $q_x = \frac{2eV\alpha'}{m\Omega_{rf}^2}$. The values of a_x and q_x determine whether the trajectories of the ion are stable, i.e. remain bounded for all time and are thus called stability parameters. In the case where $a_x, q_x << 1$, which is the regime in which most ion trapping experiments operate, the trajectories are stable and the ion's motion is approximately given by:

$$x(t) = 2A\cos(\beta_x\frac{\Omega_{rf}t}{2})\big(1 - \frac{q_x}{2}\cos(\Omega_{rf}t)\big) \tag{2.4}$$

where $\beta_x = \sqrt{a_x + \frac{q_x^2}{2}}$ and A is a constant depending on the initial conditions. So the motion consists of harmonic motion at frequency $\nu_{sec} = \beta_x\frac{\Omega_{rf}}{2}$, called the secular motion. On top of this, there is a low amplitude ($q_x << 1$) oscillation at the applied radio frequency, referred to as micro-motion. This component in typical experiments is small enough to be ignored and so the ion's motion is equivalent to that of a harmonic oscillator with frequency ν_{sec}. So it is as if the ion is trapped in a (pseudo) potential of the form $\phi = \frac{1}{2}m\nu_{sec}^2(x^2 + y^2)$ and similarly for the z direction. In case of stray static fields, the contribution of micromotion to the ion's overall motion can become non-negligible. This can significantly increase the temperature of the ions and make QIP impossible [16]. Several techniques have been developed to detect the magnitude of the micromotion which can be used as feedback to apply a compensating electric field to cancel out the stray fields. Our solution will be described in the next chapter. To bring numbers into the above discussion, consider the case of a 4 rod trap. Applying a DC voltage U to the end caps yields the potential:

$$V_{EC}(x,y,z) = \frac{U}{2z_0^2}(2z^2 - x^2 - y^2) \tag{2.5}$$

where z_0 is the distance from the end caps to the trap center. Applying a RF voltage $V_0\cos(\Omega_{rf})$ to one pair of opposing electrodes and grounding the other, yields the potential:

$$V_{rf}(x,y,z,t) = \frac{V_0}{2}\cos(\Omega_{rf}t)\big(1 + \frac{x^2 - y^2}{r_0^2}\big) \tag{2.6}$$

where r_0 is the distance from the trap center to the rods. This equation is exact in the case of hyperbolic electrodes. In this case:

$$q_x = \frac{eV_0}{mr_0^2\Omega_{rf}^2} = -q_y \text{ and } q_z = 0 \tag{2.7}$$

$$a_x = a_y = -a_z/2 = \frac{-2eU}{mz_0^2\Omega_{rf}^2} \tag{2.8}$$

For typical trap parameters, $a_i \approx 0$ so the secular frequency is given by:

$$\nu_{sec} = \frac{\beta_x\Omega_{rf}}{2} = \frac{q_x\Omega_{rf}}{2\sqrt{2}} = \frac{eV_0}{\sqrt{2}m\Omega_{rf}r_0^2} \tag{2.9}$$

Our trap is a microfabricated surface electrode trap from Sandia National labs where the trap electrodes are arranged on a surface rather than as rods in 3D. Regardless, the above equation for the secular frequency still holds with $r_0 = 140$ μm [112]. This trap can be safely operated with $V_0 = 250$ V. Using an RF drive of 45 MHz, this yields a radial secular frequency of $\nu_{sec} = 3.6$ MHz for ^{133}Ba$^+$. Based on [112] the trap depth for the Sandia trap is given by $(0.028)\frac{1}{2}m\nu_{sec}^2r_0^2$. For our setup this yields a trap depth of 0.19 eV. This corresponds to a temperature of 2000 K. So if the ion collides with a particle of energy less than 0.19 eV it will not leave the trap. Typical 4-rod style Paul traps can attain trap depth on the order of 1 eV but the lower depth is expected of a surface trap. With these numbers the trap stability parameter $q_x = 0.12$.

2.3 Making a chain

In the previous section we considered what happens to a single particle in a radio frequency Paul trap. Now we'll discuss how multiple ions can be trapped into a linear chain along the z-direction, through the competition between the attractive trapping potential and the repulsive Coulomb force between the ions, if the radial secular frequencies $\nu_{x,y}$ are much greater than the axial frequency ν_z. The potential energy of a system of N ions is given by:

$$V(x,y,z) = \frac{m}{2}\sum_{i=1}^{N}(\nu_x^2 x_i^2 + \nu_y^2 y_i^2 + \nu_z^2 z_i^2) + \frac{e^2}{8\pi\epsilon_0}\sum_{i,j=1 i\neq j}\frac{1}{\sqrt{(x_i-x_j)^2+(y_i-y_j)^2+(z_i-z_j)^2}} \tag{2.10}$$

The equilibrium position of the ions can be found by setting $x_i = y_i = 0$, which is valid under the assumption that $\nu_{x,y} >> \nu_z$ and solving the system of equations $\frac{\partial V}{\partial z_i} = 0$ [63]. As an example the equilibrium position of 10 ^{133}Ba$^+$ ions in an axial potential $\nu_z = 150$ kHz is shown in figure 2.2. The spacing between the ions increases closer to the edge of the chain because ions closer to the edge have fewer ions pushing them towards the center through the Coulomb repulsion. The average spacing in this case is $6.0 \pm 0.7\mu m$. This deviation from uniformity can be reduced by adding buffer ions to the ends of a chain. The Lagrangian for this system is given by:

$$L = \frac{m}{2}\sum_{i=1}^{N}\sum_{k=1}^{3}\dot{q_i^k}^2 - \sum_{i,j=1}^{N}\sum_{k=1}^{3}\frac{\partial^2 V}{\partial q_i^k \partial q_j^k} q_i^k q_j^k$$

(2.11)

Here the q_i^k denote excursions from the equilibrium position of the i^{th} ion's k^{th} coordinate. For example for the x coordinate, $x_i(t) = x_{i0} + q_i^1(t)$. The potential has been expanded to second order about the equilibrium positions which for the radial direction are assumed to be $x_{i0} = y_{i0} = 0$ and in the axial direction, they must be calculated from equation 2.10. Terms of the form $\frac{\partial^2 V}{\partial q_i^k \partial q_j^l}$ for $k \neq l$ turn out to be zero under this condition. At low temperatures, after cooling, the ions are fixed at their equilibrium positions. Perturbations from laser beams can cause them to start oscillating about this point. We can decompose this motion into a sum of normal modes or collective vibrational modes of the chain: $q_i^k = \sum_{m=1}^{N} b_{m,i}^k e^{i\omega_m^k t}$ where ω_m is the frequency of normal mode m and $b_{m,i}^k$ describes the contribution of ion i to that mode. We have one such equation for each coordinate k of the ion so in total there are 3N normal modes, 2N in the radial direction (x, y) and N in the axial direction (z). Using the Euler-Lagrange equation $\frac{\partial L}{\partial q_i^k} - \frac{d}{dt}\frac{\partial L}{\partial \dot{q}_i^k} = 0$ and substituting in the normal mode decomposition we get a matrix eigenvalue equation that can be solved for the normal mode frequencies and contribution vectors: $A^k \boldsymbol{b}_m^k = -m(\omega_m^k)^2 \boldsymbol{b}_m^k$. The matrix A^k is defined as [40]:

$$A_{ij}^k = \begin{cases} m\nu_k^2 - c_k \sum_{l \neq i} \frac{e^2/(8\pi\epsilon_0)}{|z_{i0}-z_{l0}|^3} & i = j \\ c_k \frac{e^2/(8\pi\epsilon_0)}{|z_{i0}-z_{l0}|^3} & i \neq j \end{cases}$$

(2.12)

where $c_{x,y} = 1$ and $c_z = -2$. The matrix is symmetric so the normal mode participation vectors $\boldsymbol{b}_m^k$ are orthogonal. The axial and radial normal mode frequencies, along with a few of the normal mode vectors are depicted in figure 2.2 for the case of $\nu_z = 150$ kHz and $\frac{\nu_{x,y}}{\nu_z} = 10$. The axial modes have a lower frequency since $\nu_z < \nu_{x,y}$ and are uniformly spaced. On the other hand the spacing between the radial modes shrink at higher frequencies. The normal mode eigenvectors are shown in figure 2.2 (c). In the center of mass (COM) mode, all ions move in phase with each other, in the same direction. In the axial direction, the COM mode has the lowest frequency while in the radial direction the COM mode has the highest frequency. On the other hand, the zig-zag mode, where neighbouring ions move in opposite directions, has the lowest frequency in the radial but the highest frequency in the axial direction. In the above we assumed that $\frac{\nu_{x,y}}{\nu_z}$ is large enough that we can assume the equilibrium positions in the radial direction to be zero i.e. $x_{i0} = y_{i0} = 0$. It can be shown that as long as $\frac{\nu_{x,y}}{\nu_z} > 0.73\mathrm{N}^{0.86}$, then the ion crystal will take the shape of a linear chain. Below this value, the chain forms into a zig-zag shape [143]. This can be used to determine in practice how large the radial frequencies need to be compared to the axial.

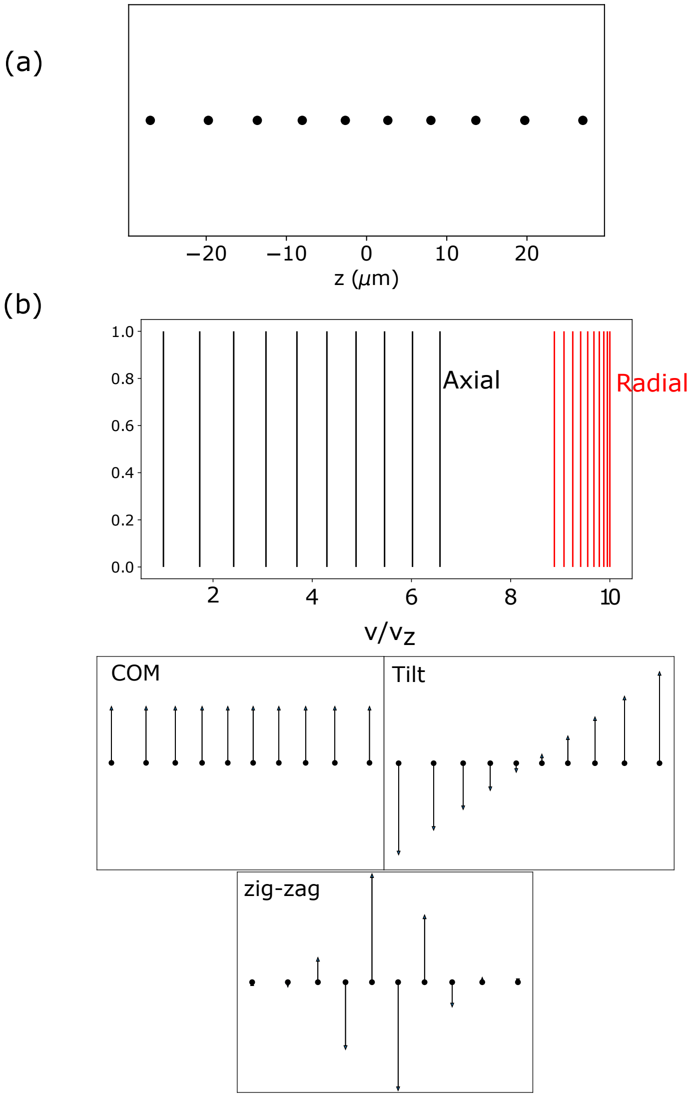

Figure 2.2: (a) Ion positions for a chain of 10 ions in an axial potential with $\nu_z = 150$ kHz. The average spacing is $6.0 \pm 0.7\mu m$. (b) Frequency of the transverse (Radial) and axial normal modes for a chain of 10 ions with ν_z same as (a) and $\nu_{x,y} = 10\nu_z$. The axial modes have approximately equidistant frequencies while the radial modes bunch up together. (c) Graphical depiction of the normal mode eigenvectors $\boldsymbol{b}_m$ for the transverse direction.

2.4 Cooling a chain

A cloud of atoms produced by ablation can have temperatures > 30000 K [140]. So only the slower fraction of the ions can be trapped and in order to enter the trap and remain trapped, these ions need to be cooled. This is done using Doppler cooling. The basic idea of this technique is that an ion will see a red-detuned laser as being on resonance in its rest frame if it is travelling towards it. If the ion is travelling away from the beam, the frequency is further red-detuned. So the momentum kicks imparted to the ion by the photons are in a direction that slow it down. Further, spontaneous emission is approximately isotropic so it will cause no net change in the ion's momentum. In this way, the red-detuned laser can be used to slow an ion down. Unlike an optical molasses or a magneto-optical trap, requiring 6 counter propagating beams, Doppler cooling of (trapped) ions requires only one beam. This is because the ion's motion is periodic. During the half cycle that the ion is moving away from the beam, the frequency is further red-shifted in it's rest frame so the ion experiences no "kick". During the half cycle that the ion is moving towards the beam, the Doppler cooling light is near resonant and provides a "kick" in the direction opposite it's motion, thus slowing down the ion. This one beam should have overlap with all three spatial directions so that the ion chain is cooled in all directions. One can show that the steady state temperature for this technique is [77]:

$$T_{ss} = \frac{\hbar\Gamma}{8K_b}(1+\zeta)\big[(1+s)\frac{\Gamma}{2\Delta} + \frac{2\Delta}{\Gamma}\big] \tag{2.13}$$

Here Γ is the line-width of the transition used for cooling, K_b is the Boltzmann constant, s is the saturation parameter, Δ is the detuning from the transition and ζ gives the average amount of momentum kick from spontaneous emission in the direction of the laser. The minimum temperature is reached when $\Delta = \Gamma\sqrt{1+s}/2$. This is given by [77]:

$$T_{min} = \frac{\hbar\Gamma\sqrt{1+s}}{4K_b}(1+\zeta) \tag{2.14}$$

The temperature is lower at lower saturation but it also takes longer to reach T_{min} for a smaller saturation parameter. For dipole radiation $\zeta = 2/5$ and assuming $s << 1$, the minimum temperature simplifies to $T_{min} = \frac{7\hbar\Gamma}{20K_b}$. In terms of the average number of quanta, $\bar{n}_{min} = \frac{7\Gamma}{20\nu_{sec}}$. For the $S_{1/2}$ to $P_{1/2}$ transition in Barium, $\Gamma \approx 2\pi \times 20$ MHz and using $\nu_{sec} = 3.6$ MHz as calculated previously, we get a steady state phonon number of $\bar{n}_{min} \approx 2$. To be useful for quantum information processing, ions need to be cooled to near their motional ground state ($\bar{n}_{min} \approx 0$). This is not possible with Doppler cooling unless the secular frequencies are significantly increased. The reported 3.6 MHz is around the highest that can be done with our trap. Further increasing ν_{sec} by increasing the RF voltage will lead to RF breakdown which can permanently damage the trap by resulting in the formation of shorted connections [112, 141].

To get close to the ground state, a combination of electromagnetically induced transparency (EIT) cooling and resolved sideband cooling is used [77, 75]. Resolved sideband cooling requires the use of a narrow linewidth transition so that the motional mode frequencies can be resolved. The 20 MHz transition used for Doppler cooling will not work since the motional modes have frequencies on the order of a few MHz as shown above. As a result, quadrupole transitions or Raman transitions, involving the hyperfine states, with linewidths $\Gamma << \nu$ are used. Cooling is done by setting the detuning of this transition onto resonance with the red sideband. The minimum temperature attainable with this technique is approximately $\bar{n}_{min} \approx (\frac{\Gamma}{2\nu})^2$. This is approximately zero since we are using a transition for which $\Gamma << \nu$ [77]. With many ions and many modes this can be time consuming as each mode must be cooled separately. The solution to this problem is EIT cooling. The fano resonance of EIT is broad enough to enhance red sideband transitions for many motional modes, but narrow enough so that blue sideband transitions are suppressed. With EIT cooling, the ion can get close to the ground state but not as well as resolved sideband cooling. This is because the blue sideband has a small but non-negligible scattering rate with EIT while the very narrow transition used for resolved sideband cooling yields a very small scattering rate on the blue sideband, at the cost of having to cool each mode separately. Often the two methods are used in conjunction where EIT is used to get all the modes relatively close to the ground state and then resolved sideband cooling is used to further cool the modes of interest that will participate in quantum information processing.

2.5 Single qubit gates

Single qubit gates constitute rotations about a vector in the equatorial plane of the Bloch sphere. These are implemented using a microwave horn that directly drives the hyperfine qubit or using a pair of laser beams whose beat note is resonant with the hyperfine splitting. The former can only implement simultaneous global rotations while the latter can be used for individual addressing. The implemented unitary has the form:

$$R(\phi, \theta) = \begin{bmatrix} \cos(\theta/2) & -\sin(\theta)e^{-i\phi} \\ -\sin(\theta)e^{\phi} & \cos(\theta/2) \end{bmatrix} \tag{2.15}$$

where ϕ is the angle the rotation axis makes with the x-axis of the Bloch sphere and θ is the rotation angle of the Bloch vector about the axis defined by ϕ. ϕ is determined by the phase of the laser or microwave pulse and θ is set by the Rabi frequency and pulse duration.

2.6 Two-qubit gates

The main way the internal states of a pair of ions in a chain are entangled is through the shared motional modes of the chain. There are several ways to do this but the most popular is the Mølmer–Sørensen scheme [127]. This method uses a pair of laser beams that are detuned from the qubit frequency. One is blue detuned by an amount μ ($\omega_b = \omega_q + \mu$) and the other is red detuned by the same amount $\omega_r = \omega_q - \mu$. The Hamiltonian of a chain of N ions interacting with this bichromatic laser field is given by:

$$H_{MS} = \sum_{\text{ion } i,\text{ mode } m} \frac{\eta_{i,m} \cdot \Omega_i(t)}{2} \sigma_x^i \, \sin(\mu t) \big(a_m e^{-i\omega_m t} + a_m^\dagger e^{i\omega_m t} \big) \tag{2.16}$$

here $\eta_{i,m} = \Delta k b_{i,m} \sqrt{\frac{\hbar}{2m\omega_m}}$ is the generalized lamb-dicke parameter for ion i and mode m. To arrive at this Hamiltonian we have made the assumption that the ion chain has been cooled to the lamb-dicke limit, that is, $\eta_{i,m}\sqrt{n} << 1$. Δk is the difference between the wavevectors of the two raman beams whose beat-notes at $\omega_q \pm \mu$ generates this interaction. For maximum spin-motion coupling the two beams should be counter-propagating and to minimize coupling, if say one is only interested in implementing single qubit gates with raman, then the beams should be co-propagating. ω_m is the frequency of normal mode m and $\Omega_i(t)$ is rabi frequency of ion i. In our setup the two raman beams are orthogonal to the chain so they can only excite the radial modes. The tighter confinement of the radial modes means that they can be cooled to a lower temperature and makes them less sensitive to ion heating. But this is a double edge sword as the tighter confinement also means a smaller lamb-dicke parameter, thus to achieve the same interaction strength as with a system using the axial modes, the laser power needs to be increased. Since $\eta_{i,m} \propto 1/\sqrt{\omega_m}$, the required increase in power is not substantial. One of the raman beams illuminates all the ions equally while the other is focused down on individual ions. This individual addressing beam allows for independent control over the magnitude of Ω_i. While using the radial modes is a more natural choice if we are to do individual addressing, it may not be suitable in some cases. For example, when chains consist of two different species, the radial normal modes tend to separate into those that significantly couple one species or the other. This effect is less severe for the axial modes. So the axial modes are a better choice for performing inter-species or inter-isotope entangling gates[128].

To find the time-evolution operator for the above Hamiltonian, we can use the Magnus expansion, $U(t) = e^{\gamma_1+\gamma_2+\cdots}$ where the terms γ_1 and γ_2 are given by:

$$\gamma_1(t) = -i\int_0^t H_{MS}(t^{'})\mathrm{dt} \tag{2.17}$$

$$\gamma_2(t) = \frac{-1}{2}\int_0^t \mathrm{dt}^{'}\int_0^{t^{'}} [H_{MS}(t^{'}), H_{MS}(t^{''})]\mathrm{dt}^{''} \tag{2.18}$$

The higher order terms turn out to be zero as $[H_{MS}(t^{'}), [H_{MS}(t^{''}), H_{MS}(t^{'''})]] = 0$. Computing the above integrals yields the following for the time evolution operator:

$$U(t) = \exp\left[\sum_{i=1,m=1}^{N}(\alpha_{i,m}(t)\hat{a}_m^{\dagger} + \alpha_{i,m}(t)\hat{a}_m)\cdot\sigma_x^i + i\cdot\sum_{i=1,j=1}^{N}\chi_{i,j}(t)\sigma_x^i\sigma_x^j\right] \tag{2.19}$$

where:

$$\alpha_{i,m}(t) \equiv -\eta_{i,m}\int_0^t \Omega_i(t^{'})\mathrm{sin}(\mu t^{'})e^{i\omega_m t^{'}}\mathrm{dt}^{'} \tag{2.20}$$

$$\chi_{i,j}(t) \equiv -2\sum_m \eta_{i,m}\eta_{j,m}\left(\int_0^t\left(\int_0^{t^{'}}\Omega_i(t^{'})\Omega_j(t^{''})\mathrm{sin}(\mu t^{'})\ \sin(\mu t^{''})\ \sin(\omega_m(t^{''}-t^{'}))\ \mathrm{dt}^{''}\right)\mathrm{dt}^{'}\right) \tag{2.21}$$

The second term in equation 2.19, involving the tensor product of σ_x on ions i and j is what creates a two-qubit entangling interaction. The first term, resembling the displacement operator, on the other hand causes spin-motion entanglement between mode m and ion i. If the ions start in the ground state of the motion, the displacement operator generates the coherent state $|\alpha_{i,m}(t)\rangle$, where $\alpha_{i,m}(t)$ represents some trajectory in phase space generated by the motional part of the unitary. To use this interaction for spin-spin entanglement we must somehow remove the spin-motion coupling term. For the case of digital quantum gates, this is done by tuning the parameters of the problem (laser powers, frequency, phases) so that the spin-motion term vanishes at the end of the interaction. That is, if the interaction is turned on for a time τ, then $U(\tau) = \exp\left[i\cdot\sum_{i=1,j=1}^{N}\chi_{i,j}(t)\sigma_x^i\sigma_x^j\right]$. In terms of the phase space picture, the trajectories for each mode must end back at the origin of phase space. As we will see, by having a sufficiently large detuning μ, we can create a situation where the spin-motion term is negligible throughout the interaction. This latter technique is used for analog quantum simulation.

Focusing on digital gates for now, to disentangle spin and motion, it is needed that $\alpha_{i,m}(\tau) = 0$ for all ions i and modes m, at the end of the gate duration τ. Further, if we shine light only on ions i and j, the unitary 2.19 further simplifies to:

$$U(\tau) = e^{i\chi_{ij}\sigma_x^a\sigma_x^b} = \begin{bmatrix} \cos(\chi_{ij}) & 0 & 0 & -i\sin(\chi_{ij}) \\ 0 & \cos(\chi_{ij}) & -i\sin(\chi_{ij}) & 0 \\ 0 & -i\sin(\chi_{ij}) & \cos(\chi_{ij}) & 0 \\ -i\sin(\chi_{ij}) & 0 & 0 & \cos(\chi_{ij}) \end{bmatrix} \tag{2.22}$$

The sign of χ_{ij} depends on the sign of the normal mode participation vector components for ions i and j. These are hidden inside the lamb-dicke parameters in equation 2.21. Figure 2.3 shows how these native trapped-ion entangling gates can be used to implement the CNOT gate or the controlled-phase gate, necessary for the implementation of the quantum Fourier transform, an integral component of Shor's factoring algorithm [101].

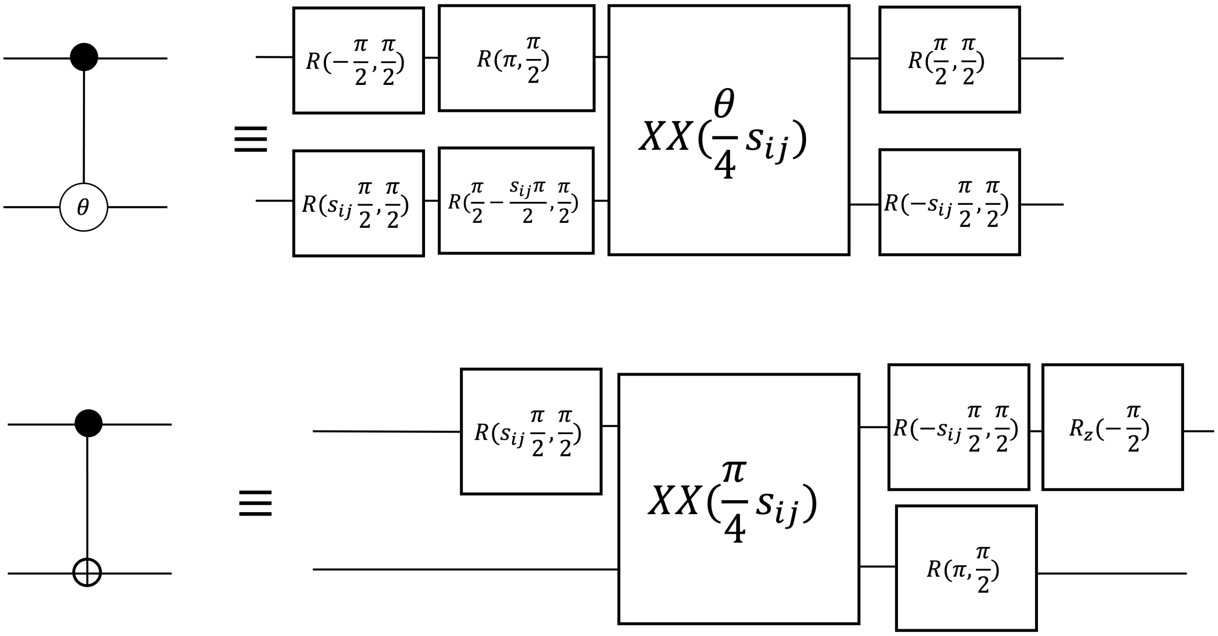

Figure 2.3: Implementing the Controlled phase (top) and the CNOT gate (bottom) using an ion trap computer's native gate set. $s_{ij} = \pm 1$ denotes the sign of χ_{ij} which depends on what two ions in the chain are participating in the gate [37].

To see how the $\alpha_{i,m}(\tau) = 0$ constraint can be satisfied, consider a constant rabi-frequency $\Omega_i(t) = \Omega_0$. In this case, equation 2.21 for the $\alpha_{i,m}(\tau)$ evaluates to:

$$\alpha_{i,m} = \frac{\eta_{i,m}\Omega_0}{\mu^2 - \omega_m^2}\left[e^{i\omega_m t}(\mu\,\cos(\mu t) - i\omega_m\,\sin(\mu t)) - \mu\right] \tag{2.23}$$

When the detuning $\delta_m \equiv \mu - \omega_m << \mu + \omega_m$ the phase space trajectories become approximately circular:

$$\alpha_{i,m} = \frac{\eta_{i,m}\Omega_0}{2\delta_m}\left(e^{i\delta_m t} - 1\right) \tag{2.24}$$

Therefore, by picking the gate duration $\tau = \frac{2\pi}{\delta_m}$, we can get the phase space trajectory for mode m to close at the end of the gate. If we have a two ion chain, then by placing the detuning μ halfway between both modes ($\delta_1 = -\delta_2$) we can get both trajectories to close with this choice of gate duration. This is shown in figure 2.4. However, for an N ion chain, it is unlikely that control over only two constant parameters, namely the gate duration and detuning, will allow all N phase space trajectories to close simultaneously at the end of the gate.

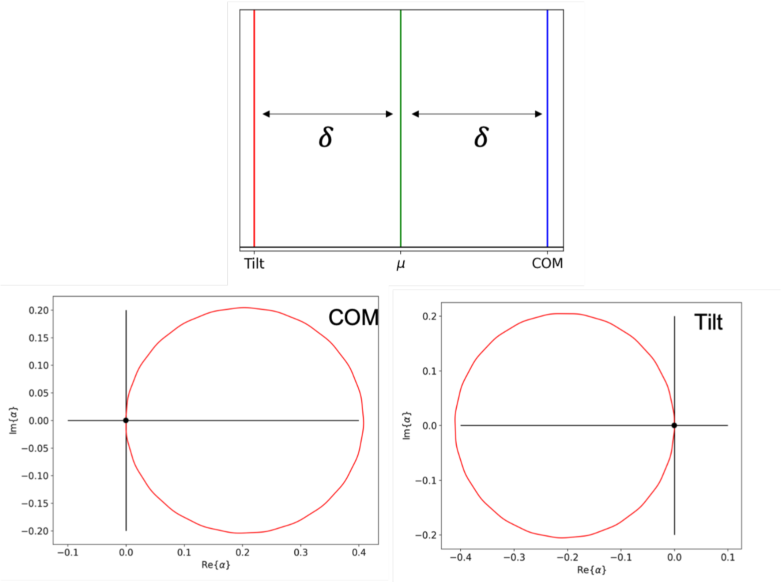

Figure 2.4: Top: The detuning μ is placed half way between the center of mass and tilt radial frequencies of the chain. Bottom: Phase space trajectories for the two modes, resulting from the interaction in equation 2.19. By picking the gate duration $\tau = \frac{2\pi}{\delta} \cdot n$ where $n \in \mathbb{Z}^+$, both motional modes return to the origin in phase space.

The constraints $\alpha_{i,m} = 0$ represent a set of 2N equations (N for the real and N for the imaginary part of $\alpha_{i,m}$). Typically the geometric phase is set to $\chi_{ij} = \pi/4$ so that the XX gate generates the maximally entangled state $|00\rangle \mp i\,|11\rangle$ from an initial $|00\rangle$ state. Taken together, this is a set of 2N+1 constraints that we need to satisfy at the end of the interaction. To satisfy all these requirements, the amplitude, phase or frequencies of the laser beams can be made functions of time [50, 80, 89, 25]. Figure 2.5 shows how a piecewise constant modulation of the amplitude can be used to simultaneously close the phase space trajectory of all modes in a 5 ion chain. In this case, an 11 segment pulse is used but it turns out that one can get away with fewer segments as well. The pulse shapes were obtained through numerical optimization. Such a pulse shape needs to be calculated for every pair of ions in the chain since every ion pair i,j couples to the modes m differently [37]. These optimization techniques can also be used to make the interaction less sensitive to fluctuations in the laser parameters, such as the detuning. If all motional modes return back to their initial state after time τ, the two-qubit unitary in equation 2.22 can be realized. For the pulse in figure 2.5, the geometric phase was fixed to $\chi_{ij} = \pm\pi/4$. Other values can be realized by simply scaling this optimal solution.

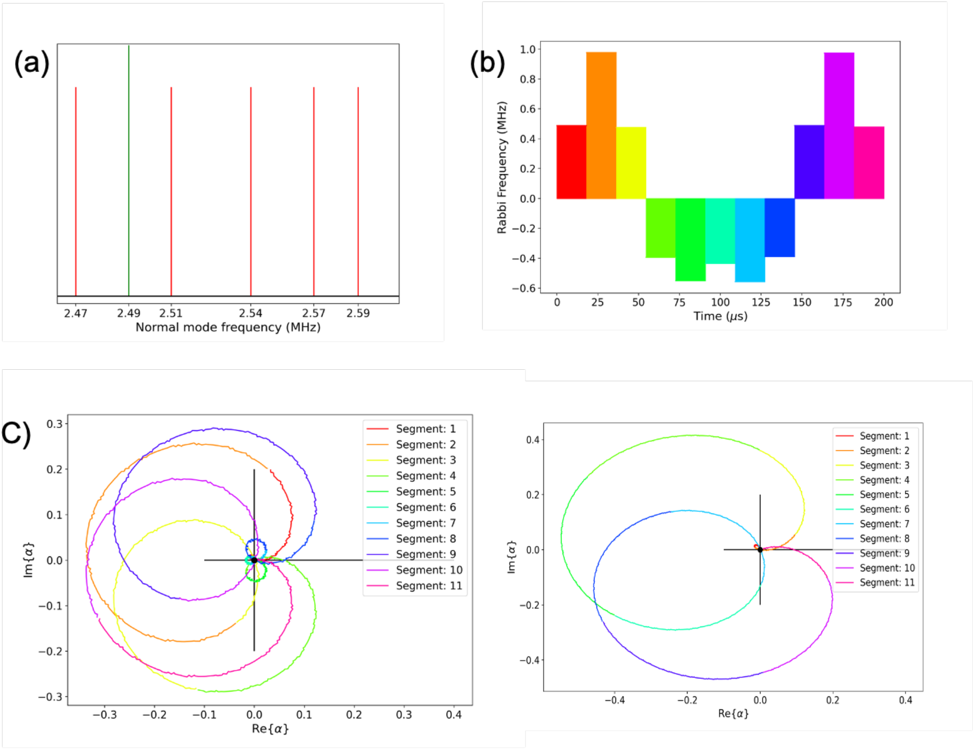

$\omega_m = 2.54\ MHz$ $\omega_m = 2.51\ MHz$

Figure 2.5: (a) Position of the laser detuning (green) relative to all the axial modes of the chain participating in the interaction (red). (b) The 200 μs 11 segment pulse used to close the phase space trajectories at the end of the interaction. (c) The resulting phase space trajectories for two of the five modes. The colors of each curve segment is the same as the color of the corresponding pulse segment in (b). The black dot denotes the final position of $\alpha_{i,m}(t)$, which as desired is at the origin of phase space. The normal mode frequency and eigenvectors for these simulations were calculated using code written by Yi Hong Teoh.

2.7 Analog Quantum Simulation

The same interaction as discussed in the digital quantum gate section can be used to realize arbitrary spin-models, in any dimension, afforded by the all to all connectivity of the ion chain. If we evaluate the integrals in equation 2.21 for constant rabi frequencies, we get:

$$\alpha_{i,m}(t) \equiv -\eta_{i,m}\int_0^t \Omega_i(t^{'})\text{sin}(\mu t^{'})e^{i\omega_m t^{'}}\,\text{dt}^{'} \tag{2.25}$$

$$= \frac{\eta_{i,m}\Omega_i}{\mu^2-\omega_m^2}\left[e^{i\omega_m t}(\mu\ \cos(\mu t) - i\omega_m\ \sin(\mu t)) - \mu\right] \tag{2.26}$$

$$\chi_{i,j}(t) \equiv -2\sum_m \eta_{i,m}\eta_{j,m}\left(\int_0^t\left(\int_0^{t^{'}} \Omega_i(t^{'})\Omega_j(t^{''})\text{sin}(\mu t^{'})\ \sin(\mu t^{''})\ \sin(\omega_m(t^{''}-t^{'}))\ \text{dt}^{''}\right)\text{dt}^{'}\right) \tag{2.27}$$

$$= \sum_m \frac{\eta_{im}\eta_{jm}\Omega_i\Omega_j}{2(\mu^2-\omega_m^2)}\Big[-\omega_m t + \frac{\omega_m sin(2\mu t)}{2\mu} + \mu\frac{sin((\mu-\omega_m)t)}{\mu-\omega_m} - \mu\frac{sin((\mu+\omega_m)t)}{-\mu+\omega_m}\Big] \tag{2.28}$$

In the limit $\mu >> \omega_m$ for all modes m, $\alpha_{i,m}(t) \rightarrow 0$ for all time since the equation is bounded in time. At the same time, the equation for the geometric phase simplifies to:

$$\chi_{ij}(t) = -\sum_m \frac{\eta_{im}\eta_{jm}\Omega_i\Omega_j\omega_m}{2(\mu^2-\omega_m^2)}t \tag{2.29}$$

If we now define:

$$J_{ij} = \sum_m \frac{\eta_{im}\eta_{jm}\Omega_i\Omega_j\omega_m}{2(\mu^2-\omega_m^2)} = \sum_m \frac{b_{im}b_{jm}\Omega_i\Omega_j\Omega_m}{2(\mu^2-\omega_m^2)} \tag{2.30}$$

where $\Omega_R = \frac{\hbar\Delta k^2}{2m}$. With this, the time-evolution operator 2.19, simplifies to:

$$U(t) = e^{-i\left(\sum_{i,j} J_{ij}\sigma_x^i\sigma_x^j\right)t} \tag{2.31}$$

which corresponds to the Ising-like Hamiltonian: $H = \sum_{i,j} J_{ij}\sigma_x^i\sigma_x^j$. With this particular form of the J_{ij} coupling matrix, we cannot realize arbitrary spin models. However some interesting cases can be realized. For example, a fully anti-ferromagnetic ($J_{ij} > 0$ for all i, j) interaction can be realized by setting the detuning, μ, to be greater than the radial center of mass frequency, ω_{COM}. Alternatively a fully ferromagnetic ($J_{ij} < 0$ for all i, j)

interaction can be generated by setting $\mu \lesssim \omega_{\mathrm{COM}}$ [62]. The interaction graphs for these cases and a few others are shown in figure 2.6. Control over the frequency and amplitude of each beam shining on the ion chain on the other hand, can give arbitrary control over the couplings so that arbitrary spin models can be simulated [133, 110, 68]. This modified J_{ij} matrix is given by [134]:

$$J_{ij} = \sum_{n}^{N} \Omega_{i,n}\Omega_{j,n} \sum_{m}^{N} \frac{b_{im} b_{jm} \Omega_m}{2(\mu_n^2 - \omega_m^2)} \tag{2.32}$$

where the additional sum and index on the rabi frequency is required to account for the addition of N frequency tones to each of the N beams shining on the ions. So the task is now to solve for the rabi frequencies Ω_{ij} given an arbitrary J_{ij} matrix. This inverse problem is hard to solve in general but machine learning can be used to learn and approximate the inverse to equation 2.32. With this technique, arbitrary J_{ij}'s such as that for interacting spins on a 2D Kagome or triangular lattice have been realized [134].

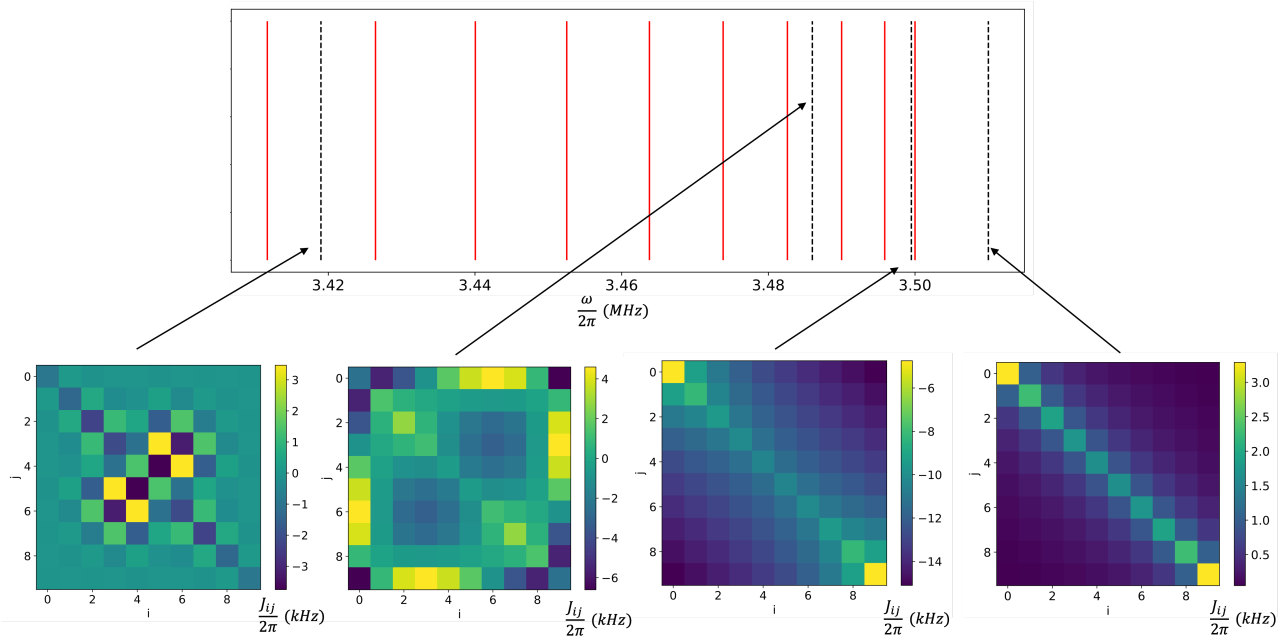

Figure 2.6: Dependence of the J_{ij} matrix given in equation 2.30 for several detunings μ. The red vertical bars denote the radial frequencies and the black dashed lines denote the detunings. The rabi frequencies, Ω_i, are taken to be 500 kHz. The trapping frequencies are chosen to be 170 kHz in the axial direction and 3.5 MHz in the radial direction, for a chain of 10 ions.

2.8 Conclusion

This chapter covered the fundamentals of quantum computing with trapped ions. We covered how a chain of ions can be trapped with a combination of RF and DC voltages and how the normal modes of this chain can be used to mediate entanglement between arbitrary sets of ions in the chain. Finally we discussed how this can be used for digital quantum computation as well as analog quantum simulation.

Chapter 3

The CW and imaging subsystems

3.1 Overview of the CW light sources and their role

For our ion trap we are interested in 3 isotopes of Barium: 133, 137, and 138. $^{133}\mathrm{Ba}^{+}$ has a spin 1/2 nucleus and thus possesses the simplest hyper-fine structure. Thus $^{133}\mathrm{Ba}^{+}$ is our primary choice for a qubit. $^{137}\mathrm{Ba}^{+}$ has a spin 3/2 nucleus, resulting in a more complex hyper-fine structure that we intend to use for qudit operations. Finally $^{138}\mathrm{Ba}^{+}$ has no nuclear spin and is the most abundant isotope of barium. As a result, this isotope is the easiest to trap and so will be used for initial diagnostics of the trapped-ion system. The energy level structure of all 3 isotopes are shown in figure 3.1.

In $^{133}\mathrm{Ba}^{+}$, the qubit is defined by the two clock states of the ground state manifold: $|0\rangle \equiv \left|\mathrm{S}_{1/2}; F=0, m_F=0\right\rangle$ and $|1\rangle \equiv \left|\mathrm{S}_{1/2}; F=1, m_F=0\right\rangle$. The 493 nm $\mathrm{S}_{1/2}$ to $\mathrm{P}_{1/2}$ transition is used for state preparation/initialization of the $|0\rangle$ state, qubit measurement and Doppler cooling. Around 24% of the population from the $\mathrm{P}_{1/2}$ level decays to the long lived $\mathrm{D}_{3/2}$ metastable state. To establish a closed cycling transition, a 650 nm laser is used to re-pump the ion out of $\mathrm{D}_{3/2}$ state. The 1762 nm laser can be used to shelve one of the hyperfine states to the long-lived $\mathrm{D}_{5/2}$ manifold which can be used for storage and measurement [27]. The 614 nm laser is used to de-shelve out of this long lived state. Shelving can also be done using a combination of the 650, 585 and 455 nm transitions but we will primarily use the quadrupole transition. All these transitions are addressed using continuous-wave (CW) diode lasers. Most of the CW lasers used in our system are external cavity diode lasers of the Littrow or Cat-eye type from MOGLabs. The lasers are locked using a HighFinesse WS8-2 wavelength meter to begin with and then we will move to more sophisticated locking schemes such as using a transfer cavity with a stable laser or Pound–Drever–Hall.

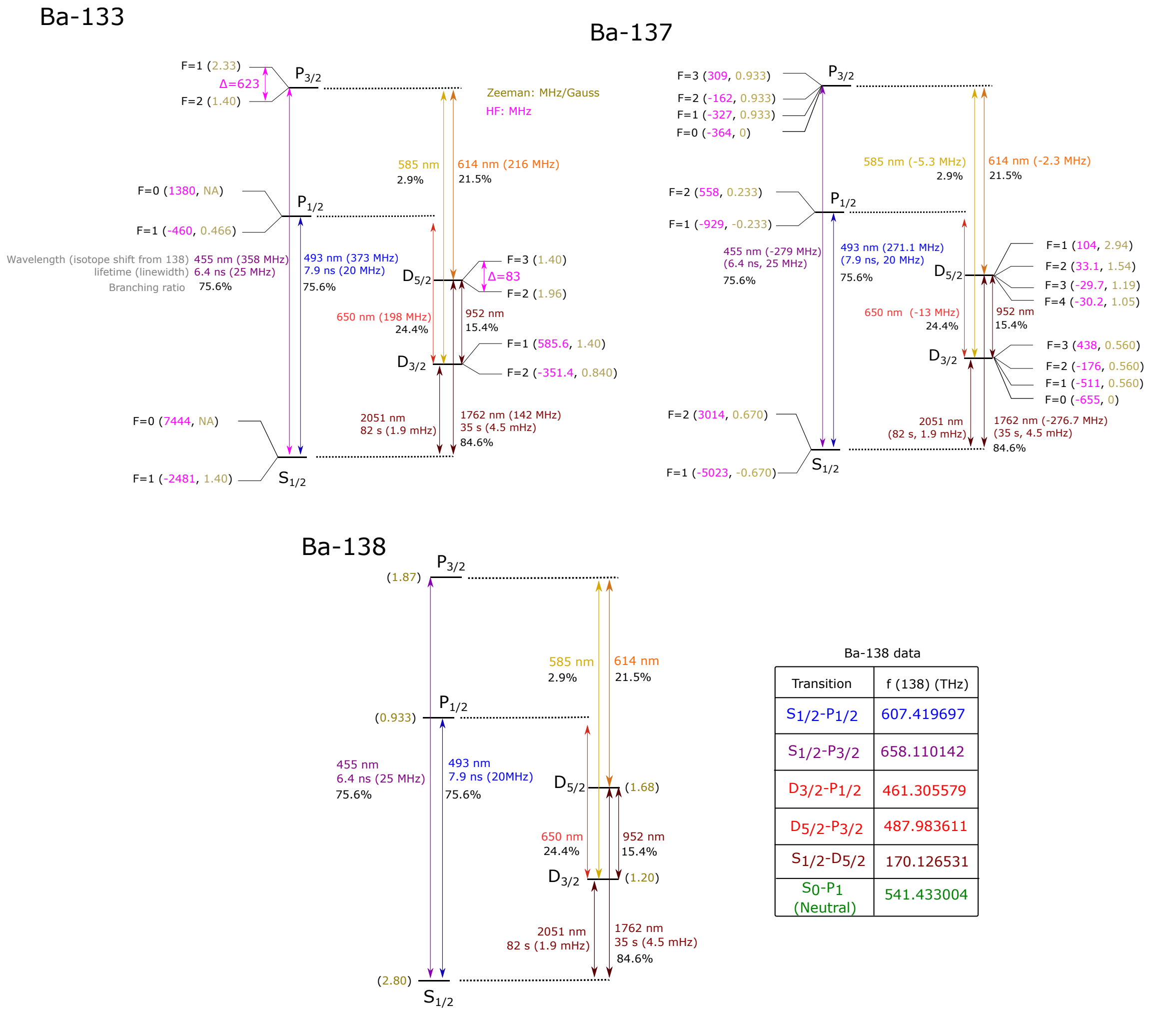

Ba-138 data

Transition	f (138) (THz)
$S_{1/2}$-$P_{1/2}$	607.419697
$S_{1/2}$-$P_{3/2}$	658.110142
$D_{3/2}$-$P_{1/2}$	461.305579
$D_{5/2}$-$P_{3/2}$	487.983611
$S_{1/2}$-$D_{5/2}$	170.126531
S_0-P_1 (Neutral)	541.433004

Figure 3.1: Energy level structure of the 3 isotopes of barium that are used in our system.

3.2 The trap

The ion-trap we use is the Phoenix 2.0 surface electrode trap from Sandia National Labs [112]. Figure 3.2 shows an optical microscope image as well as a schematic of the trap. The red regions in (a) represent the inner DC electrodes and the blue highlights the RF electrode. Beneath these electrodes, not visible from 3.2, is the ground plane. The center of the large slot on the left forms the quantum zone, with a length of 1.54 mm. This zone has the highest number of independently controllable electrodes (66 total with 22 pairs of inner electrodes and 11 pair of outer electrodes). The large slot provides a numerical aperture (NA) of 0.25 and is intended to allow for optical addressing of the ions using a beam from behind the trap. This would be from the top of our vacuum chamber since the trap is installed upside down to reduce the accumulation of contaminants. This is not possible in our system since the beam will be obstructed by the internal pumps (See chapter 4). The slot can also be used to load ions from the back of the trap but we only load ions from the front of the trap.

The second region of importance in the trap is the loading zone, located at the center of the smaller slot, around 3 mm from the center of the trap. The slot is not large enough to thread beams through and is only designed for loading from the back of the trap. However, again, our ablation targets are positioned for head-on loading into the trap. This choice was made because we can only have a small amount of ^{133}Ba in our chamber and front loading would allow for a higher atomic flux. The loading zone serves as a reservoir of ions. Once an ion from this zone is needed at the quantum zone, the large number of electrodes afforded by the surface trap permit the axial potential to be dynamically modified in way that allows the ion to be detached from the chain in the loading zone, and shuttled to the quantum zone. Having a dedicated loading zone means that we are not contaminating the quantum zone electrodes. This is useful because contamination has been shown to lead to higher heating rates of the ions. The ions are approximately trapped 68 μm above the top electrode surface in the quantum zone and the rest of the large slotted region and approximately 72 μm in the loading zone. The large number of electrodes can also be used to introduce anharmonicity to the axial confining potential. The addition of a quartic or higher order terms in the potential can be used to reduce the variation in the ion-ion spacing seen in chapter 2 [83]. Another way of improving homogeneity is to use buffer ions. In our system, we intend to ultimately trap 20 ions, 16 will act as the qubits/qudits while the 4 at the end are buffer ions that do not participate in computation but help improve the homogeneity in the pitch of the 16 inner ions. A combination of both techniques will be used to obtain a uniformly spaced chain.

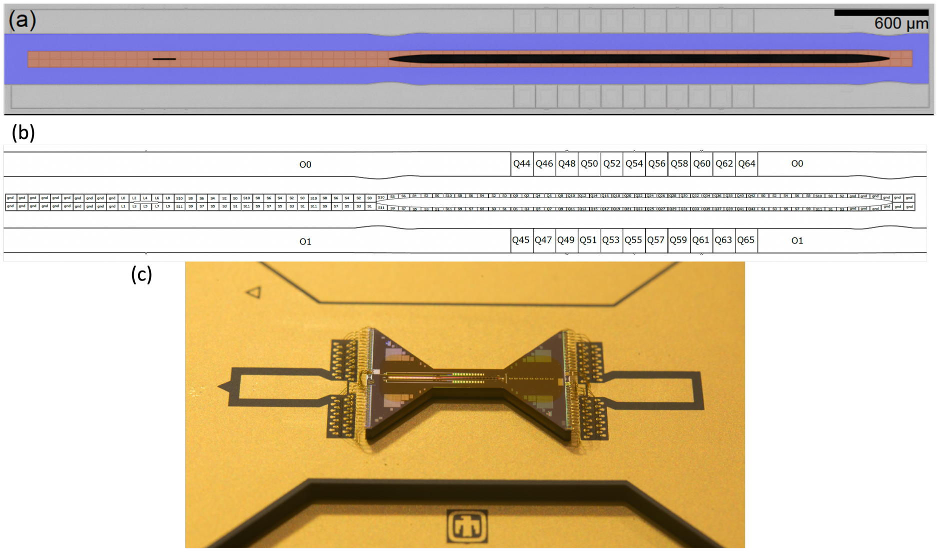

Figure 3.2: (a) Optical image [141] and (b) Schematic [112] of the Pheonix trap. The blue region highlights the RF electrode and the red regions highlight the inner DC control electrodes. The inner electrodes have a pitch of 70 μm and the width of the slot in the quantum zone is 60 μm, providing a 0.25 NA opening for an optical beam. (c) Zoomed out image of the trap.

3.3 Optomechanical Design

3.3.1 The laser rack

All CW lasers, electro-optic modulators (EOM), acousto-optic modulators (AOMs), second harmonic generation (SHG) crystals, scanning Fabry-Perot cavities and the wavemeter are placed inside a rack cabinet we call the “laser rack”. The rack is placed adjacent to the optics table where the vacuum chamber and all the optics that direct light onto the ions are located. Light from the lasers is delivered to the table through several fiber optic cables. This whole system is enclosed inside a custom environmental chamber that provides temperature and humidity stability. These are important for stabilizing the frequencies of our lasers and minimizing drifts in beam pointing or fiber coupling. The components of the control system (Microwave synthesizers, DDS modules, ADC/DAC channels, TTL input/output, etc.) are placed inside a second rack cabinet. This is placed outside the environmental chamber and a patch-panel feed-through is used to transfer signals from the control system to the experiment and back. This overview of our system is shown in figure 3.3.

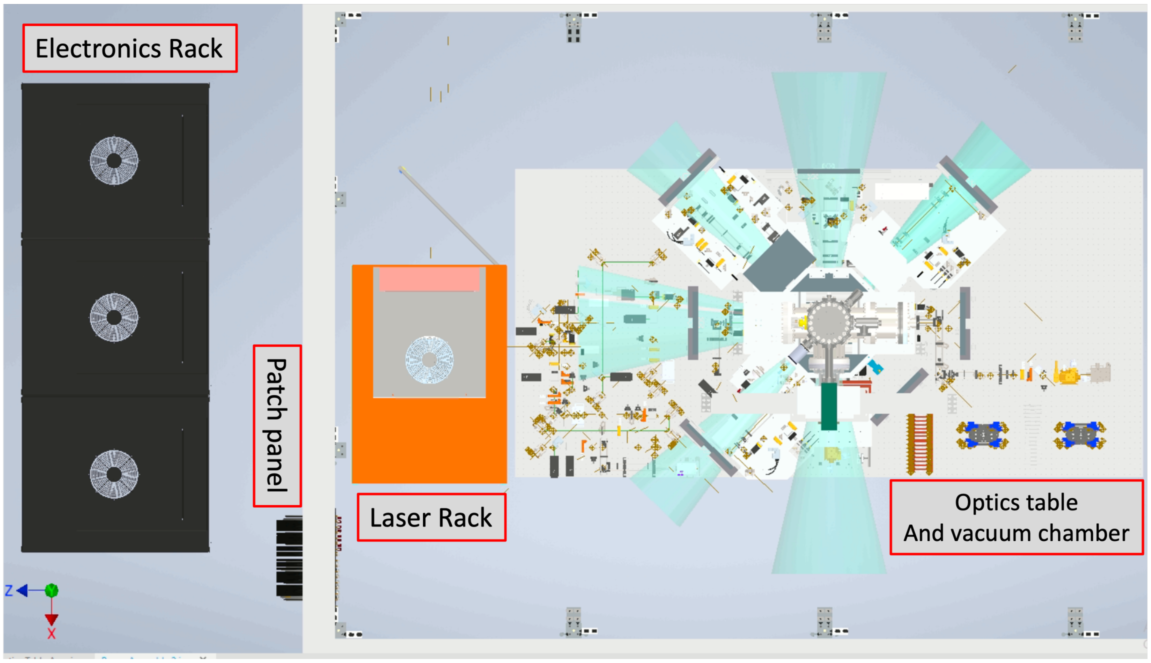

Figure 3.3: Overview of the experiment. The experiment is housed inside an environmental chamber that provides temperature and humidity stability. All the continuous wave lasers, modulators, doublers, and other optics are housed inside the laser rack. This light is delivered to the optics table, where the vacuum chamber resides, using several fiber cables. The electronics rack outside the environmental chamber holds components of the control system. Signals are exchanged between the experimental equipment (lasers, vacuum gauges, EOMs, AOMs, etc.) and the control system through patch panels in the wall of the environmental chamber.

The lasers are fiber coupled using the optical setup shown in figure 3.4. For all the optical systems in this project we decided to move away from posts, post-holders, forks, clamps, etc. and instead machine custom aluminum breadboard to directly mount any optical component to. This way of building optics significantly reduces the number of degrees of freedom in the system, thus reducing drifts and misalignment. It also allows optical setups to be shrunk by taking advantage of both vertically and horizontally mounted optics. The main disadvantage of this way of design is that once the breadboards are machined, mistakes in the design can be time consuming to fix as it may require remachining. But as an anecdotal testament to the robustness of this design, our laser pegboards maintained fiber coupling even after our entire setup was moved between two buildings. Though the power was significantly reduced. In the setup, light out of the laser is first sent through a Faraday-Isolator to prevent reflected light from making it's way back into the laser. Next, elliptical beam-shaping optics correct for the elliptical profile of the light emitted by the laser diode. This is essential to maximize fiber coupling efficiency. A half-wave plate and polarizing beam splitter (PBS) are used to control the intensity of the laser beam. This is followed by a second half-wave plate that is used to set the linear polarization of the laser along the slow axis of the single mode fiber. Finally, a pair of piezo controlled mirrors are used to send light into the fiber collimator to be focused into the fiber. The piezo controlled mirror mounts will be used to compensate for slow drifts in the alignment. At two points along this path, we use beam-samplers to send light to a photodiode or camera to monitor the power and mode quality of the laser. The particular pegboard shown in figure 3.4 is for our 1107 nm laser. 3 others just like this one are used to fiber couple 493, 650 and 1228 nm. These are all placed in a single drawer of a 19 inch rack.

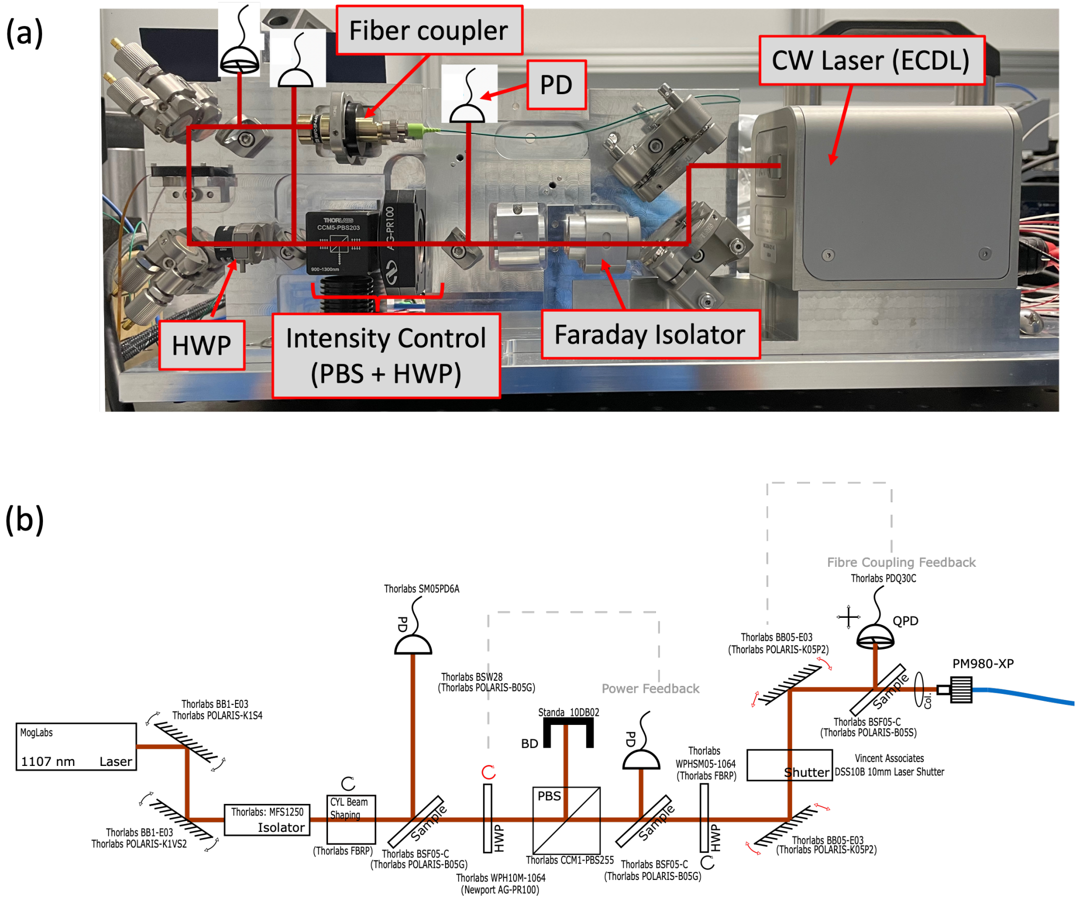

Figure 3.4: (a) Setup used to fiber couple light from each of our CW lasers. The picture shown is for the 1107 nm laser (doubled to 553 nm). There are 3 other similar boards for 493, 650 and 1228 nm. The black and white graphics superimposed on the image are placeholders for missing equipment. (b) Optical schematic for the setup shown in (a). This was adapted from the schematic made by master's student Nikolay Videnov.

From here, light from all 4 lasers is sent to a drawer containing the modulators, doublers and fiber splitters that are used to modify and combine the light before it is sent to the table and focused onto the ions. A schematic of this part of our system is shown in figure 3.5. First, 1% of the light from each laser is split off and sent to the wavemeter, also housed in the optics rack, for stabilizing the laser frequency. The 614 nm light needed for de-shelving out of $D_{5/2}$ and the 553 nm light for photoionization are generated by doubling 1228 and 1107 nm respectively. The fiber coupled SHG modules are periodically poled lithium niobate (PPLN) waveguides, packaged with a thermoelectric cooler and thermistor, from NTT Electronics. To be able address multiple hyperfine levels on the 493, 614 and 650 nm transitions, EOMs are used to create the required frequency sidebands. 1% of the light after the EOMs is picked off and sent to a set of confocal, scanning Fabry-Perot cavities (free-spectral range = 10 GHz, finess≈180) to monitor the amplitude of the sidebands imparted by the EOMs. The 493 nm EOM is a potassium titanyl phosphate (KTP) fiber coupled phase modulator from ADVR with an insertion loss of 4.1 dB. The 614 and 650 nm EOMs are fiber coupled lithium niobate phase modulators from Jenoptik with an insertion loss of around 6 dB. After the EOMs, the 493 nm and 650 nm light are split into three because they are required in three different beam paths on the table. Each of the resulting beams is then sent to one AOM (8 total). The fiber coupled AOMs, with a maximum rise time of 25 ns, act as high bandwidth laser amplitude modulators or switches. One of the 493 nm beams is then combined with one of 650 nm beams and the 553 beam. This combination is sent to the loading zone and is used to ionize (553 nm in combination with 405 nm) and then cool the resulting trapped-ions (493 and 650 nm). We call this the loading zone beam since it constitutes most of the frequencies sent to that region of the trap. For another beam path, another of the 493 and 650 nm beams is combined with the 614 nm beam. We call this the Cooling-Repump-Measurement (CRM) beam since it will be used to perform these operations in the quantum zone of the trap. The single remaining 650 nm beam is sent to the imaging beam path on the table and will be used for micromotion compensation. The single remaining 493 nm beam is sent to the table and then focused onto the quantum zone. As we will see, it will be used for optical pumping state-preparation of $^{137}\mathrm{Ba}^{+}$. These fiber optic combiners, purchased from Oz Optics, use multiple dichroics to combine the 3 beams into one path [114]. There are two lasers in our system that are not sent through the beam-prep drawer. The first is the 405 nm second photoionization beam which requires no modulation and the second is a stabilized Helium-Neon laser which is periodically used to calibrate our wavemeter and is not sent to the optics table.

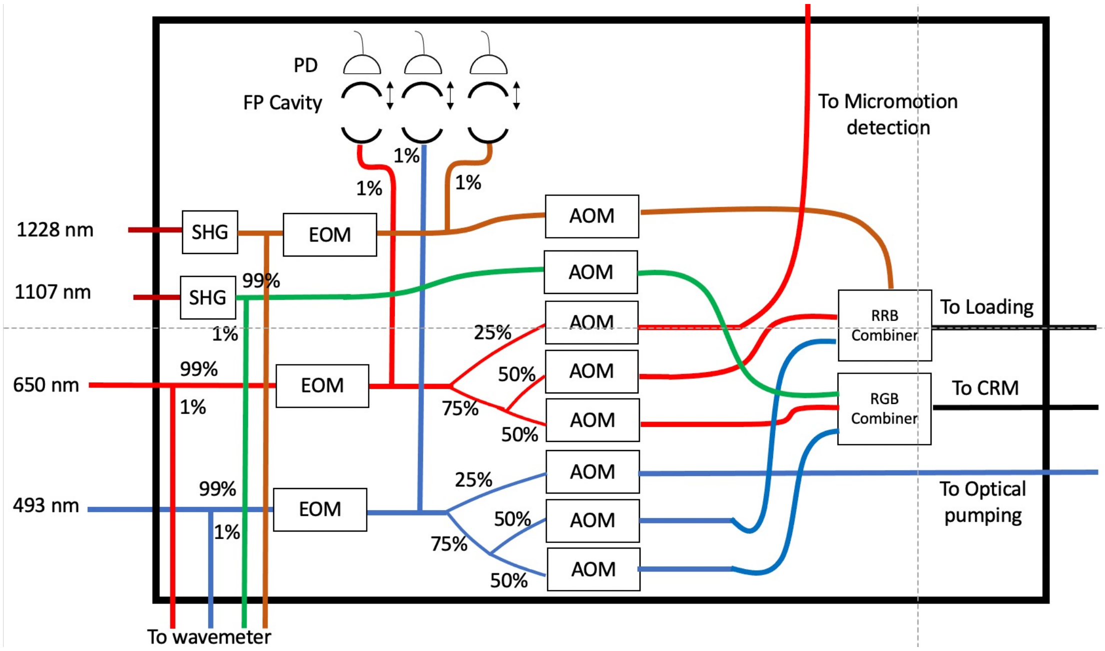

Figure 3.5: Schematic of the beam-prep drawer of the laser rack. The lines denote fiber optic cables, colored to reflect the wavelength of light propagating down each. The splitting is done using fiber based evanescent beam splitters. Light from each of the 4 CW lasers is brought to this drawer through fibers. EOMs add sidebands for addressing several transitions between hyperfine states simultaneously and the AOMs provide high bandwidth amplitude modulation. Part of the light from each laser is split off and sent to the wavemeter section of the rack for frequency stabilization. The sidebands of the EOMs are monitored using a set of scanning Fabry-Perot cavities. The light is then sent through fibers to several beam path on the optics table, to be then focused onto the ions.

3.3.2 Beam delivery boards

The light out of the beam-prep drawer is sent to multiple beam paths on the table, arranged around different ports of the vacuum chamber. These beam paths are built out of custom machined aluminum breadboards, just like the laser rack fiber coupling modules. An example is shown in figure 3.6. This particular board is used to focus the optical pumping 493 nm light out of the beam-prep drawer and the 405 nm light onto the quantum and loading zones respectively.

On the 493 nm side, light from the laser rack is coupled back to space and then collimated using a collimator from Schäfter+Kirchhoff. Part of this beam is then sampled for monitoring with a photodiode and the rest passes through a half-wave plate on a motorized rotation mount and PBS that are used to control its intensity. The output intensity is also sampled with a photodiode, to provide feedback for intensity control. Next, a half-wave plate and quarter-wave plate are used to set the polarization of the beam. After the wave-plates, a motorized filp-mirror is used to deflect light from it's main path for measurement on a camera. A mirror is used instead of a beam-splitter/sampler, to maximize the amount of light reaching the ions. Light continuing down the main path then passes through a motorized shutter which is used to completely block the light from reaching the ions, to account for the finite extinction ratio of the AOMs. This is included as light leakage can reduce the coherence time of the ions. A telescope consisting of a set of cylindrical lenses is used to create an elliptical beam profile so that all the ions can be addressed simultaneously. After the telescope, light is focused down to the ion chain using a single spherical 500 mm focal length lens. This lens is placed on a motorized translation stage (Newport AG-LS25) that moves the optic in the direction of light propagation. This stage has a travel range of 12 mm and < 1 μm step size which is more than enough precision for aligning the focus at the ions. This is used to make small adjustments to the position of the lens so that the focus of the beam directly coincides with the ion chain. Part of the light after the focusing lens is sampled and sent to a beam position sensor from thorlabs (PDP90A), placed 500 mm from the lens, just like the ions. This is used to detect drifts in the beam position at the ions, which are then compensated for using the two motorized mirror mounts after the focusing lens. The light on the 405 nm side passes through a similar set of components. A dichroic mirror, used to transmit the 493 nm light and reflect the 405 nm light, combines and sends both beams through a viewport on the vacuum chamber and then onto the ion trap.

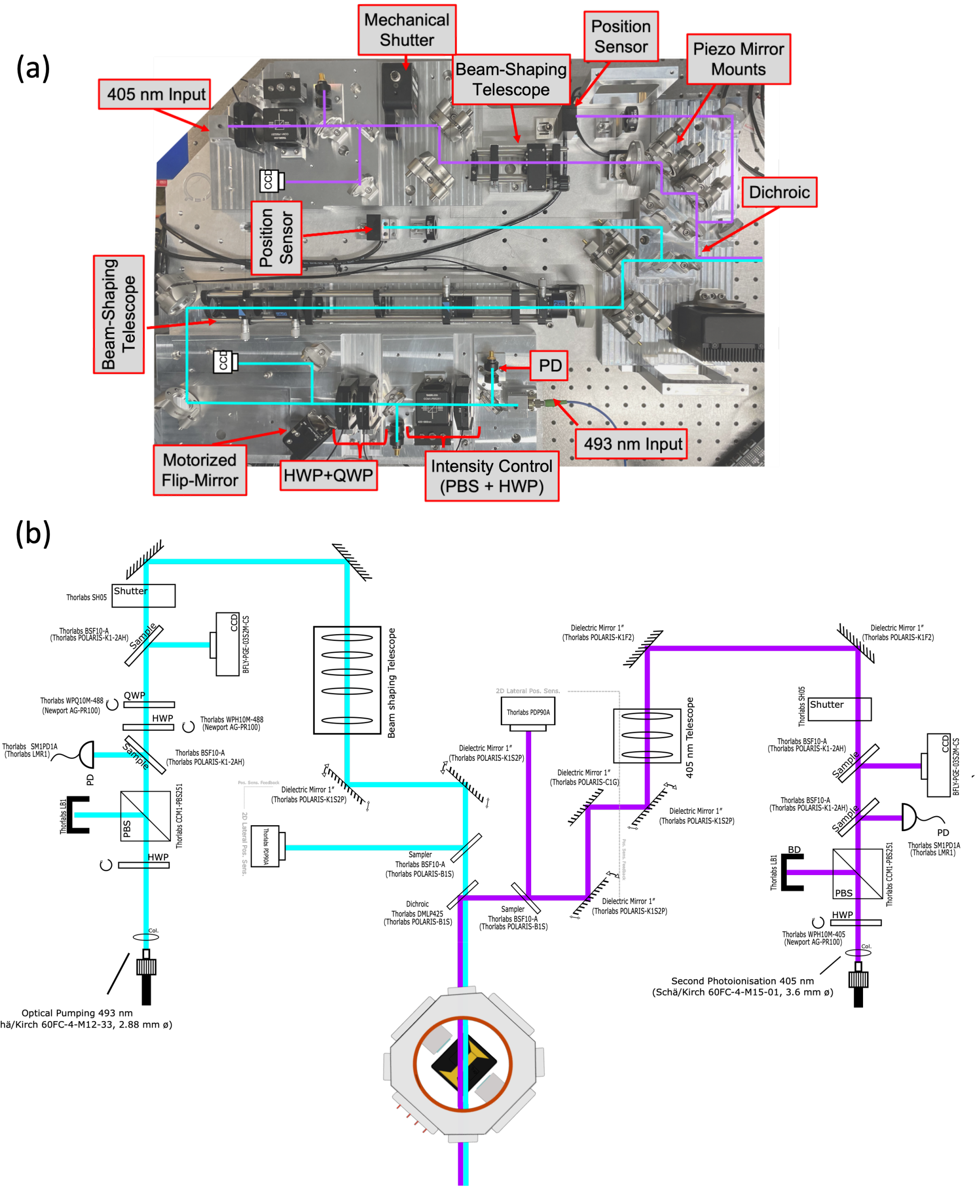

Figure 3.6: (a) Board for focusing and positioning laser beams onto the ions. Light is delivered to each board through fibers from the laser rack. The board shown here delivers circularly polarized 493 nm light to the quantum zone and 405 nm light to the loading zone. The black and white graphics superimposed on the image are placeholders for missing equipment. (b) Optical schematic for the setup shown in (a). This was adapted from the schematic made by PhD student Noah Greenberg.

A very similar setup is used to direct other beam paths out of the beam-prep drawer and focus them onto the ions, with the exception of the micromotion detection beam which passes through the imaging system. A schematic of the experimental chamber and all the different beams being focused onto the loading or quantum zones of the trap by these boards are shown in figure 3.7. From the figure we see that the CRM beam (493, 614 and 650 nm) makes an angle of 45° to the ion chain at the quantum zone. The 493 nm optical pumping beam intersects the chain 90° to CRM. The 405 nm beam which enters the chamber through the same port, makes an approximately 5° angle with the optical pumping beam and hits the loading zone at 40° relative to the trap axis.

The natural abundance target is oriented such that the atomic cloud generated through ablation travels approximately orthogonal to the loading beam. This minimizes the Doppler shift on the first photoionization (553 nm) transition. Since the exact frequency of the second photoionization beam does not matter, it is oriented approximately parallel to the direction of the atomic cloud. Once ions are trapped in the loading zone, the 493 and 650 nm frequencies of the loading beam are used to cool them. The global and individual addressing Raman beams are counter propagating and oriented 90° to the ion chain, to maximize the coupling to the radial modes. Finally, fluorescence is collected from the ions in both the loading and quantum zone, through the central port of the chamber. The ports used for the Raman beams as well as for ion imaging use re-entrant vacuum windows. These ports, shown in figure 3.7 (b), are used to bring the focusing optics as close as possible to the ions, to maximize the available NA. The proximity of the Raman re-entrants are limited by the need to avoid clipping beams entering from other ports of the chamber. Even if this was not the case, the viewports cannot be brought arbitrarily close to the ions as charge build up on any dielectric surface leads to a stray electric field that modifies the trapping potential and can lead to heating of the ion. To screen these fields, a metal shield is built around the trap structure. Sandia recommends that the surface of this shield and the surface electrodes be separated by at least 20 times the ion height so that this ground plane has negligible impact on the trap potential [112]. This sets the limit on how close the imaging re-entrant can be brought to the ions. An alternate solution is to coat the windows with some transparent conductor like ITO but this was decided against because ITO lowers the transmission coefficient of the window [51, 112]. With the current geometry of the trap, the imaging port has a maximum NA of 0.6 and the Raman ports have a maximum NA of 0.37 parallel to the trap and 0.11 orthogonal to the trap.

Figure 3.7 also shows the location and orientation of magnetic field coils placed near the chamber. There are 6 coils in total, the two placed above and below the chamber are not shown. The magnetic field is used to set the quantization axis of the experiment, typically taken to be parallel with the field. The π and $\sigma^{\pm}$ components of the polarization of beams interacting with the ion are then defined with respect to this axis. In our experiments the magnetic field direction is set to be perpendicular to the CRM beam or parallel to the Raman beams. In the former configuration, the optical pumping beam will have no π-polarization components. Using pure $\sigma^{\pm}$ polarized light, this configuration can be used to optically pump $^{137}\mathrm{Ba}^{+}$ to one of the stretch states ($m_f = \pm 2$) of the $S_{1/2}$ F=2 manifold, depending on whether σ^{+} or σ^{-} light is used. On the other hand, the CRM beam has all polarization components. So this configuration is useful for working with $^{137}\mathrm{Ba}^{+}$ as a qudit. The latter configuration, with the magnetic field parallel to the Raman beam (so called lin-perp-lin configuration), can only be used for qubit operations with $^{133}\mathrm{Ba}^{+}$ but is necessary for maximizing the Rabi frequency in Raman transitions. It turns out that the Rabi frequency has no dependence on the π-polarization component of the Raman beams. So by removing this polarization component from the beams, the power in the $\sigma^{\pm}$ components is increased and so is the Rabi rate as a result. The other two coils are used to cancel out stray magnetic fields such as Earth's < 1 G field.

A second benefit of introducing a magnetic field is the destabilization of dark states. When two lower levels are coupled by two beams that are equally detuned from a third excited state, the system's state can be pumped into a superposition of the two lower levels, uncoupled from the excited state. This is called a dark state. In our case, the 493 and 650 nm beams couple the $S_{1/2}$ and $D_{3/2}$ states to the $P_{1/2}$ excited state. During cooling and measurement, we want the ion to continuously scatter 493 nm light. However, a dark state between the $S_{1/2}$ and $D_{3/2}$ levels can form that is uncoupled from the $P_{1/2}$ transition [125]. Dark states can also form between Zeeman sublevels of the $D_{3/2}$ state, decoupling it from the $P_{1/2}$ level [15]. In either case the ion stops scattering light and goes dark. By lifting the degeneracy between the Zeeman sublevels using a magnetic field, we can prevent the dark state from forming [15].

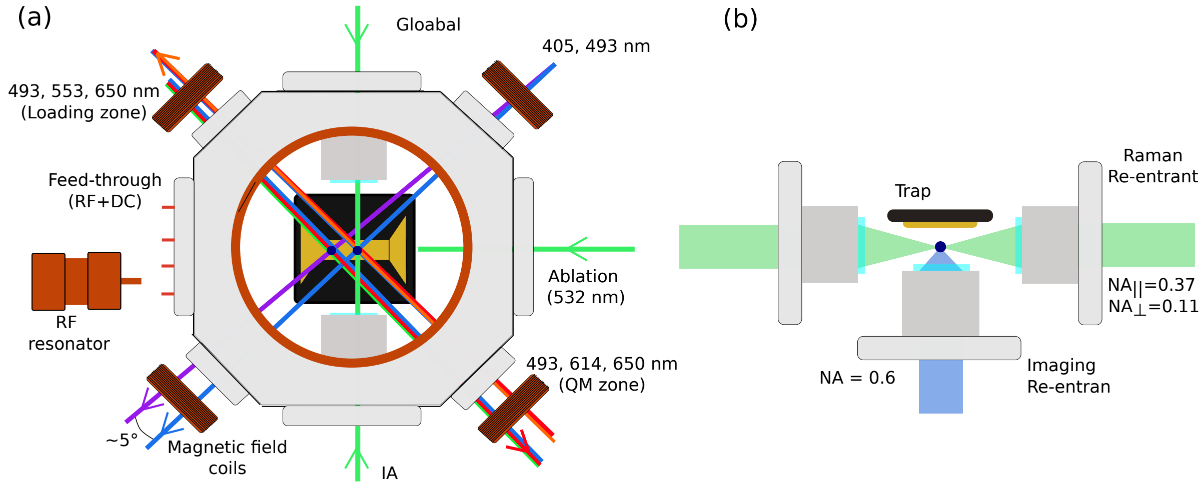

Figure 3.7: Left: Schematic of the experimental chamber and all the beams being focused onto ions in the loading zone (left) or quantum zone (right) of the trap. Right: Available NA at each of the three re-entrants windows. Re-entrants are used to bring the objectives as close as possible to the ions in-order to maximize the NA. Bringing the Raman re-entrants any closer would cause the CW beams entering through the other ports to clip the re-entrant. The proximity of the imaging re-entrant is constrained by the need of having a grounding shield around the trap. This is to nullify the effect of any stray fields at the ions due to charge build up on the window.

3.3.3 Overview of the imaging system

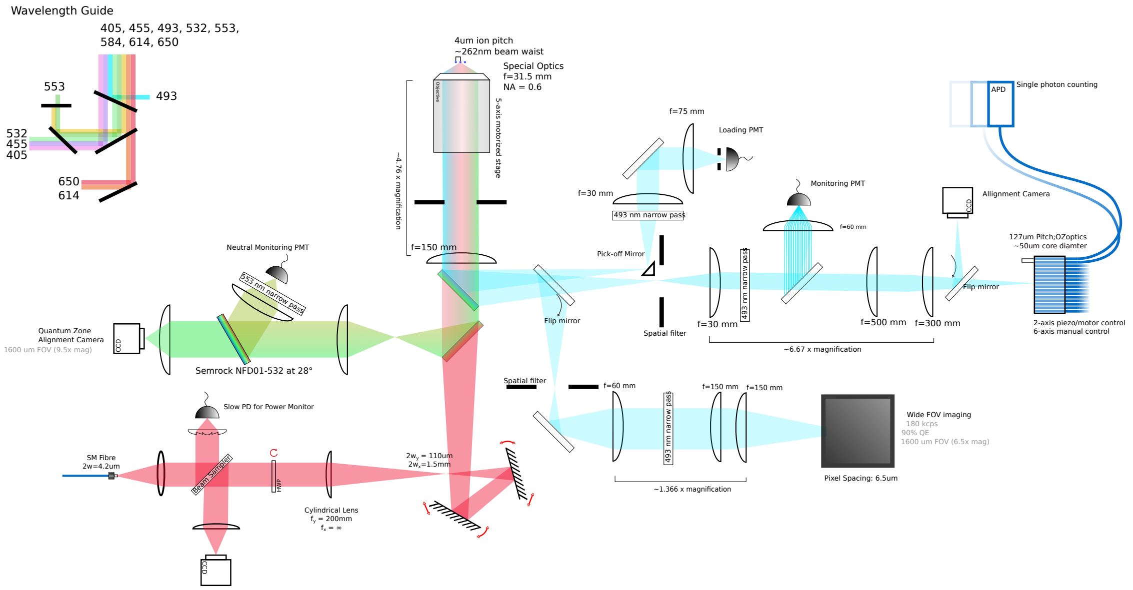

Figure 3.8: Schematic of our imaging system used to collect ion (493 nm) and neutral atom (553 nm) fluorescence. The beam at 650 nm is sent up through the imaging system and used for micromotion compensation. This figure was adapted from one made by Dr. Matt Day and master's student Nikolay Videnov.

The schematic of our imaging system is shown in figure 3.8. The fluorescence from the ions is collected by a microscope objective and then relayed to a 150 mm focal length lens, providing a magnification of around 4.76x. The objective lens is a custom optic from Special Optics with a NA of 0.6, focal length of 31.5 mm and a working distance of 19 mm (11.023mm Vacuum + 5±0.01mm glass + 3mm air). The objective is attached to the 150 mm lens through a lens tube and the two are clamped to a custom 5-axis stage that is used to control the exact position of the objective inside the re-entrant. This microscope objective positioning system is shown in figure 3.10. The system consists of a Newport 562-XYZ ULTRAlign stage for linear translation and two GOHT-60A-S goniometers, with an angular range of ±3°, from OptoSigma to provide rotation about the ions. An L-shaped cantilever is used to place the two goniometers at 90° to each other, providing angular control about the two horizontal axes. Counter-weights were added to the side opposite the cantilever to minimize the torque about the goniometer to which the cantilever is attached. Given the NA of the objective, the depth of focus for 493 nm light is around 500 nm. So we need to control the vertical position of the objective with $< 1\mu$m resolution. This is achieved using 8301NF Newport picomotors which have a step size of < 100 nm. These motors are also used for positioning of the other axes and allow us to automate the alignment process. The picomotors have a limited axial load capacity of 22 N but the weight of the stage is greater than this maximum. To correct for this, three spring plunger screws, with a compressed force of 20 N each, are used to reduce the load that the z-axis picomotor has to push. Control over the exact position and angle of a high NA objective is very important as even the smallest misalignments can cause significant aberrations. Motorized operation of this device is not only good for automation but a necessity in our system as the objective is in a difficult to access location. The entire imaging system is placed inside a trench at the center of our custom optics table (see figure 3.9). A student trying to manually adjust the objective will not only run the risk of misaligning the surrounding optics but will also be exposed to radiation from radioactive barium.

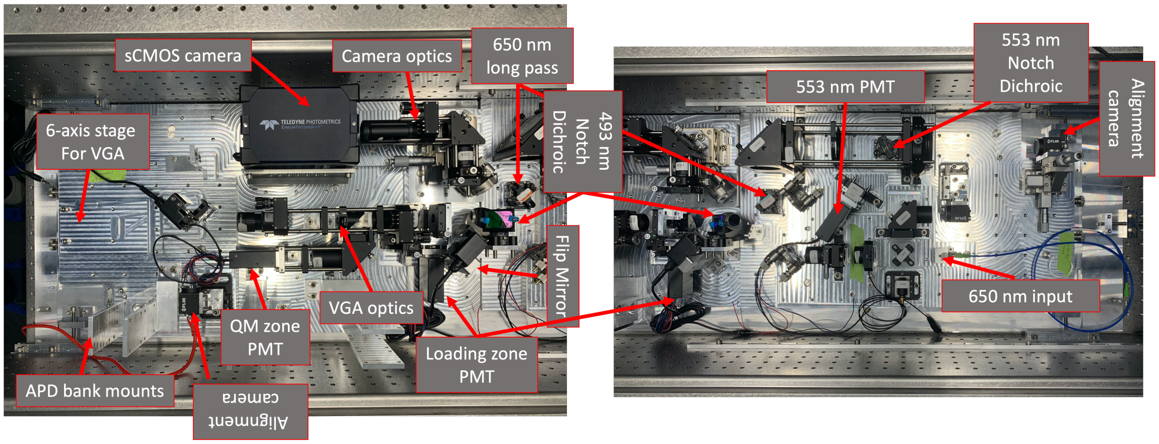

Figure 3.9: Left: Details of the 493 nm arm of the imaging system, consisting of the imaging camera, PMTs and a fiber array for sending light from the ions to an array of avalanche photodiodes (fiber array stage and APDs currently missing from setup). Right: The 650 nm and alignment arms of the imaging system. The former we use for micromotion compensation by sending 650 nm light up to the ions and the latter we primarily use for detecting 553 nm neutral fluorescence during photoionization.

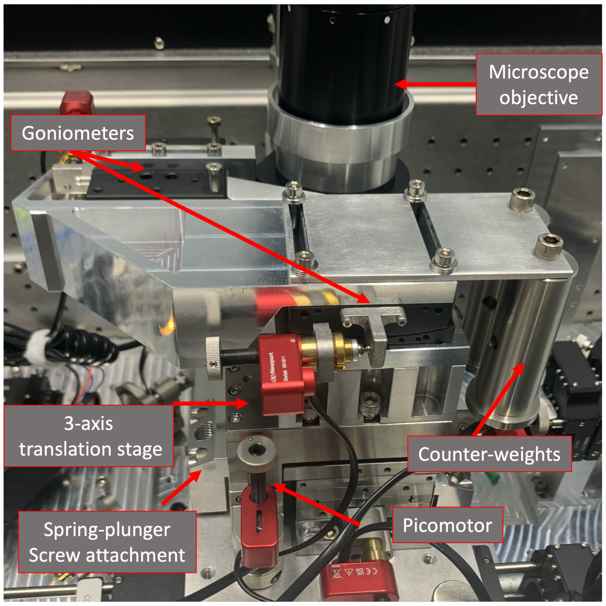

Figure 3.10: Details of the microscope objective alignment system.

After the 150 mm lens, the light passes through a 45° notch dichroic that reflects 493 nm light and transmits all of the other colors. This right arm of the imaging system is used to detect the 493 nm light scattered from ions in the loading and quantum zones. A flipper mirror can be used to send light to a camera. In this path, a set of lenses are used to magnify and image the beam onto the sensor, providing a magnification of 1.366x, yielding a total magnification of 6.5x. Given the objective NA of 0.6, the expected diffraction limited spot size is $\sim 0.41\mu$m at 493 nm. The 6.5x magnification yields a beam radius of 2.7 μm on the camera. Each ion is given a single pixel on the camera to minimize crosstalk/overlap of the point spread functions as well as to maximize the intensity falling onto a single pixel for higher signal to noise ratio. The camera is a Teledyne Photometrics Prime BSI with 6.5 μm pixels and a quantum efficiency of 90% at 493 nm. If the flip mirror is removed, light can continue down other beam paths on the 493 nm arm. Light from the loading zone of the trap, located around 1 mm from the quantum zone (around 5 mm after magnification), is picked off using a right-angle prism mirror and separated from light from the quantum zone. This light is sent through a 493 nm band-pass filter to block out any other wavelengths that may be present and then is focused onto a photomultiplier tube (PMT), we call the loading PMT. All PMTs in this project are the Hamamatsu H12775. On the other path, a set of lenses are used to image the light from each ion, using a 6.67x magnification imaging system, onto one channel of a multi-mode fiber array. The fibers are packaged together and spaced apart by 127 μm using a v-groove array by Oz Optics. The combined magnification from the ions to the fiber facets is 31.75x, mapping the 4 μm pitch of the ions to the 127 μm pitch between the fibers. Each fiber then delivers light from one ion to an avalanche photo diode (APD). This system can be used for site-resolved quantum state measurement. The camera can also be used for this purpose but the higher bandwidth of the APDs means that it can be used for mid-circuit feedback i.e. modifying the execution of a quantum algorithm based on measurement on a subset of the ions. This is necessary for error correction schemes. In our setup, measurement of a subset of ions can be done through shuttling, but the use of a tightly focused 493 nm beam may be explored. The fiber array is placed on a 6-axis stage from Newport to help align the fiber cores to the ion light. A flip mirror is used to send light to a camera just before the fiber array to help with alignment. 1% of the light sent towards the fiber array is sampled and focused onto another PMT. This provides information on the number of bright ions but it cannot be used to detect the state of any individual ion.

The light transmitted through the first dichroic then arrives at a long pass dichroic that transmits any light with wavelength greater than 600 nm. In our setup, this refers to 614 and 650 nm. The remaining wavelengths, 405, 532 and 553 nm are reflected. In this path, a notch dichroic reflects the 553 nm beam to a PMT. Detection of 553 nm fluorescence signals the generation of neutral barium by ablation when the atoms interact with the 553 nm light in the loading zone. This will be an important quantity to monitor and maximize when we first attempt to trap ions. The other wavelengths are transmitted by the notch filter and imaged onto a camera.

The final arm of the imaging system is not intended for the detection of fluorescence at 614 or 650 nm but for micromotion compensation in the direction perpendicular to the trap surface. This is done by sending 650 nm light back through the imaging system and up to the ions. A single 200 mm cylindrical lens, combined with the 150 mm lens and the objective, generate a beam waist at the ions of 158 μm along the chain and 11.5 μm perpendicular to the chain. The micromotion of the ion imparts sidebands on each transition, detuned by the RF drive frequency. By scanning the frequency of the 650 nm beam and observing the 493 nm fluorescence counts on a PMT at each point, these sidebands can be resolved since the drive frequency in our case is 45 MHz and the linewidth of the 650 nm transition is around 20 MHz. By tuning the DC electrode voltages and monitoring the amplitude of the sidebands, excess micromotion caused by electric field noise can be attenuated. If there is significant micromotion, then the 493 nm light is driven well above saturation to broaden the transition but the 650 nm light should be kept below saturation so that the sidebands can be resolved. Other techniques for micromotion compensation that we could use include using a time tagger device to obtain time dependant 493 nm fluorescence counts on a PMT. If there is significant micromotion along the direction of the 493 nm beam, then one will observe modulations of the signal at the RF drive frequency due to the Doppler shift. The amplitude of this modulation can be used as feedback for tuning the DC electrode voltages [16].

3.4 Basic Manipulation of the Ba^+ ion

In this section we will discuss how the barium ion is laser cooled, how a pure quantum state of the qubit is prepared for quantum information, and how this state is read-out. These operations all make use of the beam paths discussed in the previous sections and are shown in figure 3.11. Coherent manipulation of the qubit for single and two-qubit operations is the subject of the next chapter.

Measurement of the $^{133}\mathrm{Ba}^+$ qubit ($|0\rangle \equiv \left|\mathrm{S}_{1/2}; F=0, m_f=0\right\rangle$, $|1\rangle \equiv \left|\mathrm{S}_{1/2}; F=1, m_f=0\right\rangle$) is done by driving the transition between the F=1 states of the $S_{1/2}$ manifold and the F=0 state of the $\mathrm{P}_{1/2}$ manifold. Taking advantage of the fact that a $F=0 \to 0$ transition is not allowed, if the ion is in state $|1\rangle$ then it will continuously fluoresce and if it is in the $|0\rangle$ state, the ion will scatter no light as the beam is far off resonance. 650 nm light, resonant with $\left|\mathrm{D}_{3/2}; F=1\right\rangle \to \left|\mathrm{P}_{1/2}; F=0\right\rangle$ transition is used to repump out of the metastable state. The fidelity of this scheme is limited by off-resonant scattering to the $\left|\mathrm{P}_{1/2}; F=1\right\rangle$ state.

Preparation of the $^{133}\mathrm{Ba}^+$ qubit in the $|0\rangle$ pure state can be done by only driving the $\left|S_{1/2}; F=1\right\rangle$ state to the $\mathrm{P}_{1/2}$ level. This way, due to decay from $\left|\mathrm{P}_{1/2}; F=1\right\rangle$ to $\left|\mathrm{S}_{1/2}; F=0\right\rangle$, all the population eventually ends up in the $|0\rangle$ state. The fidelity of this process is limited by off resonant coupling of the 493 nm light to the $\left|\mathrm{S}_{1/2}; F=0\right\rangle$ level. This time both the $\mathrm{D}_{3/2}$ hyperfine levels need to be repumped because the $\left|\mathrm{P}_{1/2}; F=1\right\rangle$ state, which can decay to either of the $\mathrm{D}_{3/2}$ hyperfine states, is excited. Finally, Doppler cooling of the $^{133}\mathrm{Ba}^+$ qubit is done by exciting both hyperfine states of the ground $\mathrm{S}_{1/2}$ level, with repumping done in the same way as in state preparation.

State preparation in $^{137}\mathrm{Ba}^+$ is done by driving the transitions shown in figure 3.11 and using purely σ^+ or σ^- polarization for the 493 nm transition. In the case of purely σ^+ light, all Zeeman states of the $S_{1/2}$ manifold are depopulated except for the $m_F=2$ state of the $F=2$ hyperfine level. Thus, eventually all the population ends up in the $m_F=2$ state as it decays from the $\mathrm{P}_{1/2}$ level. Using σ^- light, we instead prepare the $m_F=-2$ state. Once, prepared, two microwave π-pulses of appropriate polarization can be used to prepare the $F=2, m_F=0$ clock state. This state, along with the $F=1, m_F=0$ hyperfine state can be used to encode a qubit, or by including the other Zeeman sublevels in the $\mathrm{S}_{1/2}$ manifold, for a total of 8 states, we could encode a qudit. Alternatively, pure π light can be used to directly prepare the $F = 2, m_F = 0$ state by taking advantage of the selection rule that $m_F = 0 \to m_F = 0$ is not allowed for $\Delta F = 0$ [42]. This is also possible in our system, using the 493 nm light in the CRM path which can be made purely π polarized in the qudit magnetic field configuration. The same exact set of transitions can be used for cooling the 137 isotope but now all polarization components are used to pump all Zeeman sublevels of the $\mathrm{S}_{1/2}$ manifold. Measurement can be done by shelving one of the two qubit states to the $\mathrm{D}_{5/2}$ level, say the $|1\rangle$ state. Detection of fluorescence upon Doppler cooling then implies that the ion was in the $|0\rangle$ state. Here the fidelity is limited by the fidelity of the shelving operation and the efficiency of the collection optics. High efficiency light collection would allow for a shorter detection window, thereby minimizing the infidelity caused by spontaneous emission out of the $\mathrm{D}_{5/2}$ state. To measure a qudit, all but one state is shelved to the $\mathrm{D}_{5/2}$ level. Detection of fluorescence during Doppler cooling implies that the qudit was in the un-shelved state. If no fluorescence is detected, then one of the states in the $\mathrm{D}_{5/2}$ level is un-shelved and the fluorescence detection is repeated. This process is repeated until the quantum state of the qudit is known [19].

This same shelving technique can be used for state detection in $^{133}\mathrm{Ba}^+$, yielding higher fidelity than the previously described hyperfine-selective optical cycling [27]. Shelving can be done coherently by driving a π pulse on the narrow linewidth 1762 nm transition or dissipatively, via decay from the $\mathrm{P}_{3/2}$ to $\mathrm{D}_{5/2}$ level. The latter technique requires the use of a 455 nm laser to excite the desired $\mathrm{S}_{1/2}$ level to the $\mathrm{P}_{3/2}$ level. Since around 3% of the population can decay to the $\mathrm{D}_{3/2}$ level, 585 nm and 650 nm light must be used to pump out of this state. Eventually, all the population ends up in the $\mathrm{D}_{5/2}$ state. This latter scheme is more feasible for $^{133}\mathrm{Ba}^+$ due to the simpler hyperfine structure.

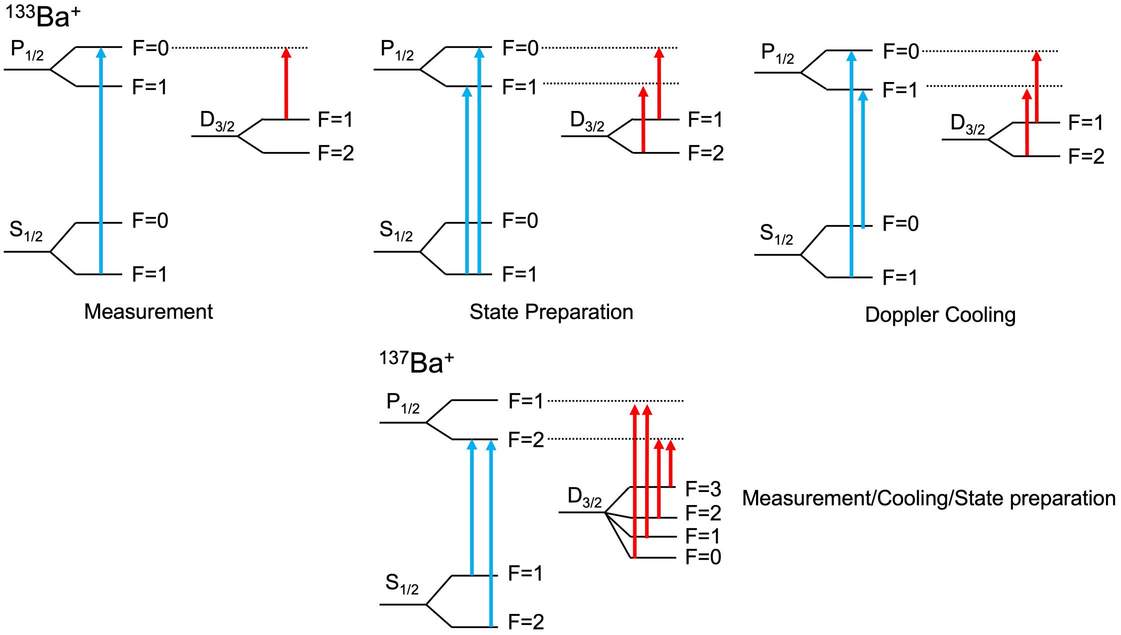

Figure 3.11: Basic manipulation of the 133 and 137 isotopes of Ba$^+$. The blue (red) arrows denote the required sidebands for 493 nm (650 nm) light.

The multiple transitions between the hyperfine levels of different states are driven by imparting the laser beams with appropriate sidebands using EOMs. The choice of the EOM modulation frequency depends on the choice of the frequency of the carrier. The case where both the 493 and 650 nm carriers are set on resonance with the corresponding transitions in ^{138}Ba$^+$, ω_0, is shown in figure 3.12 as an example. The transitions between hyperfine levels for ^{133}Ba$^+$ are shown in green and those for the ^{137}Ba$^+$ ion are shown in purple. The sidebands required for Doppler cooling, imparted by the EOM to the 493 nm light, are shown in blue in figure 3.12 (a). There are 4 bands in total because for each tone ω_i on the EOM, there are two first order sidebands, $\omega_0 \pm \omega_i$. So two of the tones drive the required transitions between hyperfine states, while the other two are idle, and can result in off-resonant coupling. By artfully picking ω_0, these idle sidebands can be pushed as far away from the available transitions as possible. For example, by picking the carrier to be halfway in between the two driven transitions, only a single tone is required on the EOM, and there are no idle sidebands. Since one of the Doppler cooling transitions in ^{133}Ba$^+$ is very close to a transition in ^{137}Ba$^+$, ^{133}Ba$^+$ cannot be used as a coolant/communication qubit, when ^{137}Ba$^+$ is used as the memory, however, the reverse is possible, since the

$F = 1 \rightarrow 1$ transition in $^{137}\mathrm{Ba}^+$ does not need to be driven for any operations.

The transitions between hyperfine levels of the $\mathrm{D}_{3/2}$ and $\mathrm{P}_{1/2}$ states for $^{133}\mathrm{Ba}^+$ and $^{137}\mathrm{Ba}^+$ are shown in figure 3.12 (b). The sidebands shown correspond to those required for cooling $^{133}\mathrm{Ba}^+$ with the carrier placed at the $^{138}\mathrm{Ba}^+$ frequency. Cross-talk between the two isotopes does not matter in this case since quantum information is typically encoded in either the $\mathrm{S}_{1/2}$ ground state or the $\mathrm{D}_{5/2}$ metastable state and the 650 nm laser is far off-resonant from any transitions involving those states. Figure 3.12 (c) depicts the same transitions as in (a) but now instead indicating the sidebands required to cool $^{137}\mathrm{Ba}^+$. As discussed, this will not decohere a qubit stored in the $\mathrm{S}_{1/2}$ state of $^{133}\mathrm{Ba}^+$.

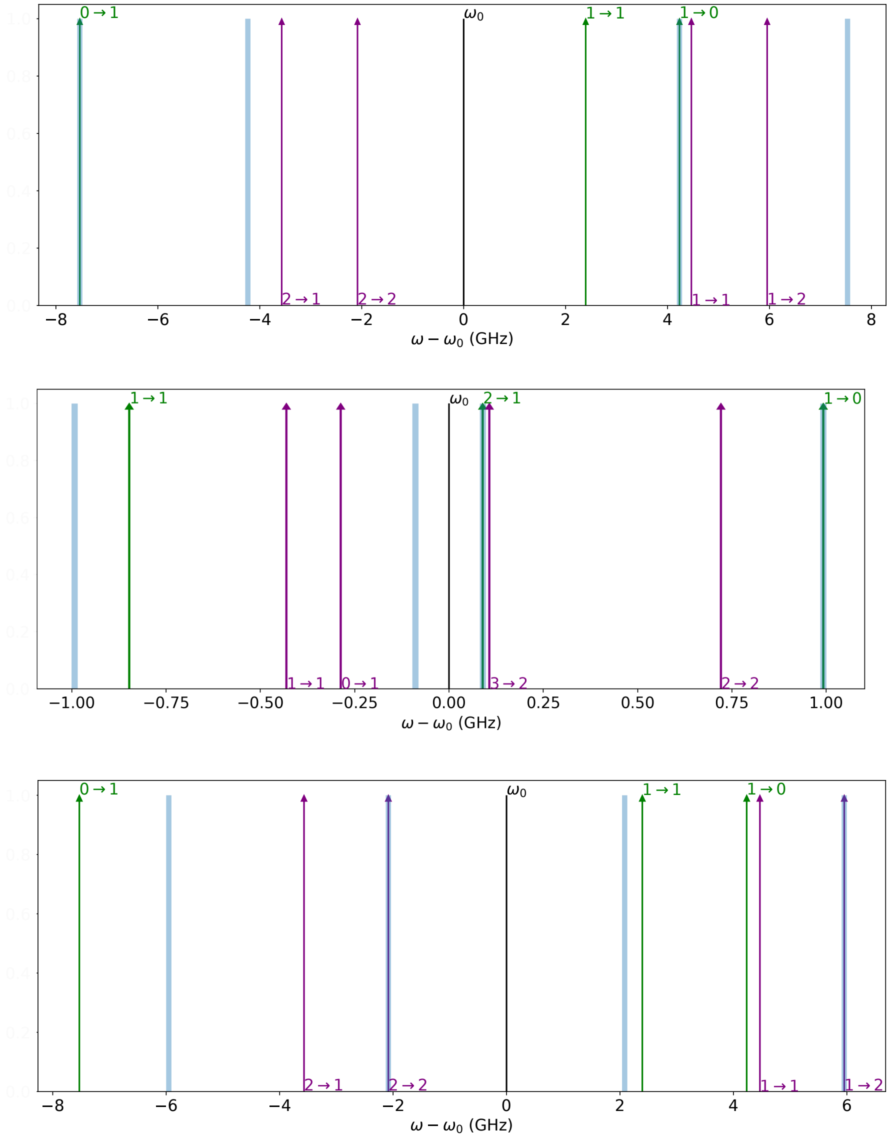

Figure 3.12: Positions of the hyperfine transitions in ^{133}Ba$^+$ (green) and ^{137}Ba$^+$ (purple) relative to the ^{138}Ba$^+$ transition frequency, ω_0. (a) Denotes the frequencies for the 493 nm transition. The transparent blue vertical lines, placed symmetrically about the carrier ($\omega = \omega_0$) denote the required sidebands, imparted by the EOM, for cooling ^{133}Ba$^+$. (b) Shows the required sidebands on the 650 nm repump transition for cooling ^{133}Ba$^+$. (c) Shows the required sidebands on the 493 nm transition if we instead wanted to cool ^{137}Ba$^+$, for comparison with (a).

3.5 Beam delivery telescopes

3.5.1 High dynamic range beam profiling

An understanding of the level of optical cross-talk between the loading and quantum zones of the trap is essential if we want to perform operations in both regions simultaneously. For example, if we want to cool ions in the loading zone while performing a quantum algorithm in the quantum zone, the leakage of the 493 nm light to the quantum zone can destroy the quantum information being processed in this region. This can be fixed by interleaving the cooling and gate operations. An understanding of the beam profile orthogonal to the ion chain is also important. If a significant amount of light clips the trap electrodes, the resulting light scatter can contribute to noise on the detection signal. One way to assess the impact of this cross-talk is to use the ion itself as a sensor, by shining the cooling/measurement light on a desired ion and looking at its effect on a neighbouring ion. The decoherence rate, measured say by the fringe contrast in a Ramsey experiment, as a function of the ion-ion separation can provide a quantitative estimate of the effects of cross-talk. However, since we are not yet at the point of trapping and shuttling ions, we need to resort to other means of assessing the quality of our optics.

In particular we use a camera to measure the profile of the optical beams at the location of the ions. A typical sensor does not have enough dynamic range to allow us to determine the cross-talk at one zone of the trap due to a beam turned on at the other. This is circumvented by taking several images at different exposure times and stitching these together. In the shorter exposure time images, bright objects in the scene will be in clear view while while darker features will not be clear. In the long exposure time images, the darker objects come into clear view while the bright ones saturate the sensor. Composing these images yields the HDR images.

To stitch the images at different exposure times together, we need to find a relationship between the laser power P and the intensity as measured by the CCD, $I_{CCD}(t_E)$ for each exposure time t_E. The intensity of a gaussian beam $I \propto P \cdot e^{-2x^2/\omega(z)^2}$. So assuming a linear response for the sensor, the maximum intensity measured by the camera at a given exposure time, $S(t_E)$, is proportional to the power in the beam: $S(t_E) - B(t_E) = C^{t_E} \cdot P$ where C^{t_E} is the proportionality constant and $B(t_E)$ is the average background signal, obtained by averaging the value of every pixel in the absence of a laser. In order to compute the calibration constant for a given exposure time, we measure $S(t_E) - B(t_E)$, as a function of power. The slope of this line is C^{t_E} and this allows us to convert from the camera's intensity units in ADU to physical units. Figure 3.13 shows sample plots for exposure times $t_E = 0.01, 1, 10ms$.

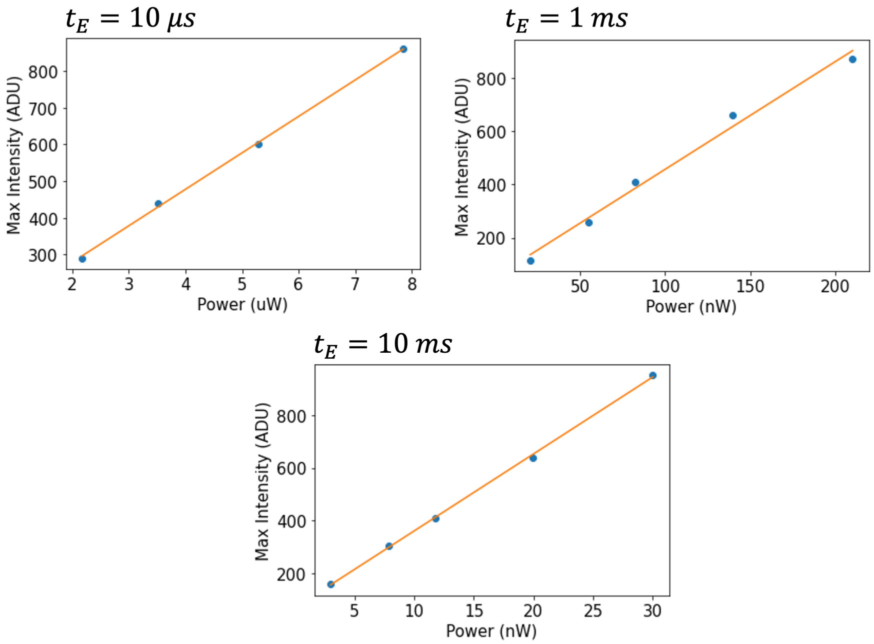

Figure 3.13: Camera response as a function of laser beam power for several exposure times. The slope for each exposure time can be used to relate the intensity measured by the camera in ADU to physical units. This can then be used to stitch the profiles from each exposure time together into a single profile.

Once the calibration constants are known,the HDR profile can be obtained. We fix the power of the laser so that the sensor's ADC is nearly saturated at the lowest exposure time and capture this image and the other (saturated) images at the larger exposure times. The calibrated image at each exposure time is given by $(S(t_E)-B(t_E))/C^{t_E}$. This is illustrated in figure 3.14.

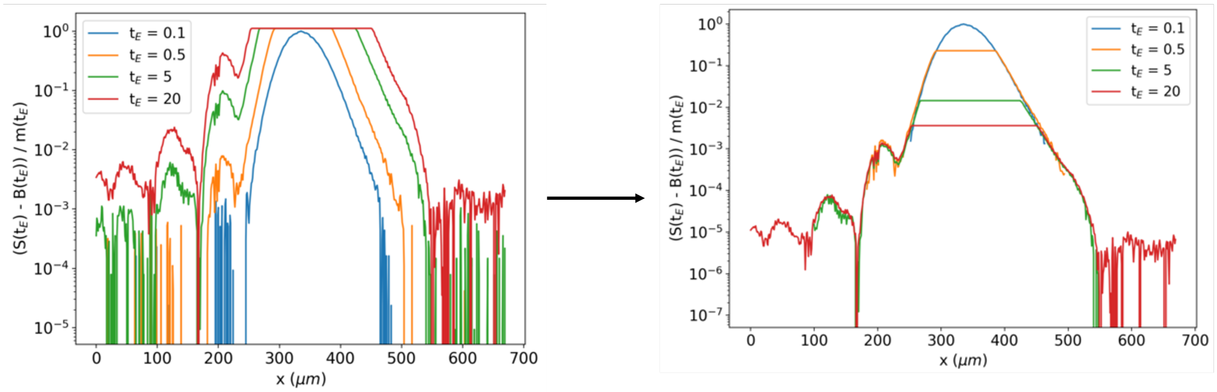

Figure 3.14: An example of a high dynamic range beam profile before and after calibration.

3.5.2 Telescope design and characterization

The schematic of the cylindrical beam shaping telescopes is shown in figure 3.15 (a). This telescope is used in the CRM, loading and 493 nm optical pumping paths. Their purpose is to stretch the beams along the ion chain, so that all the ions experience approximately the same intensity, and squeeze them in the direction perpendicular to the chain to allow the beams to clear the surface of the trap without appreciable clipping. We are planning to have 16 computational ions in our trap, each separated by 4 μm. So the distance from the center ion to the one at the end is 32 μm. Requiring that these two ions experience the same intensity, to within 90%, constrains the radius of the beam along the ion chain to be greater than about 211 μm. The upper bound on the beam size is set by the level of cross-talk that we can tolerate in one zone, when the lasers are turned on in the other. Requiring an intensity cross-talk level of $<$ 1e-5 and noting that the center of the two zones are separated by 1 mm, the maximum size of the beam is constrained to $<$ 400 μm. This estimation assumes a perfect Gaussian beam; in reality, the effects of diffraction and aberrations should be taken into account which would yield a stricter upper bound but this is a good starting point. In the orthogonal direction, requiring that the beam clips the trap at a relative intensity of 1e-5 or less, leads to an upper bound of 27 μm for the radius of the beam in that direction. Maintaining the amount of light clipped by the trap at a minimum is important because light scatter, particularly at 493 nm, can decohere the qubits.

The beam delivery boards use a pair of mirrors and a beam position sensor after the telescope for automated control over the position of the beam at the ions. The presence of these opto-mechanical components as well as the thick lead shielding, required for using a radioactive species, constrains us to use a relatively long focal length lens for focusing. In our case, this is 500 mm. Given these constraints, a 4 lens cylindrical beam shaping telescope was designed (figure 3.15 (a)). The telescope consists of two cylindrical lenses that demagnify the beam in the direction along the chain. Another pair of cylindrical lenses, oriented 90° to the first, magnify the beam orthogonal to the ion chain. These two sub-telescopes are interleaved to minimize the amount of space they take up. After the beam has been shaped into an ellipse, a 500 mm focal length spherical lens, focuses the light to a beam radius of 220 μm along the chain and 16 μm perpendicular to the chain at 493 nm. At 650 nm, the beam radii are 310 μm and 22 μm respectively which are within the required constraints. The beam profile at the ions generated by this telescope is shown in figure 3.16.

The telescope used to focus the 405 nm light at the loading zone is shown in figure 3.15 (b). In this case the beam profile is kept circular, with a waist of around 19 μm at the loading zone. The small beam size relative to the elliptical beams is intended to lower the fraction of ionized atoms. While this will reduce the ion loading efficiency, having a smaller beam centered at the trap minimum means that most of the ions loaded into the trap will be near this minimum. A bigger beam would ionize atoms further away from the potential minimum as well. After ionization, these ions will experience a larger acceleration that can heat up the ions that have already been loaded into the trap [51].

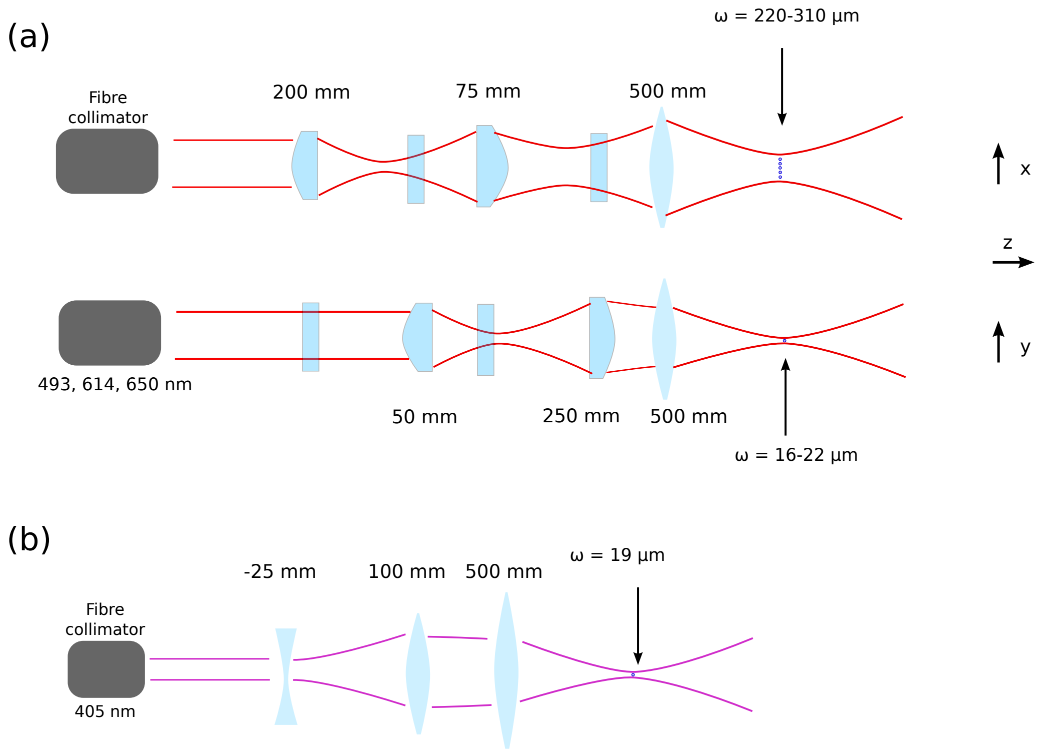

Figure 3.15: (a) Schematic of the achromatic cylindrical telescope used to elliptically shape the beam profile so that all 16 ions in the chain experience approximately the same intensity. This design is used for the loading, optical pumping and CRM beam paths. (b) Schematic of the telescope used for the second photoionization beam (405 nm).

Since beams of different colors will be focused by this optical system, with 493 nm and 650 nm at the extremes, the telescope was designed using only achromatic elements. We measure a focal shift of 34 μm between 493 nm and 650 nm. The caustic in figure 3.16 (b) is obtained using a scanning slit beam profiler (DataRay beam R2) placed on a translation stage. This yields a M^2 value of 1.15 and a Rayleigh range of 1.49 mm in the tightly focused direction. For a Gaussian beam, the beam radius grows with distance as $\omega(z) = \omega_0\sqrt{1+(z/z_R)^2}$. Given that the focal shift is much smaller than the Rayleigh range, z_R, this shift has a negligible effect on the size of the beam at the ions.

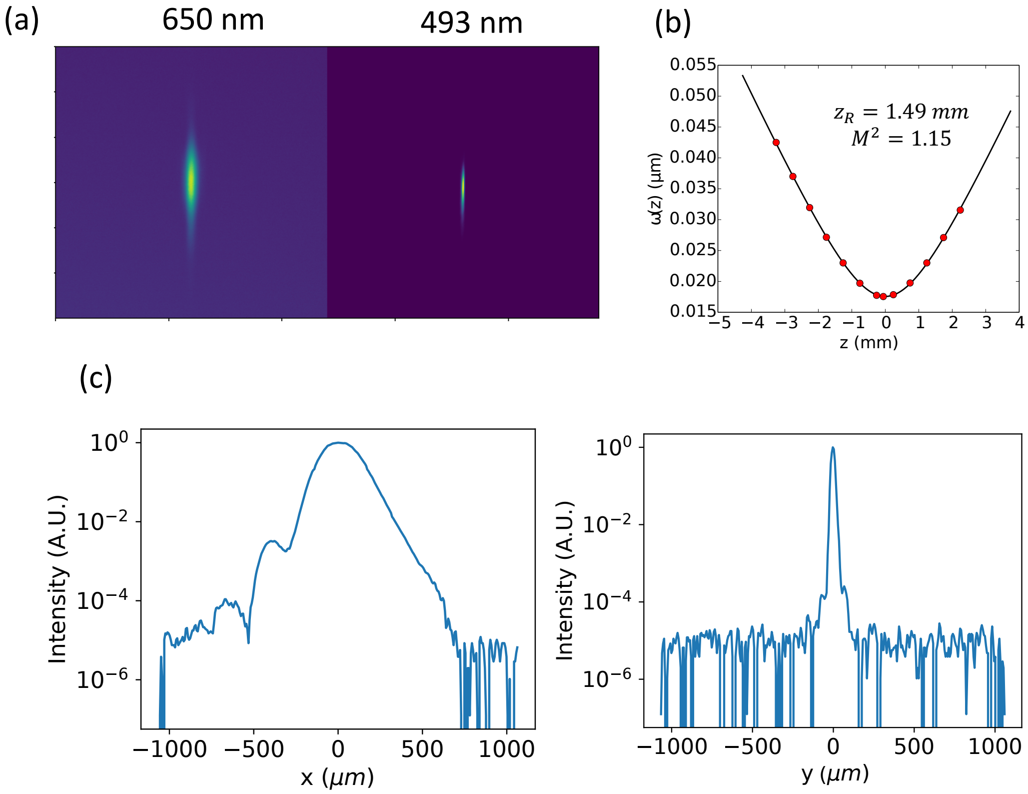

Figure 3.16: (a) Beam profile of 650 nm and 493 nm light at the ion plane, focused by one of the achromatic cylindrical telescopes. Since the beam waist at the focus $\omega_0 \propto \lambda$, the 650 nm beam is larger. (b) Beam caustic near the ion plane, measured along the tightly focused direction (orthogonal to the chain). A fit to the data yields a Rayleigh range of 1.49 mm. (c) HDR cross-sections of the beam profile along (left) and orthogonal (right) to the ion chain.

From the HDR images it is evident that the beam along the ion chain exhibits some coma aberration, due to the asymmetry in the beam profile. This could not be completely removed by optimizing the alignment of the lenses. However, the intensity cross-talk level is still $\sim 10^{-5}$. Further, since the ion chain only extends 32 μm on each side of the beam's peak, this aberration does not affect the uniformity of the intensity across the chain. In the orthogonal direction, the beam has an intensity $\sim 10^{-4}$ at the position of the trap electrodes, leading to a small amount of light scatter.

Now that the beam parameters at the ions are known, we need to make sure that we have enough power in each wavelength to drive the discussed operations. This is characterized by the saturation parameter and the saturation intensity. For a two-level system interacting with a laser field, the steady state population in the excited state, $|1\rangle$, is given by:

$$\rho_{11} = \frac{s/2}{1+s} = \frac{s_0/2}{1+s_0+(\frac{2\Delta}{\Gamma})^2} \tag{3.1}$$

where $s_0 \equiv \frac{2\Omega^2}{\Gamma^2}$ is the on resonance saturation parameter and is proportional to the intensity. The saturation intensity is defined in terms of the saturation parameter as $s_0 = \frac{I}{I_{sat}}$. It can be shown that the saturation intensity is given by [47]:

$$I_{sat} = \frac{\pi h c}{3\lambda^3 \tau} \tag{3.2}$$

Where τ is the lifetime of the excited state $|1\rangle$. On resonance, when $I = I_{sat}$, $\rho_{11} = 1/4$ and as $I \to \infty$, $\rho_{11} \to 1/2$. So increasing the intensity well beyond saturation will not significantly increase the scattering rate from the excited state, instead it will cause the transition to broaden since the full-width at half-maximum line-width of the resonance can be shown from equation 3.1 to be $\Gamma\sqrt{1+\frac{I}{I_{sat}}}$. The $P_{1/2}$ excited state in barium has a lifetime of 7.9 ns. This yields a saturation intensity of 220 W/m^2 and 95.9 W/m^2 for 493 nm and 650 nm respectively. Using the relationship between the maximum intensity and power of a Gaussian beam, $I_0 = \frac{2P_0}{\pi\omega_x\omega_y}$, we can turn this into a requirement for the minimum amount of power needed at the ions. This yields 1.22 μW for 493 nm and 1.03 μW for the 650 nm transition. While the beam size at the focus of a lens scales linearly with wavelength, $I_{sat} \propto \lambda^{-3}$ so the power requirement decreases as λ^{-1}.

3.6 Conclusion

This chapter covered the optical infrastructure built for modulating and focusing down CW light onto the ions. The CW lasers are used for photoionization, qubit measurement, qubit state preparation and Doppler cooling. We covered the details of how these operations are implemented for our trapped ion system. In addition, we discussed how fluorescence is collected from the ion chain for quantum state detection using our imaging system.

Chapter 4

The Raman individual addressing system

4.1 Coherent control with Raman transitions

The qubits in our system are primarily defined in the clock states of the $S_{1/2}$ level. Coherent control of this qubit can be achieved using a microwave horn, emitting a frequency at the qubit's resonance (~ 9.9 GHz for $^{133}\text{Ba}^{+}$). However, this would affect the quantum state of all the qubits at once since the ions are separated by a few microns and the wavelength of the microwave is a few centimeters. Further, microwaves impart a very small momentum kick to the ions, making the strength of the spin-motion coupling, as characterized by the lamb-dicke parameter $\eta \propto \frac{2\pi}{\lambda}$, small. These problems can be solved by optically addressing the hyperfine qubit using a Raman transition (figure 4.1). The hyperfine qubit levels can be connected through a third auxiliary level, in our case this is the $P_{1/2}$ state of of ion, and two lasers that couple the two hyperfine levels to this excited state. Here ω_1 and ω_2 denote the frequencies of these two lasers and Δ is the detuning from the third level. If Δ is large compared to the single photon rabi frequencies then the 3 level Hamiltonian of this lambda system can be simplified to an effective two level Hamiltonian, involving only the two hyperfine levels of interest with a modified rabi frequency given by the product of the two single photon rabi frequencies, $\frac{\Omega_1^*\Omega_2}{4}$:

$$H_{eff} = \begin{bmatrix} \frac{|\Omega_1|^2}{4\Delta} & \frac{\Omega_1\Omega_2^2}{4} \\ \frac{\Omega_1^*\Omega_2}{4} & \frac{|\Omega_2|^2}{4\Delta} \end{bmatrix} \tag{4.1}$$

The diagonal terms come from the off-resonant coupling of the two lower energy levels to the excited state. They cause a change in the qubit frequency known as the AC-stark shift. The complex-valued off-diagonal terms couple the two qubit levels, causing rotations about some axis in the equatorial plane of the Bloch sphere, depending on the phase. This coupling allows us to take advantage of the benefits of optical transitions. In our case this transition is driven using 532 nm light which has a diffraction limited size of around 700 nm along the ion chain, given the NA of 0.37 in this direction. Since the ions are separated by 4 μm, this allows for the quantum state of one ion to be manipulated without affecting that of the others. Further, the smaller wavelength means that the momentum imparted from the photons to the atoms will be larger. In this case the shorter wavelength will yield a spin-motion coupling strength that is larger by a factor of $\sim 10^4$. Therefore, for a fixed geometric phase χ_{ij}, the intensity of the microwave needs to be increased by a factor of 10^4 relative to that required for the Raman transition.

To drive the Raman transition one could use two different CW laser sources but in that case one must lock the phase of the two lasers. Alternatively an EOM can be used to provide the ~ 10 GHz frequency splitting but EOMs tend to be lossy at these high frequencies [94]. The common choice, requiring only a single source, is to use a frequency comb generated by a mode-locked laser. One advantage of this method is that since interference only occurs when two pulses are temporally overlapped, perturbation of the beam profile at the ions due to back reflections from vacuum view-ports or other optics do not occur.

A mode-locked laser generates a series of short pulses of duration τ spaced $1/f_{rep}$ apart in time, where f_{rep} is the repetition rate. The Fourier transform of such a pulse train is a series of narrow comb teeth separated by the repetition rate. The envelope of the combs is given by the Fourier transform of a single pulse in the train and so the bandwidth is proportional to $1/\tau$. This is shown in figure 4.1 (b). In our experiments, we use a fiber laser from NKT with a pulse duration $\tau = 10$ ps, a repetition rate $f_{rep} = 104$ MHz and a frequency of 532 nm. Assuming the laser produces transform limited pulses, this corresponds to a spectral bandwidth (FWHM) for the frequency comb of $\sim 0.5/\tau = 50$ GHz. Thus, a frequency comb has more than enough bandwidth to address the hyperfine transition of most ions. It should be noted that this frequency domain picture of the interaction is only valid when the pulses are weak enough such that any single pulse has a negligible effect on the ion. In this case a large number of pulses are required to result in an interaction, hence the spectrum of the interacting field is a frequency comb.

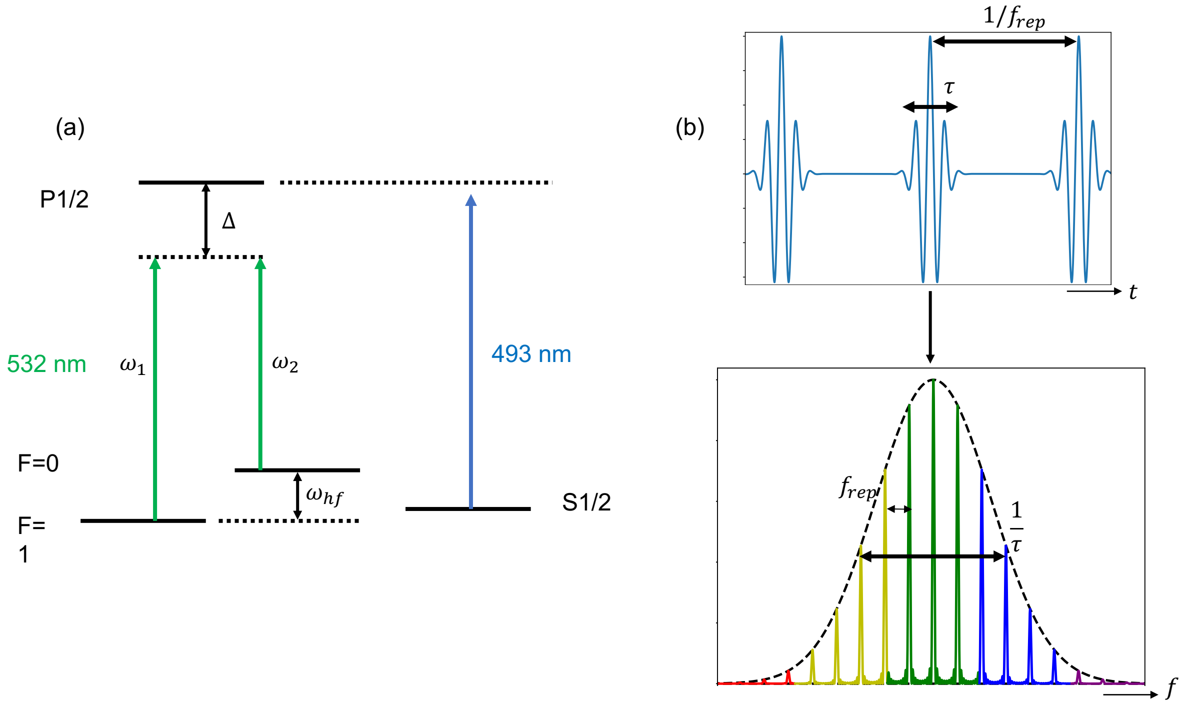

Figure 4.1: (a) Simplified Ba^+ level diagram depicting how a Raman transition can be performed. (b) Pulse train and it's Fourier transform. The bandwidth of the pulse in frequency domain is inversely proportional to the duration of a single pulse, τ in the train. The period of the pulse train is the inverse of the repetition rate f_{rep}. f_{rep} gives the distance between the comb teeth in frequency domain. The width of each tooth is inversely proportional to f_{rep}/N where N is the number of pulses in the pulse train.

To do the Raman transition with the pulse train, the laser is split into two paths, each of which is sent through an AOM and then combined at the ions. By shifting one comb with respect to the other using the AOMs, we can create a condition where the ith comb in the first beam and the N+ith comb in the second beam, satisfy the two-photon resonance: $Nf_{rep} + f_{AOM} = f_{hf}$, where f_{hf} is the hyperfine qubit splitting. This is depicted in figure 4.2.

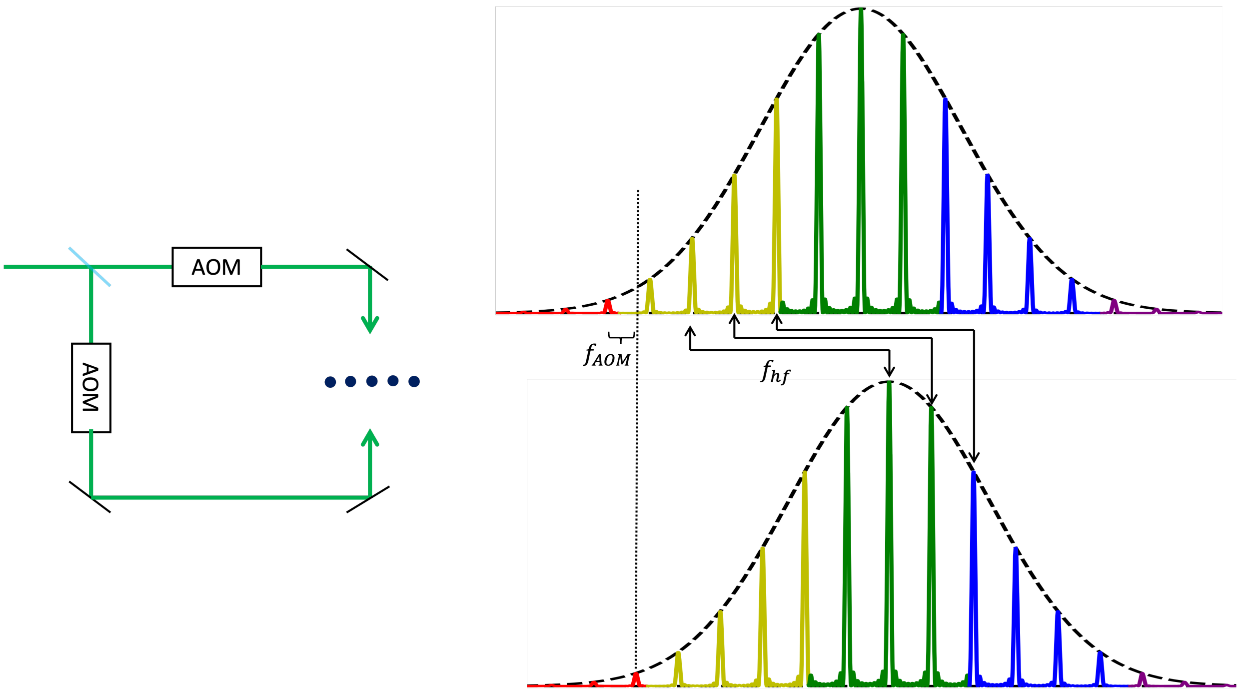

Figure 4.2: Raman transitions can be done by using a pair of detuned frequency combs generated by the same laser. By shifting one comb with respect to the other using a pair of AOMs, the beat note generated as the two beams interfere at the ions, can be made to satisfy the two-photon resonance. A typical comb has many more peaks than that depicted here. Our laser produces a 10 ps pulse train at a repetition rate of 104 MHz. This translates to around 480 comb teeth within the bandwidth of the light.

In this method of addressing ions, typically one of the beams illuminates the entire chain with approximately equal intensity, we call this the global Raman beam. The other path contains multiple tightly focused laser beams that are used to pick out specific ions in the chain for performing single and multi-qubit gates. It turns out that the two-photon rabi frequency for driving Raman transitions between the clock states is proportional to $\Omega \propto \sqrt{I_b \cdot I_r}\big(b_- r_- - b_+ r_+\big)$ [38]. Here $b_-, r_-, b_+, -r_+$ are used to denote the left and right circular polarization components of one of the two beams (denoted by b or r) involved in the Raman transition where for example, $\hat{\epsilon}_b = b_- \hat{\sigma}_- + b_0 \hat{\pi} + b_+ \hat{\sigma}_+$. This indicates that to maximize the Rabi rate, the two beams must have orthogonal polarization and there should be no $\hat{\pi}$ polarization component. Since the Raman beams run orthogonal to the chain, this is done by having the magnetic field run in the same direction. This corresponds to $b_- = r_- = b_+ = -r_+ = 1/\sqrt{2}$.

Individual addressing is necessary to turn a chain of ions into a universal quantum computer. Single qubit gates on specific ions, as given by equation 2.15, can be implemented by exclusively focusing an IA beam on the desired qubit. The repulsive Coulomb force between ions generates a long range interaction that can be used to connect the internal states of the ions through the shared modes of motion as described by the Hamiltonian in equation 2.16. To turn on this connection between only a specific pair of ions, only those ions must be perturbed by the laser interaction. In this way, as discussed in chapter 2, a two-qubit entangling gate can be implemented. This is pictorially depicted in figure 4.3 (a). Site specific optical addressing with control over the frequency and amplitude of each channel can be used to implement arbitrary spin Hamiltonians in any dimension. For example, figure 4.3 (b) shows how the all-to-all connectivity of the ions, along with individual addressing can be used to realize a system of interacting spins on a two-dimensional triangular lattice.

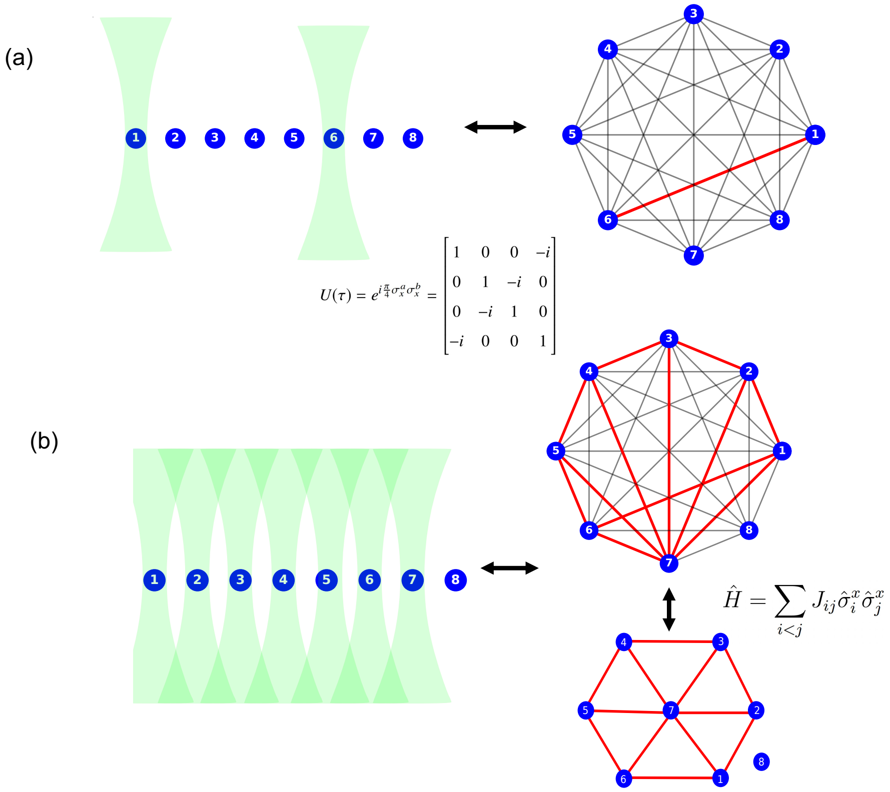

Figure 4.3: (a) By shining light on two specific ions in the chain, the Mølmer–Sørensen interaction can be used to implement a two-qubit unitary between those ions. (b) Control over the amplitude and frequency of each beam shining on the ions can be used to realize arbitrary spin models in any dimension. The graphs on the right show how a two-dimensional triangular lattice can be realized by turning on specific connections between the ions.

4.2 Review of techniques for site-resolved addressing of ions

There are currently three main schemes in use for the individual addressing of ions. These are summarized in figure 4.4. The first method, shown in figure 4.4 (a) uses a diffractive beam splitter to divide a single beam of light into multiple paths. Each of the diffraction orders are then mapped to one channel of a multi-channel AOM which provides independent control of the frequency, phase and amplitude of each beam. The light out of each channel is then focused down to the ion chain. This is a commercial device made by L3Harris [1], and has been successfully used in many experiments [37, 46, 144]. The multi-channel AOM consists of a single acousto-optic crystal and multiple piezo-electric transducers. As a result, when the radio frequency (RF) input is turned on for one channel, the transducer also perturbs the section of the crystal pertaining to the neighbouring channels. This causes unwanted light leakage from the neighbouring channels, thus perturbing the quantum state of the corresponding ions. The intensity crosstalk due to this effect has been measured to be on the order of 10^{-3} relative to the peak intensity on the target ion [46].

Another method, shown in figure 4.4 (b) uses one or a pair of acousto-optic deflectors (AOD) for individual addressing. The angle of deflection of an acousto-optic device is proportional to the frequency of the RF drive. So by modifying the RF input frequency, a beam can be made to scan across the entire ion chain. By using an input RF signal with multiple frequency tones, the AOD will create multiple deflected beams, each corresponding to one RF frequency. This allows for parallel control over the ion chain. The problem with using a single AOD is that it provides no control over the exact frequency of each laser beam as this is fixed by the required bending angle of the beam. This problem can be addressed by adding a second AOD orthogonal to the first. If f_0 is the center frequency of the AOD and a frequency shift f_i is added to the first device, by subtracting f_i from the second AOD, the shift in the laser beam's frequency be canceled. With this configuration, as f_i is varied, the device scans a line at 45 degrees to the axes of the AODs. Hence to scan across a chain of ions, the AODs need to be oriented at 45 degrees relative to the trap axes. The state of the art intensity crosstalk achieved using this method is less than 10^{-4}, an order of magnitude lower than the multi-channel AOMs [108]. There are two problems with this paired AOD scheme however. One is that the intensity on each channel drops quadratically with the number of added tones [108]. Further, the device only provides control over the exact frequency of the input light and not that of the individual channels.

The third method, shown in figure 4.4 (c), uses a digital micromirror device (DMD) for holographic beam shaping. A DMD consists of a two dimensional grid of small mirrors, each with a size on the order of 10 μm [5]. The binary position of the mirrors are controlled by a FPGA, allowing the local amplitude of light to be turned on or off depending on the deflection angle of the corresponding mirror. For a given desired beam profile at the ions, at the focus of a lens, the DMD can be used to generate an arbitrary hologram that modifies the wavefront of an incoming laser beam such that this desired beam profile is attained. This great level of control over the shape of the wavefront of an incident beam can be used to characterize and then compensate for aberrations in the optical system, allowing for nearly diffraction limited performance. With this technique, DMDs have been used to address ions with a relative intensity crosstalk on the order of 10^{-4} [122]. While the DMD allows one to realize arbitrary intensity profiles at the ions, which is important for long chains with significant non-uniformity in the ion pitch, the device is slow, with a typical frame rate of 10 kHz [121]. On the other hand, the rise and fall time of AOMs can be as short as several nanoseconds. So while the profile generated by an AOM based system is fixed, these devices can be used to modulate the amplitude of the light on each channel at a far faster rate. The current frame rate makes mid-circuit modification of the intensity profile at the ions, say for the purpose of performing two-qubit gates between arbitrary ion pairs, slow. Given that typical two-qubit entangling gates take on the order of 100 μs to execute, this frame rate is a bottleneck on the gate times. Further, just as with the AOD scheme described above, the current DMD implementations also only provide control over the frequency of the incident beam and not that of each individual channel being focused onto the ions. Such wavefront shaping techniques can also be done using nematic liquid crystal arrays but this technology has an even lower frame rate than the DMD [121, 135].

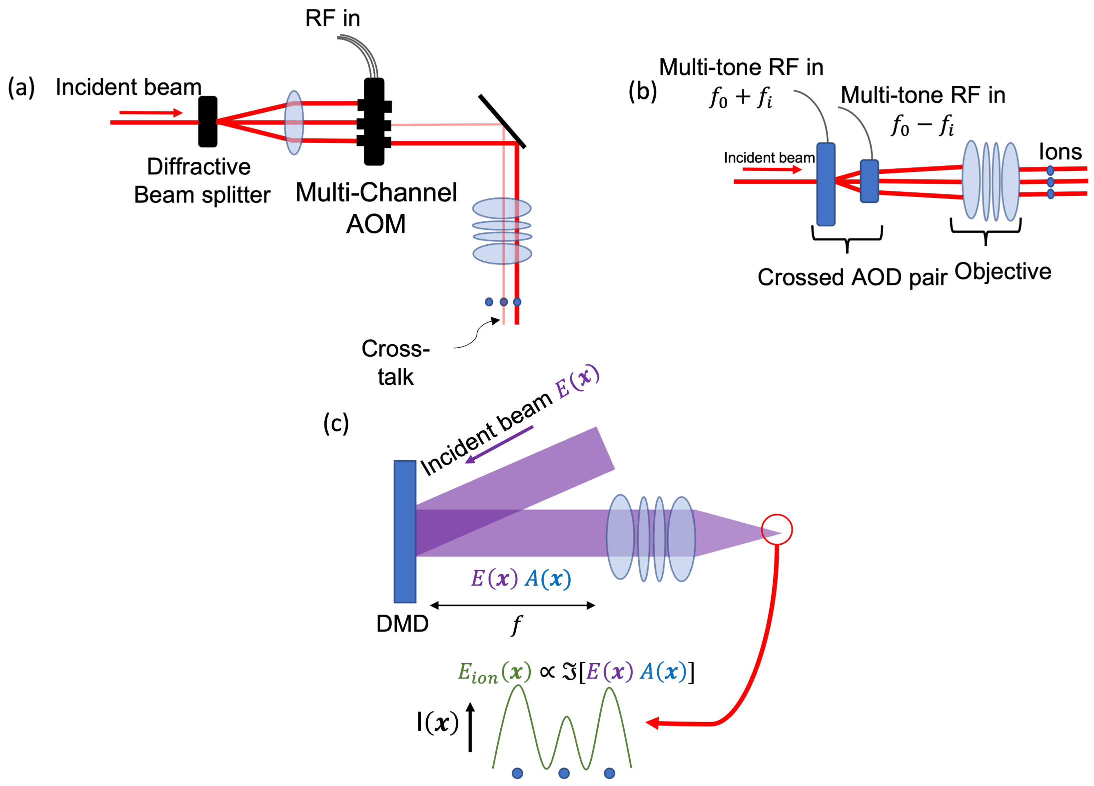

Figure 4.4: Previous implementations of individual addressing discussed in [46, 37, 108, 71, 122].

4.3 Raman System Overview

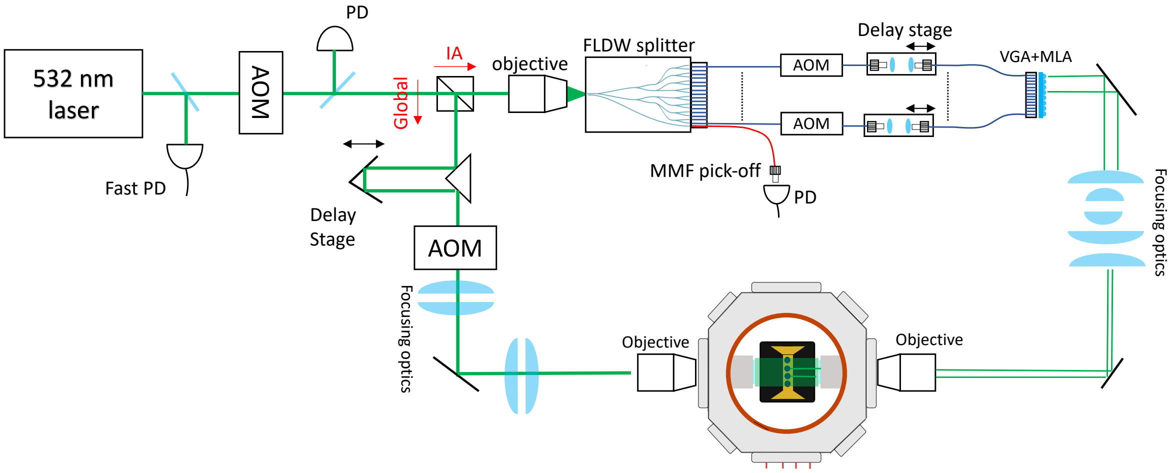

Figure 4.5: Simplified schematic of our optical setup for using Raman transitions for site-specific coherent qubit manipulation.

The experimental setup used for Raman gates, based on frequency combs, is shown in figure 4.5. In our experiments, we used a mode-locked fiber laser from NKT photonics, generating 10 ps pulses at a repetition rate of around 104 MHz and a center wavelength of 532 nm. Part of the light out of the laser is sent to a fast photodiode, with a bandwidth $>$ 10 GHz, from Alphalas (UPD-35-UVIR-P). The photodiode is used to detect the beat-note between the comb-teeth generated by the frequency comb. This signal can be used to measure drifts in the beat-note which can then be compensated for by feeding the error signal back on the AOM in the global beam path. The zeroth order output of the first AOM shown in figure 4.5 is used in conjunction with the photodiode just after the AOM (MHz bandwidth) to compensate for and reduce intensity noise in the laser output. Next, the beam is split into the global and individual addressing channels using a polarizing beam splitter. In the global path, a knife-edge right-angle prism mirror (Thorlabs MRAK25-P01), along with a retroreflector mounted on a moving stage is used to adjust the length of the global beam path to ensure that pulses from the global and individual addressing paths arrive simultaneously at the ions. Temporal (and of course spatial) overlap between pulses from each path is necessary to maximize the resulting rabi frequency. The translation stage (Newport 9066-X-P) has a travel range of 12.7 mm and a resolution of < 30 nm. Given that the pulses are 10 ps wide, the 30 nm step size provided by the stage corresponds to a timing resolution that is $\sim 10^5$ times smaller than the duration of the pulse; this is more than enough to precisely overlap the two pulses and maximize the rabi frequency. Next in the global path, the light passes through an AOM used for frequency and amplitude modulation, the former being required for beat-note stabilization. Finally, a set of cylindrical beam shaping optics are used to reshape the beam so that the profile of the focus at the ions extends the entire chain while clearing the trap in the orthogonal direction. The final microscope objective used for both paths is a custom component from Special-Optics with an effective focal length of 57.6 mm, working distance of 44.277 mm (36.277 mm Vacuum + 5 mm glass + 3mm air) and NA of 0.4. The objectives were designed to accommodate both 493 nm and 532 nm, allowing us to potentially use the individual addressing path for site-selective measurement.

Now we will describe the individual addressing path. An objective lens is used to mode-match the light from the laser to the input of a femtosecond laser direct write (FLDW) waveguide, a device that splits the light into 17 channels. A V-groove array (VGA), consisting of 17 fibers is aligned to the 17 outputs of the waveguide and epoxied in place. 16 of these channels are made up of single mode fibers that deliver light to the ions while the final channel is a multi-mode fiber (MMF) that is used to monitor the overall coupling into the waveguide for the purpose of automatic alignment optimization. The 16 channels are each connected to a fiber coupled AOM (Fiber-Q from Gooch Housego) that is used to provide independent control over the frequency, phase and amplitude of each beam. Next, a set of fiber coupled delay lines are used to ensure that the pulses from the 16 channels arrive simultaneously at the ions. This is needed because of the non-negligible tolerance on the length of each fiber. The delay lines we use are the ODL-700 from Oz-optics, which have a travel range of 4 mm and a resolution 0.67 ps per turn of the adjustment screw. Light from the 16 channels is then coupled back into free-space using a set of fibers whose facets are spaced 250 μm apart from each other by another VGA. A telecentric imaging system with a 60x magnification then maps this 250 μm pitch of the beams to the 4 μm pitch of the ions. A microlens array (MLA) is placed in front of the VGA to allow the beam waist of each channel to be controlled independently of the pitch between the beams. This independent control allows for a tight focus, ~ 1 μ m, to be realized at the ions. In the following, each element of the Raman individual addressing system will be discussed in more detail.

4.3.1 The Global beam telescope

A schematic of the beam shaping optics for the global Raman path, along with the resulting beam profile at the ions is shown in figure 4.6. It consists of a set of 4 cylindrical lenses, two of these lenses expand the beam orthogonal to the chain (25 mm and 125 mm), and the other two shrink the beam along chain (300 mm and 25 mm). The microscope objective then focuses this elliptical beam down to the ions. Since the beam radius after a lens is inversely proportional to the size of a collimated beam just before it, the resulting profile at the ions will be tightly focused orthogonal to the chain while extending across the entire chain. Based on the measured beam profile, shown in figure 4.6 (b), we measure a radius of 290 μm along the chain and 6 μm orthogonal to it.

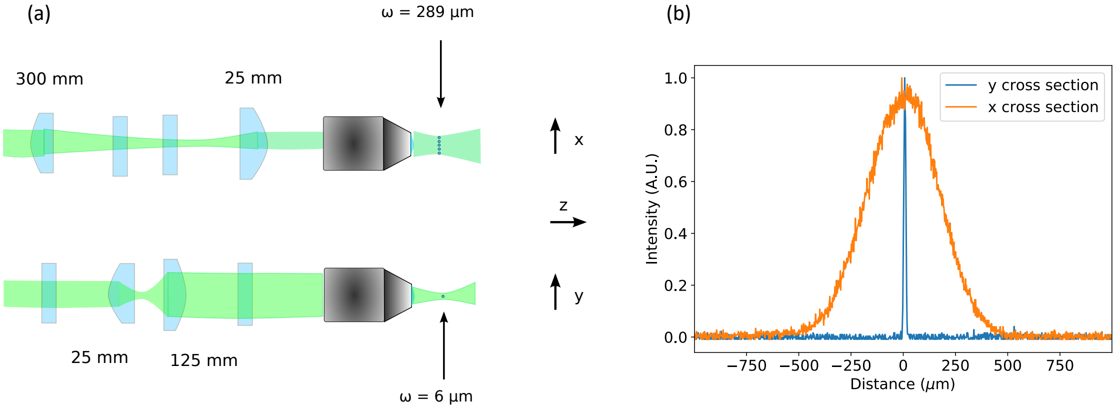

Figure 4.6: (a) Schematic of the global Raman beam path focusing optics. (b) The resulting beam profile at the position of the ions.

4.3.2 FLDW Waveguide Splitter

The FLDW chip consists of a series of waveguides, written into glass that are used to split the light into multiple channels. By bringing two waveguides close together, the evanescent field from the waveguide initially carrying the optical power couples some light to the other waveguide. The power splitting between the two is determined by how far apart they are and how long they travel together before moving apart [137]. In the splitter chip, these evanescent splitters are cascaded together and divide the input light into 16 different channels at the output.

These waveguides are created by using a high power, tightly focused femtosecond laser to locally heat up the piece of glass onto which the waveguide is being written. This locally changes the bonding structure of the underlying material which results in an increase to the refractive index [34]. The change in the refractive index compared to the surrounding takes the form of a gaussian: $n(r) = n_0 + \Delta n e^{-2r^2/a^2}$, where n_0 is the index of the surrounding glass and a is the core radius of the waveguide. The typical index contrast, $\Delta n \sim 10^{-3}$ is small compared to other technologies such as step-index fibers or SiN waveguides.

However, the fact that a laser beam is used to create the waveguide means that this technique can be used to create relatively complex waveguide shapes, such as the one for our evanescent splitter chip shown in figure 4.7. The output of the power tap port is connected to the multi-mode fiber discussed earlier. The terminated marker is used as a visual reference during alignment of light into the waveguide. Once scattered light from this line marker is detected, we know that the device is at the correct height since the main waveguide device and this marker are at the same height. At this point, by horizontally translating the chip, light can be coupled into the device. The input waveguide of the main device is recessed into the piece of glass by roughly 200 μm. Since we need to send ~ 2 W (average power) of light into the device to get a few milliwatts out of each channel, focusing the light to a few microns, on the order of the mode-field diameter of the input waveguide, will damage the face of the glass due to the presence of dust and other contaminants, severely lower the coupling efficiency. By placing the focus inside the piece of glass, this is avoided. This input waveguide has a mode field diameter (MFD) of 4.5 μm in the horizontal and 5.1 μm in the vertical direction. An objective with a 20 mm EFL, working distance of 15 mm and NA of 0.25 (Thorlabs LMH-10X-532) is used to couple light into the input waveguide. The 16 single mode channels at the output of the device have a MFD of 4.5 ± 0.1 μm at 532 nm while the single mode fibers that guide the light from each channel after the device have a MFD of 3.4 ± 0.5 μm. The maximum coupling efficiency given this mismatch can be quantified using the overlap integral [4]:

$$\eta = \frac{|\int U_1(x,y)U_2(x,y)dxdy|^2}{\int |U_1(x,y)|^2 dxdy \int |U_2(x,y)|^2 dxdy} \tag{4.2}$$

Assuming gaussian mode profiles e^{-r^2/MFD_i^2} this yields $\eta = (2 * \frac{MFD_1 \cdot MFD_2}{MFD_1^2 + MFD_2^2})^2$. From this, the MFD mismatch results in an insertion loss of 0.3 dB. This is not the only source of loss in the system; these will be elaborated on later.

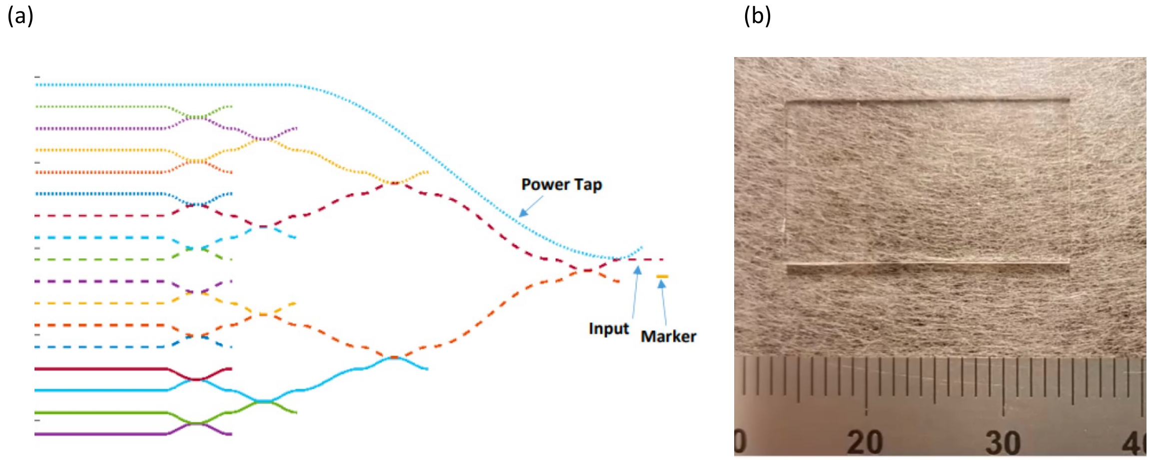

Figure 4.7: (a) Schematic of the waveguide splitter chip [35]. Light is coupled on the right side into the waveguide, divided into 17 channels using a series of cascaded evanescent splitters and exits the waveguide on the left. (b) Image of the actual device used in the experiments. The piece of glass is around 2 cm in length. The device was designed by Dr. Matthew L. Day and manufactured by OptoFab at Macquarie University.

Ideally, all 17 channels coming out of the waveguide should possess equal optical powers. In reality this is not the case and we observe a relatively large variation in the splitting ratios between channels. The output power as a function of channel number is shown in figure 4.8 (a). There is roughly a factor of 5 difference in the optical power out of the best performing channel (6) and the worst performing channel (16). To obtain an equal Rabi frequency for each ion, the powers on each channel must be made equal. This is done by controlling the RF power going to each of the fiber coupled AOMs. To protect the waveguide and the waveguide-VGA bond, a case was designed to store the waveguide. This is shown in figure 4.8 (b). The device is placed on a 3-axis linear translation stage with Piezo linear actuators for precise positioning. Expecting temperature drifts due to scattered laser light to have an important influence on the splitting ratios, through the temperature dependence of the refractive index, active temperature control was built into the case. This consists of a thermoelectric cooler (CP60433H) and heat sink, and a temperature sensor (TMP37FT9Z). A PID controller is then used for the temperature stabilization. The effect of the splitting ratio on temperature is shown in figure 4.8 (a). Varying the temperature from 20-26 °C, well beyond the expected change in the temperature of the device, we observe a relatively small change in the splitting ratio (at most $\sim 4\%/^{\circ}$C).

By deliberately misaligning the coupling into the waveguide, it was found that the power in the MMF channel is not necessarily directly proportional to the power in the other channels. Perfect alignment corresponds to the case where the power out of the single mode channels is maximized. Misaligning the system from this point, it was found that the power in the MMF channel can sometimes increase while the power in all other channels decreases. Therefore, the MMF channel does not give an accurate measure of the quality of the coupling to the waveguide and cannot be used for the purpose of automatic alignment; instead, one of the single mode channels can be used.

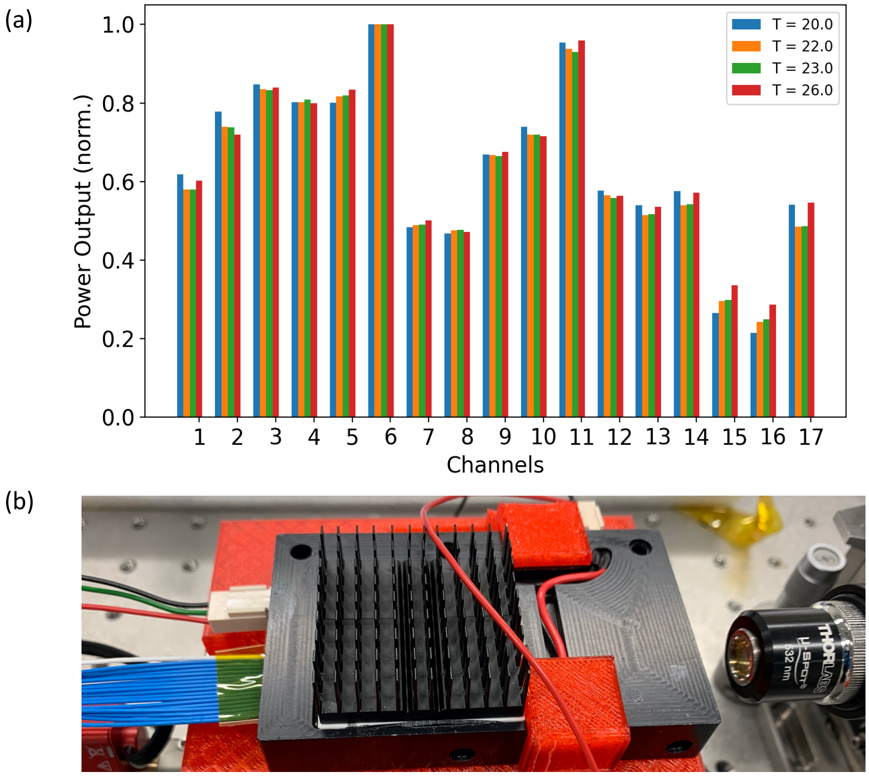

Figure 4.8: (a) Power out of each channel of the splitter chip for a range of temperatures. (b) Waveguide splitter chip inside a temperature-controlled case. On the right a microscope objective focuses light into the input waveguide mode and on the left the 17 fibers exit the case. The blue jacketed fibers are the 16 single mode fibers (PM460-HP) and the single white fiber at the end is the multi-mode fiber. The case is placed on a 3-axis linear translation stage with piezo motor control for alignment.

4.3.3 IA telescope

A schematic of the telescope used in the individual addressing path is shown in figure 4.9. This telescope has a demagnification of 62.5x and is used to map the 250 μm pitch of the fibers from the VGA to the 4 μm pitch of the ions. To achieve this, the telescope uses two cascaded 4f systems. The first, consisting of a 300 mm and 25 mm lens, provides a magnification of 1/12x. The second consists of a 300 mm lens and the 57.6 mm EFL objective from special optics, yielding a magnification of 0.19x. Together, the entire system provides a demagnification of 62.5x. In between the two lenses of the first 4f system, there are two cylindrical lenses (100 mm and -25 mm) that are used to shrink the size of the beam orthogonal to the ion chain. This is used to reduce the NA of the beam after the objective as in this direction, the maximum NA is only 0.12 due to the geometry of the trap.

The use of two cascaded 4f systems makes the telescope telecentric. An optical system is (doubly) telecentric if the chief ray is parallel to the optic axis in object and image space. The focusing optics for the IA system need to be telecentric to ensure that for one, the magnification is independent of the object location, in this case the beam focus after the MLA. Telecentricity is also necessary to ensure that the wave vectors of all the individual addressing beams are approximately parallel to each other and orthogonal to the chain, ensuring maximum coupling to the radial normal modes of interest and minimizing crosstalk to the other normal modes.

This telescope uses achromatic doublets to accommodate both 532 nm light for Raman qubit manipulation as well as 493 nm light for site-resolved qubit measurement. Based on the Zemax simulations of the telescope, we found the axial color, including the MLA, to be around 4 μm between 532 and 493 nm [137]. Given that the focused spot is around 0.9 μm at 532 nm, the Rayleigh range is around 4.8 μm. Therefore the chromatic shift is just within the Rayleigh range and causes the beam radius to slightly increase to 1.2 μm.

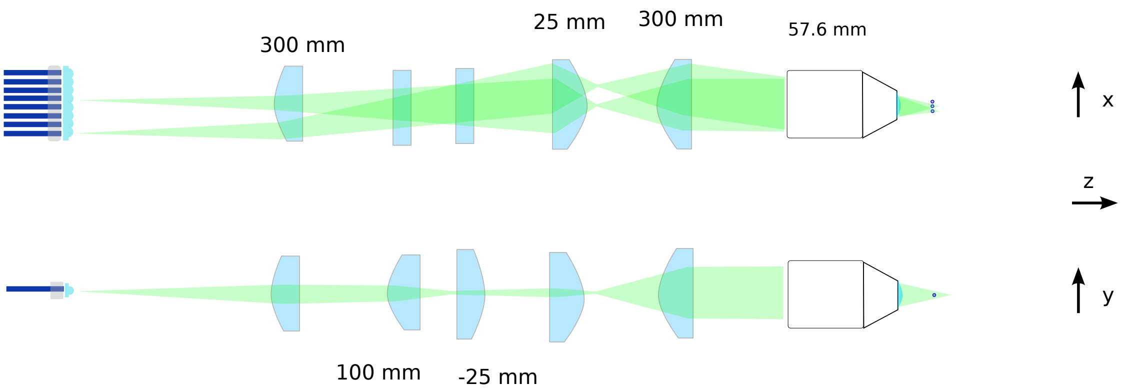

Figure 4.9: The individual addressing path telecentric imaging system. This is used to map the beam foci after the MLA, separated by 250 μm, to the 4 μm separation at the ions.

4.3.4 The micro lens array

The pitch between the ions is fixed at 4 μm and the maximum available NA in the final image space is constrained to 0.37 by the geometry of the vacuum chamber, re-entrants and the trap. To understand the necessity of the MLA, we can look at the Lagrange invariant, H, a conserved quantity at any location z in a paraxial optical system:

$$H \equiv ny\bar{\theta} - n\bar{y}\theta \tag{4.3}$$

where n is the refractive index, y and $\bar{y}$ are the heights of the marginal and chief rays respectively and θ and $\bar{\theta}$ are the angles these rays make with the optical axis. At conjugate planes, which is what interests us in this discussion, the expression simplifies to $\bar{y}_o\theta_o = \bar{y}_i\theta_i$ where the subscripts denote the values of the ray parameters in object (o) and image (i) space. In words, the product of the height of the chief ray and the NA of an optical system, at conjugate planes is conserved. Given that the fiber cores in object space are separated by 250 μm and the fiber NA is 0.1, the invariant is violated and an optical system, satisfying the constraints we have on the beam in image space ($\bar{y}_i$= 4μm and θ_i=0.37), cannot be constructed. To satisfy the constraints, either the pitch of the fibers or their NAs need to be reduced. This problem is depicted in figure 4.10 (a). It should be noted that while outside of the linear, paraxial regime this invariant is not satisfied in general, to design an optical system that is nearly aberration free, this invariant must be taken into account.

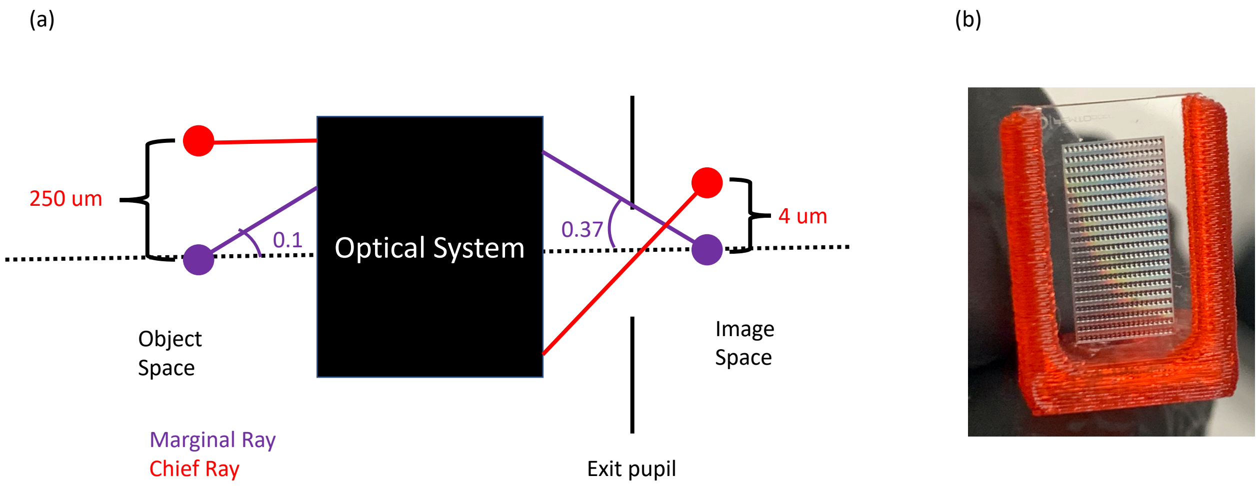

Figure 4.10: (a) Schematic of the chief (red) and marginal (purple) rays in object and image space. The optical invariant requires the product of these two quantities at conjugate planes to be conserved but this cannot be done using bulk optical elements. The pitch of the fiber array is 250 μm and the NA of each fiber is 0.1. In image space, the maximum available NA is 0.37 and the pitch between the ions is 4 μm. To satisfy the constraints we have on the beam in image space, we reduce the NA of the beams out of the fibers by using a series of microlenses placed at the facet of the fibers. (b) Image of the MLAs used in our IA setup. In the experiment, only a single row is used. Multiple rows were manufactured to account for fabrication inaccuracies.

To satisfy the constraints we have on the beam in image space, either the pitch of the fiber array or the NAs of the beams from each channel need to be reduced. We initially considered the former scheme where the output of the splitter chip is connected to another FLDW waveguide that reduces the pitch between the fibers to around 15 μm. This is shown in figure 4.11. This solution was abandoned because numerical simulations indicated significant crosstalk between the 16 channels after pitch reduction [137]. The intolerable level of crosstalk ($> 10^{-4}$ in intensity) was caused by the limited index contrast available in current laser written waveguide technology ($\sim 10^{-3}$ as discussed previously). The crosstalk can be reduced by using waveguides with higher index contrast, thereby decreasing the penetration depth of the evanescent field.

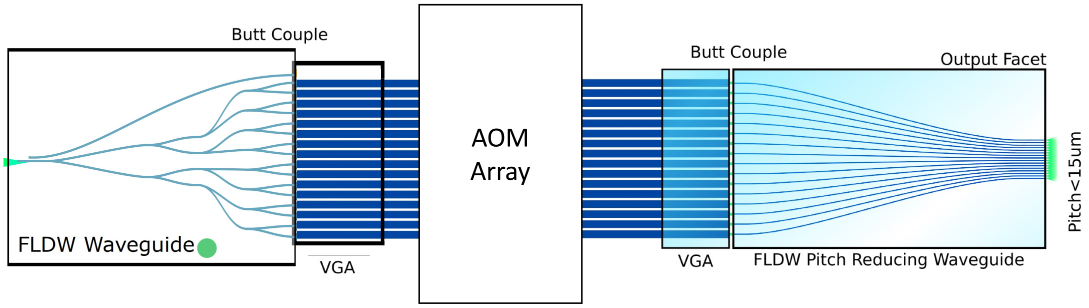

Figure 4.11: The optical invariant can be satisfied by using a FLDW pitch reduction waveguide. The low index contrast of laser written waveguides yields significant crosstalk at the required waveguide pitch so this solution was abandoned. Figure adapted from [137].

Rather than exploring this idea we switched to the second solution, that of reducing the NA of each channel in object space. This can be done using an array of small lenses placed at the facet of each fiber. This microlens array expands the waist size out of each fiber thereby reducing the divergence or NA of each channel. With this scheme, crosstalk due to evanescent coupling is no longer an issue and it is only limited by the intensity crosstalk at the location of the ions.

The MLAs were designed by master's student Nikolay Videnov and manufactured by Femtoprint. Femtoprint uses ultrafast lasers to locally modify the index and density of a piece of glass. This combined with chemical etching can be used to realize complex three-dimensional structures in glass, such as our microlenses. The initial set of micro lenses purchased from the company possessed a shorter focal length than what we had designed for, possibly due to the polishing step that follows the etch [137]. To account for these fabrication inaccuracies, we instead designed a grid of microlenses with a range of effective focal lengths starting from 0.525 mm and going up to 1 mm in steps of 0.025 mm for a total of 20 arrays. This is shown in figure 4.10 (b). To determine whether an array in this new batch of MLAs has the desired effective focal length, an optical profilometer was used to measure the surface profile of one lens from each array. The profilometer is made up of a Michelson interferometer with a white light source. With the sample on one arm of the interferometer, the height of each point on the sample can be measured based on the stage position yielding the highest intensity on a camera pixel corresponding to that point. 1D cross sections of the surface profile for one lens from each array is shown in figure 4.12. The microlenses were designed to be aspheric to lower the contribution of spherical aberrations to the system. Specifically, the surface sag for an even asphere was used in the design which Zemax defines to be:

$$z(r) = \frac{c \cdot r^2}{1 + \sqrt{1 - (1+k)c^2 r^2}} + \sum_{i=1}^{N} \alpha_{2i} r^{2i} \tag{4.4}$$

where c is curvature of the surface, k is the conic constant, r is the radial coordinate and the α_i's are aspheric coefficients. An even aspheric only contains the even powers of r. The designed lenses only have the 2nd, 4th and 6th order aspheric coefficients and these coefficients are the same for all the lenses, optimized in Zemax to reduce spherical aberrations. Similarly k ≈ -1.002 (approximately a parabolic surface) is the same for all the lenses. The only parameter that is changed to modify the effective focal length between the different arrays is the curvature c. By fitting this equation to the measured surface profiles, the curvature and so the effective focal length of each array can be determined. This data is shown in table 4.1. Comparing this to the ideal profiles from Zemax, figure 4.12 (c) shows the error in the radii of curvature of the manufactured lenses. It is evident that the fabricated lenses have a shorter radius of curvature and thus a shorter effective focal length. On average these lenses have an EFL that is about 2% shorter than the design. Despite this discrepancy, by manufacturing lens arrays with several different EFLs, we were able to identify a row that has almost exactly the properties we were looking for. This is lens 3 in the table.

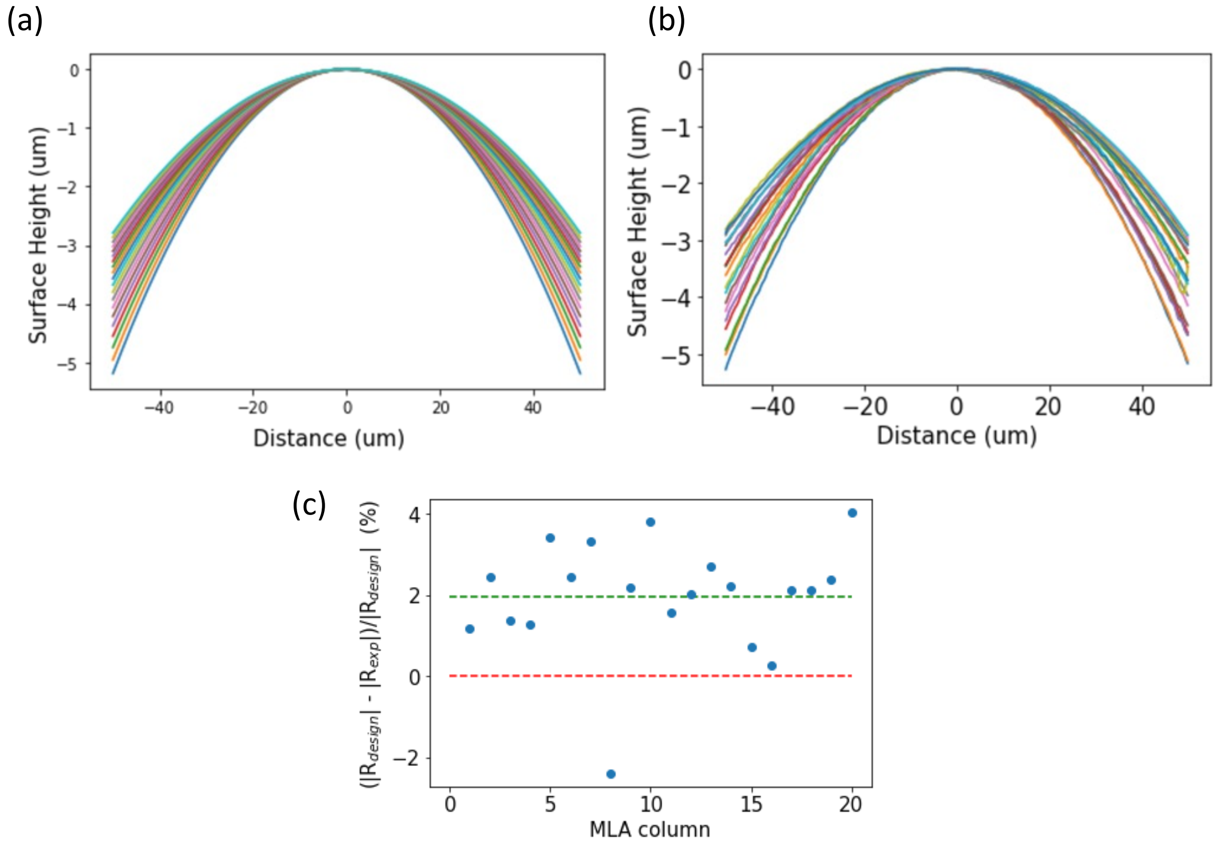

Figure 4.12: (a) Theoretical/design surface profiles obtained from Zemax using equation 4.4. (b) Actual surface profiles of the manufactured lenses as measured by an optical profilometer. (c) Normalized difference between the radii of curvature of the designed and manufactured lenses. The manufactured lenses have a radii of curvature that is on average 2% shorter than the design, as indicated by the green line.

MLA	Design Curvature (mm)	Manufactured lens Curvature (mm)	EFL (mm)
1	-0.15422	-0.1524	0.5156
2	-0.15877	-0.1549	0.5289
3	-0.1631	-0.1609	0.5621
4	-0.1673	-0.1652	0.5867
5	-0.1714	-0.1655	0.5885
6	-0.1753	-0.1710	0.6209
7	-0.1790	-0.1731	0.6336
8	-0.1826	-0.1870	0.7249
9	-0.1861	-0.1820	0.6910
10	-0.1894	-0.1822	0.6925
11	-0.1927	-0.1896	0.7432
12	-0.1958	-0.1919	0.7592
13	-0.1989	-0.1935	0.7708
14	-0.2018	-0.1973	0.7995
15	-0.2047	-0.2033	0.8456
16	-0.2076	-0.2070	0.8760
17	-0.2104	-0.2059	0.8669
18	-0.2132	-0.2087	0.8898
19	-0.2160	-0.2109	0.9085
20	-0.2189	-0.2100	0.9015

Table 4.1: Radii of curvature of the design and manufactured lenses, along with the effective focal lengths of the fabricated lenses.

4.3.5 Crosstalk Characterization

Once a viable lens array was identified and the paraxial properties of the IA telescope were verified, the IA beam path was built up for characterizing the intensity crosstalk. According to our Zemax simulations [137], we should be able to attain a relative intensity at the position of a neighbouring ion that is $< 10^{-5}$ of the peak, positioned at the target ion. This simulation data is shown in figure 4.13 (c). In practice, the ideal profile is hard if not impossible to attain due to the difficulty of aligning the MLA to the VGA.

In our test setup, alignment is done by placing the VGA on a manual 3 axis stage and using a beam back-propagating through the telescope to precisely position it relative to the telescope. Next, the MLA, mounted on a 6-axis stage, is brought close to the VGA. The pitch and yaw are adjusted by looking at the MLA-VGA interface using an over-head camera and the roll is adjusted by letting through the beam at the center and two extremes of the VGA, viewing the beams on a camera, and adjusting this axis until all three beams are at the same height.

To characterize the intensity crosstalk between channels, the beams after the MLA are imaged using a single 250 mm focal length lens, providing a 0.5x magnification, onto a camera. As with the CW telescopes of the previous chapter, several profiles at multiple exposures were recorded and stitched together, to obtain a single profile with sufficient dynamic range to assess the crosstalk level between the neighbouring channels. Of-course, as discussed in chapter 3, the crosstalk is ideally characterized by using the ion as the sensor but at the time of performing these measurements we did not have access to ions. This crosstalk data is shown in figure 4.13 (a). The profiles near the left end of the the system are broadened compared to the rest of the channels and as a result exhibit a larger amount of intensity crosstalk. For these channels, the crosstalk is on the order of 10^{-3}. For the rest, it is on the order of 10^{-4}. This asymmetry is most likely caused by the imperfect alignment of the MLA to all channels of the VGA. Since the rabi rate is proportional to the square root of the intensity, this intensity crosstalk data can be translated into an error on the rabi frequency. That is, the rabi rate of an ion when the light on its neighbours are turned on. This error is shown in figure 4.13 (b). This data was obtained assuming that both nearest neighbours of a given channel are turned on to the same intensity. From the figure it is evident that this error for most channels is on the order of 1%. This level of crosstalk is comparable if not better than that obtained with the technologies outlined previously. At the same time, our individual addressing system provides rapid, simultaneous control over the frequency, phase and amplitude of each beam using fiber coupled AOMs, while avoiding the crosstalk that results from having a single crystal for all channels.

To verify these results, the crosstalk measurement was repeated for one channel after the full IA imaging system (62.5x demagnification). To capture the beam profile at the ion plane, a camera with a relatively small pixel size is required, given that the expected beam radius at the focus of the objective is around 0.9 μm. For this we use the Raspberry Pi Noir V2 camera. It is a color camera with each unit cell consisting of 2 green pixels, one red pixel and one blue pixel. The size of each unit cell is 1.12 μm, thus the resolution is too low relative to the beam radius to obtain a precise beam profile. Nevertheless, the measured intensity crosstalk level should be comparable to that obtained in the prior measurement. This profile is shown in figure 4.13 (d). Our measurements indicate an intensity crosstalk slightly greater than 10^{-4}, 4 μm away from the peak, at the location of the neighbouring ions. This is commensurate with the data shown in figure 4.13 (b).

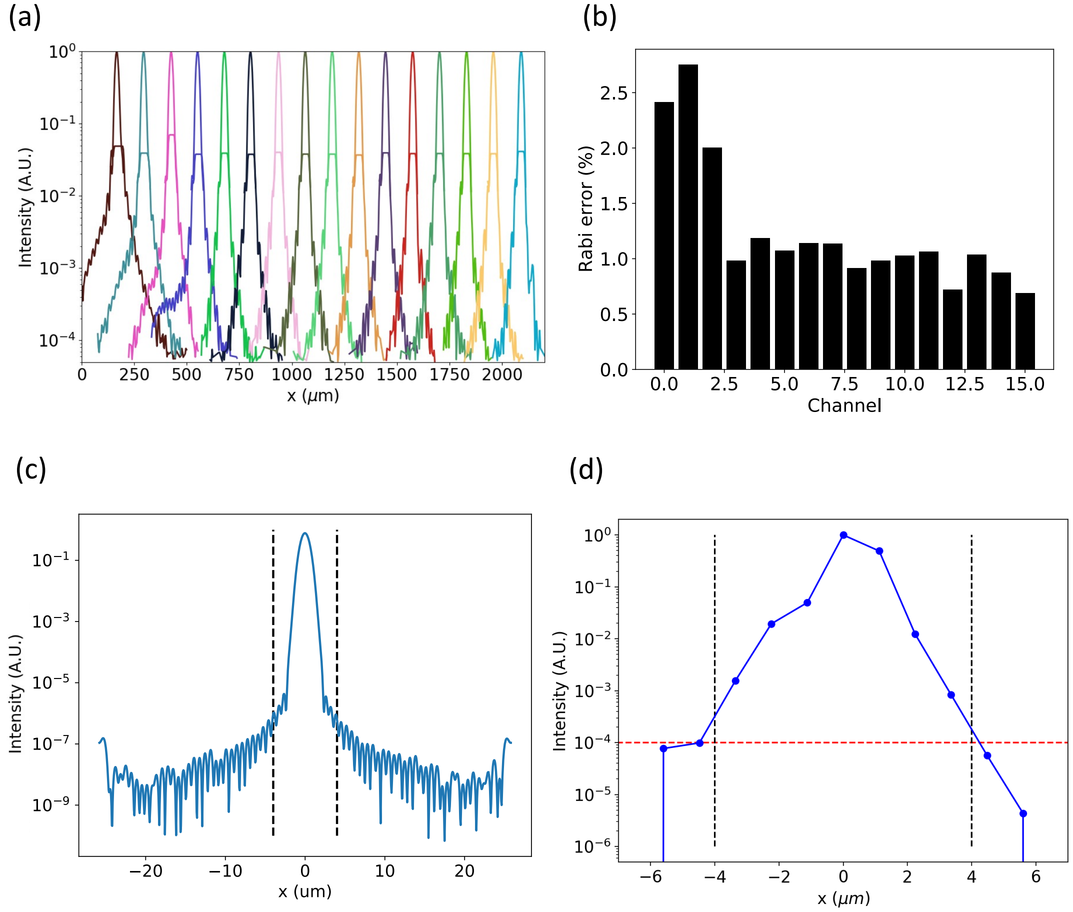

Figure 4.13: (a) Beam profiles measured after the MLA by imaging the beams with a single 250 mm focal length lens, providing a magnification of 0.5x, onto a camera. (b) Relative rabi rate of an unaddressed channel when the light on its nearest-neighbours are turned on. Due to the non-zero intensity at the location of the unaddressed ion, this ion also undergoes a slight Rabi rotation. An error of 1% corresponds to a rotation angle that is 100 times smaller compared to the addressed ions. (c) Simulated profile of one of the IA beams at the position of the ions, after the IA telecentric imaging system (62.5x demagnification). This was obtained using physical optics propagation in Zemax. (c) Actual beam profile at the location of the ions, measured using a camera with ~ 1 μm $\times$ 1 μm pixels. The red horizontal line denotes where the intensity is at 10^{-4} of the peak and the black vertical bars denote positions that are 4 μm away from the peak.

4.3.6 System insertion loss

Knowledge of the power reaching the ions is of utmost importance as it sets an upper bound on the possible rabi rate. Fiber coupled components in theory are plug and play black boxes that one can easily add or remove from an optical system. In practice this convenience is hampered by larger than expected insertion losses once the component arrives from the manufacturer. Insertion losses for major components of the IA system are shown in figure 4.14 (a). The input power is further attenuated at the AOMs by the requirement that all channels must have equal optical powers. To attain a rabi rate of at least 1 MHz, we need the optical power to be around 1.5 mW on the individual addressing side. The red curve in figure 4.14 (b) shows how the power per channel increases as the number of included channels are reduced, where each time we remove the worst performing channel in the set of 16. The power per channel increases each time a channel is removed since the AOMs must compensate for a smaller variation in the powers out of each channel. From this curve it is evident that to attain our desired 1 MHz rabi rate, we must remove the two worst performing channels (Channels 15 and 16). With this omission we can extract more than 1.5 mW from each channel. The black curve of figure 4.14 on the other hand shows how the total insertion loss scales with the number of channels included. When all channels are included, the power reduction imposed by the requirement of having equal powers on all channels increases the total loss. If too many channels are removed on the other hand, then the total insertion loss increases as well. In our case an optimal value of -19 dB is reached when the worst performing channels, 15 and 16, are removed. The power data plotted in figure 4.14 is based on an input power of 2 W into the evanescent splitter chip.

(a)

Element	Insertion loss (dB)
Waveguide	5
Waveguide-VGA bond + fibers	4.9
AOMs	3.8
Variable Delay lines	1.9 (Max delay), 4.6 (Min delay)

(b)

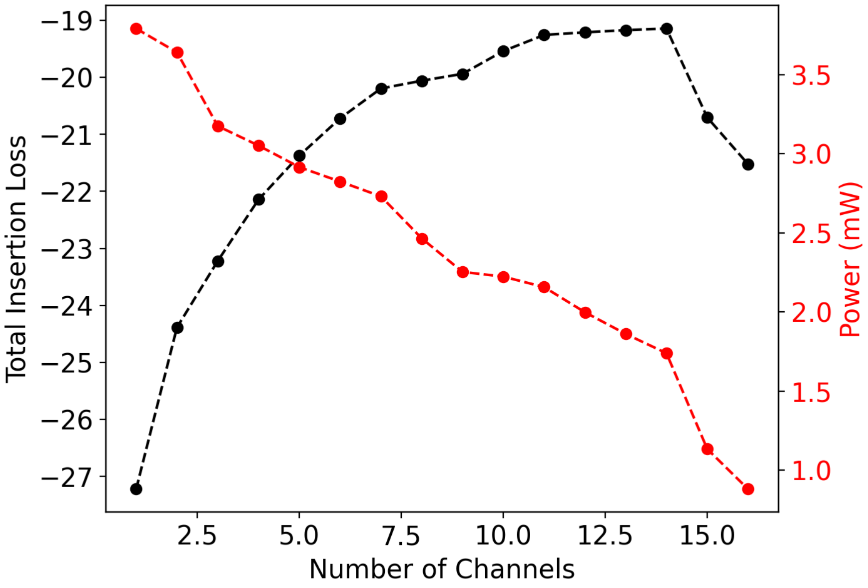

Figure 4.14: (a) Insertion loss for the major components of the individual addressing system. (b) The power per channel (red) and the total insertion loss (black) as a function of the number of channels included in the IA system. The channels are placed in increasing order from best performing (highest output power) to worst performing (lowest output power). As channels are removed, the power per channel increases since the AOMs must compensate for a smaller variation in the optical power.

4.3.7 Pulse Arrival times

In order to obtain a non-zero Rabi rate, the pulses in the global and individual addressing paths must have temporal overlap. One complication present in our individual addressing scheme is that fibers have a tolerance to their lengths that is greater than a few millimeters. Since the 10 ps duration of the pulses from our laser translates to a distance of around 3 mm, this means that the pulses out of each channel of the individual addressing system will arrive at significantly different times to the ions. Hence a single position of the global beam delay stage cannot be used to accommodate all channels. To ensure that pulses from all IA channels arrive simultaneously at the ions, variable delays must be introduced into the individual addressing path as well. Further, if the difference in fiber length between two channels is beyond what a fiber delay line, with a travel range of 4 mm, can accommodate, the fibers for those channels can be spliced so that it is within the 4 mm range of the delay lines. Our initial thought for detecting pulses was to place a fast photodiode after the IA telescope and view the waveforms with a high bandwidth oscilloscope. Unfortunately, due to the bandwidth limitation of both devices, the 10 ps pulses generated by the laser were broadened to > 100 ps. To make things worse, the unequal rise and fall response of the oscilloscope, resulted in pulses that appear asymmetric. This is shown in figure 4.15 (a). With this method we were not able to detect a difference in the pulse arrival times between different channels of the IA system.

The solution we came up with instead for optimizing the temporal overlap was to send light from two channels of the individual addressing system through the IA telescope and image the resulting interference pattern. If there is no overlap between the pulses then no interference fringes will be detected on the camera. The overlap can be optimized by maximizing the contrast of the resulting fringes. This is shown in figure 4.15 (b). Prior to optimization the fringes are faint and hard to detect but after optimization, we see a clear interference pattern with large fringe contrast. For further fine tuning of the spatial and temporal overlap, the measured Rabi frequency or AC stark-shift at the ions can be maximized.

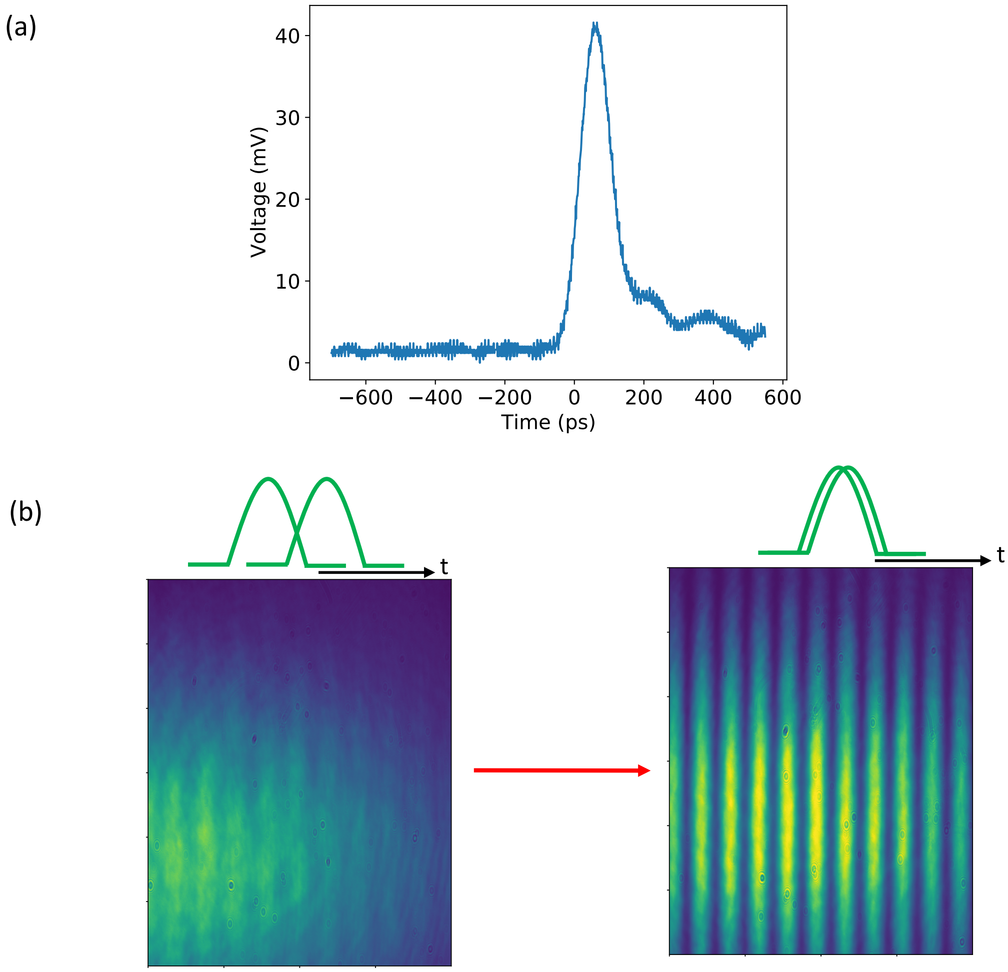

Figure 4.15: (a) Single pulse from the Raman laser measured using a fast photodiode and oscilloscope. The 10 ps pulses are broadened and asymmetric due to the limited bandwidth of both the oscilloscope and photodiode. (b) Images of the interference pattern formed when two channels from the VGA are sent through the IA telescope. The fringe contrast can be used as feedback for moving the fiber delay lines to improve temporal overlap between the two channels.

4.4 Quantum dynamics

In this section we will discuss how the optical parameters of the IA system that we outlined in the previous sections relate to the quantum mechanical parameters of interest such as the two-photon rabi rate, the AC-stark shift and gate fidelities. Given the upper bound on the amount of available power, and the beam parameters in the individual and global paths, we can obtain an estimate of the effective two-photon rabi frequency. Taking into account coupling to both the $P_{1/2}$ and $P_{3/2}$ excited states, it can be shown that this is given by [105, 142]:

$$\Omega = \frac{g_b g_r}{3}(b_- r_- - b_+ r_+)\frac{\omega_f}{\Delta(\Delta - \omega_f)} \tag{4.5}$$

where ω_f is the fine structure splitting between the $P_{1/2}$ and $P_{3/2}$ levels, Δ is the detuning from the $P_{1/2}$ level and b_-, r_-, b_+, r_+ are the left and right circular polarization components of the red (r) and blue (b) detuned beams involved in the raman process. By picking the polarization of the two beams to be linear but orthogonal ($b_- = r_- = b_+ = -r_+ = 1/\sqrt{2}$), we can maximize the rabi rate as discussed previously. Finally $g_{b/r} = E_{b/r} |\left\langle P_{3/2}, F = I + 3/2, m_F = F \middle| \boldsymbol{d} \cdot \hat{\sigma}_+ \middle| S_{1/2}, F = I + 1/2, m_F = F \right\rangle| / 2\hbar$ where $E_{b/r}$ is the electric field amplitude at the position of the ions. This can be related to the optical power using the relationship between electric field and intensity, $E = \sqrt{\frac{2I}{c\epsilon_0}}$, and the relationship between power and the peak intensity of a gaussian beam, $I = \frac{2P}{\pi\omega_x\omega_y}$. Here ω_x and ω_y are the beam radii along the two principal axes of an elliptical beam. Using the Wigner-Eckart theorem one can show that the above matrix element is equivalent to the reduced matrix element $\langle J = 3/2 | \, | e\boldsymbol{r} | \, | J' = 1/2 \rangle$ [132]. The lifetime of the $P_{3/2}$ state can then be used to compute this quantity using [132]:

$$\frac{1}{\tau} = \frac{8\pi^2}{3\epsilon_0 \hbar \lambda^3}\frac{2J+1}{2J'+1} |\langle J| \, |e\boldsymbol{r}| \, |J'\rangle|^2 \tag{4.6}$$

where $\lambda = 455$ nm is the wavelength of the transition and τ is the lifetime of this excited state. The rabi rate is shown in figure 4.16 (a). For our choice of laser wavelength, denoted by the red dashed line in the figure, we obtain a rabi frequency of 0.9 MHz. Another quantity of interest is the differential AC stark shift caused by the off resonant coupling of the ground clock states to the excited states by the red and blue detuned beams. At the position where our laser is parked this shift is less than 0.2% of the rabi frequency (around 2 kHz) and is relatively constant with detuning. This is plotted as a function of detuning in figure 4.16 (b). While qubits encoded in the hyperfine levels of an ion have very long radiative lifetimes, spontaneous emission from the 2p levels during a Raman gate will lower the coherence time of the qubit. This sets a fundamental limit on the achievable gate fidelities as $F \geq 1 - P_{SE}$ [105]. For our laser parameters, the probability of a Raman scattering event is less than 10^{-5} and thus is not the bottleneck limiting gate fidelities.

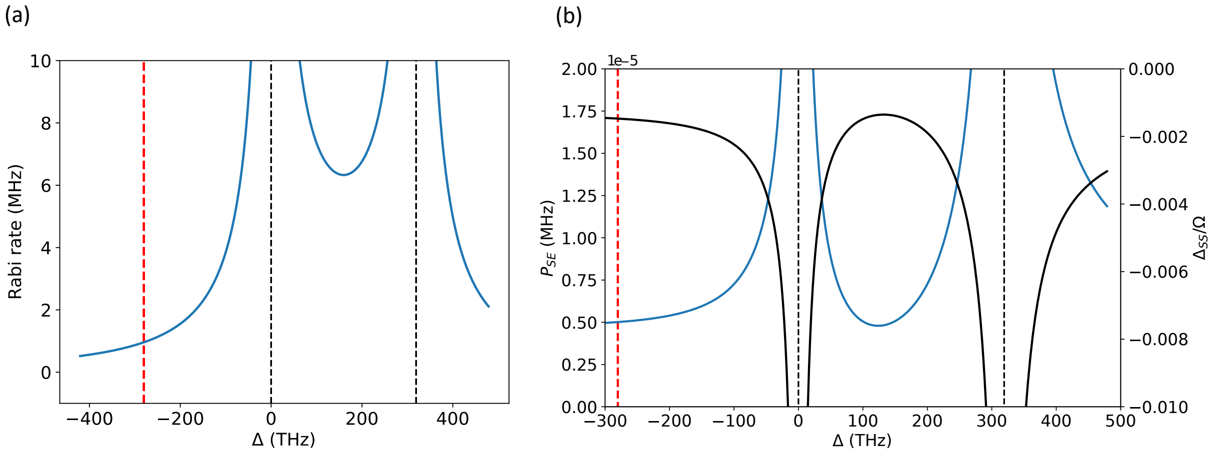

Figure 4.16: (a) Rabi frequency for single qubit gates driven by a pair of Raman beams in the lin-perp-lin configuration. Δ is the detuning from the $P_{1/2}$ excited state. The dashed red line denotes the position of our 532 nm pulsed laser and the two black lines denote the position of the $P_{1/2}$ and $P_{3/2}$ transitions. For our choice of laser frequency, power, and beam size, the rabi rate is around 0.9 MHz. (b) blue: The probability of spontaneous emission during a π pulse as a function of detuning. Black: The differential AC stark shift, in units of the rabi frequency. For our experimental parameters, the spontaneous emission probability is around 5e-6. This sets a fundamental limit on the possible gate fidelity.

4.5 Conclusion

This chapter started by covering how gates can be implemented on hyperfine qubits using Raman transitions implemented with a pair of frequency combs. We then discussed and characterized the unique individual addressing system, based on laser written waveguides and microlenses, for realizing these quantum gates in practice. The system exhibits an intensity crosstalk on the order of 10^{-4} which is comparable to or better than systems currently deployed in other ion trap setups. At the same time it provides simultaneous and independent control over the frequency of each channel but comes with the added overhead of requiring all channels to be path length matched. We provided a solution to this path length matching problem by using the fringe contrast from the interference pattern between pairs of channels. We ended by calculating the expected Rabi rate and stark shift of the qubit based on the characterization of our IA system discussed in this chapter.

Chapter 5

Vacuum system and Trapping Electronics

In this chapter we will discuss the apparatus used to achieve ultra-high vacuum as well as the circuitry required for generating a stable trapping potential.

5.1 The Vacuum system

For successful operation of a quantum experiment, the ion chain needs to be placed under ultra-high vacuum (UHV) conditions to minimize interaction with background gasses. Collision of a residual gas atom or molecule with an ion in the chain can eject ions from the chain, causing the chain to melt or decohere the internal or motional state of the ion. Collisions are classified as elastic, if they only modify the kinetic energy of the ion, or inelastic if they also modify the internal or motional state of the ion. For example they can excite the ion to some metastable state (such as the $D_{5/2}$ in barium or $F_{7/2}$ in ytterbium). Inelastic collisions can also result in the formation of a molecule or molecular ion. For example, reaction of the barium ion with residual H_2 gas, the primary gas present under UHV, leads to the formation of BaH^+ [145]. Reaction with other residual gasses such as CO_2 and H_2O will result in the formation of other molecular ions. Once either of these phenomena take place, the ions stop scattering light during Doppler cooling and so are said to go dark. The rate at which dark ions appear in the chain can be used as a method of measuring the pressure inside the chamber [106]. Another technique for measuring the pressure involves creating a double well axial potential in a surface trap. If an elastic collision imparts the ion with enough energy to overcome the barrier of the double well, the ion will hop from one well to the other. The hoping rate is proportional to the pressure near the ion trap [46]. A similar technique increases the axial trapping potential to the point of generating the zig-zag configuration and measures the rate at which the chain hops between the two degenerate zig-zag configurations [106]. Using the ion as a way of measuring the pressure inside the chamber is often useful as typically vacuum gauges are located relatively far away from the chain and so do not provide the most relevant measure of the pressure.

UHV typically refers to pressures below 10^{-9} and greater than 10^{-12} mbar. Any pressure below this value is classified as extreme high vacuum (XHV). Most ion trap vacuum systems operate in the UHV range at room temperature with typical pressures on the order of or less than 10^{-10} mbar. XHV conditions can also be attained in ion trap experiments by using a cryogenic system [106].

5.2 Generating Ultra-high Vacuum

The ultimate pressure of a vacuum system is a result of the equilibrium reached between the effective pumping speed of the pumps, out-gassing from the chamber surface or internal components necessary for trapping, real or virtual leaks, permeation of gasses through the viewports and the finite compression ratio of the pumps. No one pump can be used to generate UHV conditions. A combination of several different types of pumps, used at different pressure regimes, are required to do so. For our system, we use a combination roughing and turbo-molecular pump to establish high vacuum conditions. A non-evaporable getter (NEG) pump, in conjunction with a titanium sublimation pump (TSP) are used to pump the getterable gasses. An ion pump is used for pumping non-getterable gasses, though it does also pump getterable gasses. Getterable refers to reactive gasses that can be removed from the chamber through chemisorption on a surface coated with some material for this purpose, such as titanium. These include gasses such as H_2, N_2, CO_2, CO and O_2. Non-getterable refers to typically non-volatile species such as noble gasses and hydrocarbons that cannot be removed in this manner. With these latter 3 pumps, UHV pressures can be established. A NEG and ion pump are sufficient to reach UHV pressures. The TSP was included as a backup, in case of NEG failure. In the following sections, our chamber, its pumps, gauges and internals will be discussed in more detail.

5.3 The Vacuum Chamber

An image of our vacuum system is shown in figure 5.1. The system can be divided into 3 sections. The top Kimball chamber, which we call the Diagnostic chamber, the five-way cross, and the bottom Kimball chamber, which we call the experimental chamber.

5.3.1 The Diagnostic chamber and the gauges

The diagnostic chamber is used to mount all the gauges for the system. This includes an extractor gauge, a cold cathode and Pirani combination full-range gauge and a residual gas analyzer. An all-metal bakeable valve is also mounted on one port of the diagnostic chamber. This is where the Turbo pump will attach for the initial pump down, before the main UHV pumps are turned on. While most of our vacuum components are made from titanium, the diagnostic Kimball chamber is made out of stainless steel as the ConFlat (CF) flanges on all the diagnostic equipment are also made from stainless steel. This would help minimize the potential of leaks developing due to a mismatch of thermal expansion coefficients between two different materials. The five-way cross, the experimental chamber and the re-entrant viewports for the Raman and imaging systems are all made out of titanium. This significantly reduces the total mass of the chamber, which weighs under 200 lbs [51]. If only stainless steel was used in the construction, the system would have weighed more than 300 lbs. Another merit of titanium is that it has a lower out-gassing rate compared to stainless steel and this difference can be as much as two orders of magnitude [51, 72].

For the measurement of the vacuum pressure, we make use of a Pirani gauge, a cold cathode gauge and an extractor gauge. At low to medium vacuum (1000-10^{-4} mbar) a Pirani gauge measures pressure through the change in temperature of a heated metal coil that occurs as gas molecules collide with the coil. The smaller mean free path at higher pressures results in a higher thermal conductivity between the filament and the surroundings, causing the probe to lose heat at a faster rate [3]. In this way the pressure can be measured by for example measuring the change in resistance of the coil.

Both the cold cathode and extractor gauges can be operated below 10^{-4} mbar. The cold cathode gauge consists of a cylindrical anode placed in between two planar cathodes [3, 65]. A large voltage, on the order of several kilovolts, between these electrodes causes a discharge of electrons and these electrons are set into helical motion by a magnetic field along the axis of the anode. These electrons ionize gas molecules in the chamber which are subsequently accelerated towards the cathode. The magnetic field is used to increase the transit time of the electrons from the cathode to anode, in order to increase the ionization probability. Since the ionization rate is proportional to the gas density, the current generated in this way is used to measure the pressure. The name cold is used to distinguish it from another type of ionization gauge, the hot cathode gauge, which instead generates electrons using a heated filament cathode [65]. These electrons are then accelerated towards a helical shaped anode. A thin wire at the center of the anode grid, held at a negative potential relative to the anode, collects the ions produced by the accelerated electrons. The resulting current on this wire gives a measure of the pressure. The smallest pressure such a gauge can measure is limited by photo-electrons on the collection wire generated from x-ray radiation that is emitted when the accelerated electrons collide with the anode grid [3]. This is the so called x-ray limit and as a result, hot cathode gauges can measure pressure in the range 10^{-4}-10^{-10} mbar. To go beyond this limit, an extractor gauge can be used, which is analogues to the hot cathode gauge but uses a shorter and slimmer collection electrode that is removed from the line of site of the anode. This minimizes the spurious current from x-rays and as a result, such a gauge can measure down to 10^{-12} mbar [51, 3, 65].

The last major component of the diagnostic chamber is the residual gas analyzer (RGA). The RGA measures the partial pressure of gasses that are present in the chamber and is primarily used to diagnose problems with the vacuum system. For example, it is often used to perform leak checks while spraying helium on the flanges from the outside. The RGA works by first ionizing gasses in the chamber, using electrons generated from a heated cathode filament, and then accelerating them towards a quadruple mass filter, a 4 rod ion trap [7]. The RF and DC voltages on the rods are used to select a particular charge to mass ratio of ions to send to the detector cathode. Other ratios of e/m will have unstable trajectories and as a result, will not make it to the detector. With an electron-multiplier add-on, partial pressures below 10^{-10} mbar can be detected [51].

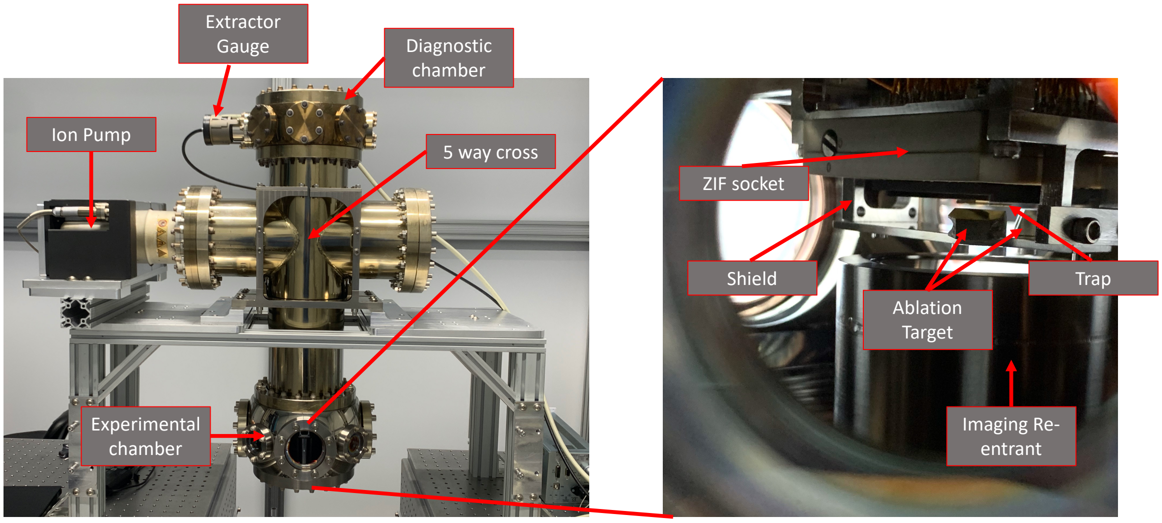

Figure 5.1: left: Image of the exterior of our vacuum chamber. The top stainless steel Kimball chamber is where all the diagnostic equipment are mounted (extractor gauge, full range gauge and RGA). The five-way cross mounts the ion pump and TSP (not shown) at two of its ports and the two Kimball chambers at the other two. The final port is left blank. Right: Inside the experimental chamber, showing the trap, electric field shield, ablation targets and the imaging re-entrant.

5.3.2 The Five-Way Cross and The Pumps

The five-way cross segment of the chamber houses all the vacuum pumps necessary to get down to UHV pressures. As stated previously, the ion pump is primarily used to remove non-getterable gasses. The principle of operation for this pump is very similar to that of the cold cathode gauge where electrons, placed in helical motion by a large magnetic field ($\sim$ 0.1 T) generated by permanent magnets outside the vacuum, ionize gasses in the chamber [2]. These positively charged gas atoms are not significantly affected by the magnetic field due to their larger mass and are directly accelerated towards the titanium cathode. The gas can react chemically with the titanium (this is the case for getterable gasses, for example forming TiN or TiO_2), forming a solid that no longer contributes to the pressure. The ions also have enough energy to get buried into the cathode electrode or bounce back as a high energy neutral and get buried into the anode. This allows for the pumping of gasses that are not reactive with titanium i.e. non-getterables such as the noble gasses. These collisions additionally sputter some of the titanium onto the other surfaces of pump such as the anode. This prevents the permeation of the non-getterable gasses buried in these surfaces and provides further surface area for chemisorption of getterable species [6]. Just like the cold cathode gauge, the current generated in this pumping process can be used to measure the pressure of the chamber. We have a Starcell type ion pump which has a unique electrode geometry that increases the pumping speed of noble gasses as well as methane while still providing a high pumping speed for H_2 [51]. The bombardment of the cathode by the accelerated ions erodes the surface of the cathode and eventually, the pump releases the buried noble gas population resulting in a spike in the pressure [118]. This instability can be avoided by increasing the likelihood of forming high energy neutrals that reflect towards the anode. This is done through modifications in the electrode material or geometry.

The other pump present in this section is the TSP. A TSP consists of several titanium filaments that are resistively heated to the point of sublimation and used to coat the inside wall of the vacuum chamber. Typically an element with large surface area (sputter shield) surrounds the filaments so that the surface area that is coated by the titanium is maximized. As titanium is more reactive at lower temperatures, sometimes a shield with a liquid nitrogen feed-through is used to cool the coated region. This pump removes getterable gasses as they collide and react with the deposited titanium. Activating the TSPs, that is sputtering a fresh coat of titanium on the chamber walls, runs the risk of saturating the NEGs due to the increased outgassing of species such as methane [45] that occurs during this process. Further, due to the placement of the NEGs, the TSPs have a reduced conductance to the experimental chamber, making them a less effective pump. As a result, the TSPs are used as a backup, in the case of NEG failure.

The final pump present on our system are the non-evaporable getters. These are placed near the center of the five-way cross, inside the chamber. They are held in place by groove grabbers attached to the top and bottom Kimball chambers. The NEGs are made up of a reactive metal or an alloy that pumps getterable gasses through chemisorption or physisorption [51]. An ingot of the active material is ground and then compressed or sintered into disks, forming a porous surface that increases the surface area for reaction with the gasses in the chamber [88]. When H_2 reacts with the NEG's surface, it dissociates and diffuses into the bulk while when other getterable gasses react, they form oxides, carbides, nitrides and other chemical compounds on the surface of the NEG [88]. Once the surface is saturated with adsorbed gasses, the pump can be re-activated by resistively heating the getter material to 400-500 °C. Chemical compounds that adsorbed on the surface diffuse into the bulk, while the embedded hydrogen diffuses to the surface and is released back into the chamber as H_2 gas. Our specific pump is made up of ZrVTiAl and has a pumping speed of 1400 L/s for hydrogen at 10^{-6} mbar [51]. For a properly designed and baked vacuum system, the most abundant gas in the chamber is H_2. As a result, these are the most important pumps in the system for achieving UHV conditions [9].

5.3.3 The Experimental Chamber

The experimental chamber houses the trap and the barium ablation targets used to load ions into the trap. It consists of 8 viewports (3 re-entrants) that are used to deliver light to the ions or collect fluorescence emitted during cooling or measurement. The final port on the experimental chamber is a feedthrough, used to deliver electrical signals (both RF and DC) to and from the trap. The feedthrough consists of a DB-100 connector, used to deliver DC voltages to the trap. On the outside of the chamber a custom PCB is used to split this into 4 DB-25 connectors for ease of organization and on the inside, the signals are carried by individual Kapton coated copper wires and soldered onto the Zero-Insertion Force (ZIF) socket onto which the trap mounts. We initially tried to use a flexible printed circuit board for this purpose but was unable to cleanly solder the PCB without developing any shorts. The feedthrough also has 12 short copper leads. Currently, one of these is used to deliver the RF signal, required for radial confinement, to the trap. The trap contains a pair of capacitors (C_1=0.25 pF and C_2=60 pF) that are used to step down the RF voltage from the resonator by a factor of ~ 240[1]. This is used to sample the RF signal for the purpose of feedback and stabilization of the secular frequency. This signal comes out another one of the 12 copper leads.

These internal elements significantly contribute to the gas load in the chamber and can prevent us from achieving UHV. In the next section we will discuss how heat treatment is used to reduce this outgassing rate to a level that makes UHV attainable.

5.4 Heat Treatment of Vacuum Components

The materials most commonly used for the construction of vacuum systems are the austenitic alloys of stainless steel, specifically those from the 304 and 316 series [51]. These have the desirable property, as far as the atomic physics is concerned, of being non-magnetic. They also have a low out gassing rate, given proper heat treatment [51]. Hydrogen gas is dissolved in stainless steel during fabrication. Under vacuum, hydrogen diffuses towards the surface of the steel, combines with another hydrogen atom, forming H_2 gas. This desorption of hydrogen is the largest component of the outgassing rate of stainless steel and must be reduced to achieve UHV conditions. Since the diffusion of defects through the

---

[1] In reality the measured attenuation is -52dB at 50 MHz [112].

bulk of a material is proportional to $e^{-E_0/RT}$ where E_0 is the activation energy, raising the temperature of a chamber for a relatively short period of time can be used to reduce the concentration of dissolved H atoms, thereby reducing the outgassing rate of H_2. To lower the outgassing rate, several different types of heat treatments are used. The chamber can be heated to > 900 ° C inside a vacuum furnace for several hours; this is called vacuum firing [119]. Other common methods are the medium heat treatment vacuum and air bakes. In the vacuum bake, the temperature of the chamber is raised to 400-500 °C for one to two weeks under high vacuum. An air bake is done at similar temperatures for a few days and results in the formation of an oxide layer that has been shown to reduce the outgassing rates. The former two techniques lower outgassing by decreasing the concentration of dissolved hydrogen while the latter method creates an iron oxide layer that hinders the diffusion of hydrogen. Using a medium temperature vacuum bake at a temperature of 430 °C for 15 days, [119] reports an outgassing rate of 10^{-11} Pa·l/s/cm^2, a two order of magnitude reduction, compared to untreated stainless steel. Following this by a one-day air bake at the same temperature, they were able to further decrease the outgassing rate by a factor 2.

For the stainless steel components of our chamber we decided to opt for a medium temperature vacuum and air bake, due to equipment availability. The components being baked include the diagnostic chamber, several blanks, as well as the TSP's sputter shield. The baking setup is shown in figure 5.2. A four-way cross is attached to a turbo Pump unit with a diaphragm roughing pump. Two gauges are connected to the four-way cross through two nipples to reduce the thermal conductivity, preventing the gauges from going beyond their maximum operation temperature. The diagnostic chamber is attached on top of the four-way cross with the sputter shield mounted on top of it. Thermocouples were attached at several points on the chamber to monitor the temperature and temperature gradients. Next, the chamber was wrapped in aluminum foil and then three electrical heating tapes were wrapped around the chamber. The entire apparatus was then covered with another layer of foil and fiber glass insulation. Additional thermocouples were added near the gauges and the turbo pump to ensure that the equipment does not get dangerously hot. The chamber was pumped down to around 10^{-6} mbar and the temperature was then slowly increased to 400 °C to prevent over shoot. This was maintained for 10 days and followed by a one-day air bake. This process is often referred to as a "pre-bake" because it is always followed by a lower temperature heat treatment that is intended to remove any water that has adsorbed on the chamber due to air exposure. This is done once the chamber is fully assembled.

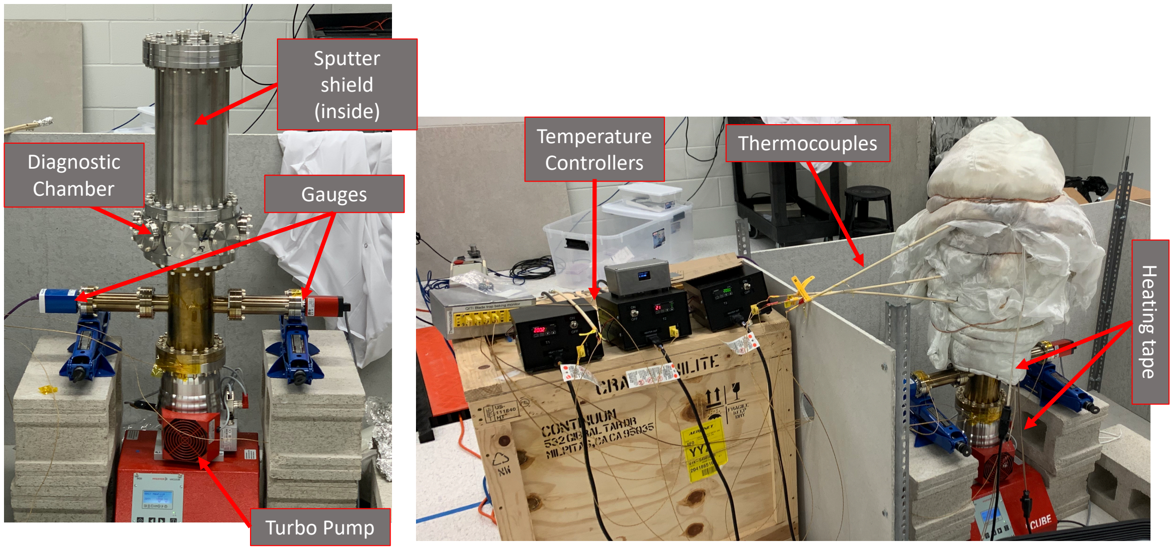

Figure 5.2: Left: Stainless steel vacuum components involved in the medium temperature bake process. Right: The fully assembled prebaking setup. Several electrical heating tapes are used to control the temperature of the chamber. Each tape is wrapped near one thermocouple on the chamber and the temperature reading from these sensors are used as the feedback for temperature control. Aluminum foil and Fiberglass are used for thermal insulation.

For the titanium components of our chamber, baking is also necessary to reduce the outgassing rate, however, the requirements are quite a bit more modest and yield a superior outgassing rate. For example, [72] obtained an outgassing rate of $7{\cdot}10^{-14}$ Pa·l/s/cm^2 after only a 20 hour heat treatment at 120 °C, roughly a 3 order of magnitude improvement over the non heat treated titanium. The internal components of the experimental chamber are the most significant source of outgassing. Specifically the ZIF socket, made out of PEEK, has an outgassing rate of $4.1{\cdot}10^{-9}$ Pa·l/s/cm^2 after a 12 hour bake at 150 °C [103] and the Kapton from the wires that deliver DC voltages to the trap have an outgassing rate of $2{\cdot}10^{-9}$ Pa·l/s/cm^2 after a 24 hour bake out at 150 °C [58]. The outgassing data quoted from the literature only serves as a qualitative guide as many variables affect a specific sample's outgassing rate including sample thickness and the details of the baking procedure.

The previously discussed medium temperature bake out is not sufficient to attain UHV. When a chamber is exposed to air, water adsorbs on its internal surfaces, and when placed under vacuum, the outgassing of this adsorbed water becomes the dominant gas load inside the chamber [33, 52]. To achieve UHV, this adsorbed water must be removed from the chamber. For our system, this was done by placing the entire chamber inside an oven, evacuating the system with a turbo pump, and baking the chamber and all the internals at 195 °C for several days. This removes most of the adsorbed water so that hydrogen becomes the dominant gas source at UHV. This also serves as the heat treatment of the ZIF socket, Kapton wires and other internal components which is required to lower their total outgassing rate as discussed above. Due to the large outgassing rate of the PEEK ZIF socket we also tried baking it at this temperature for a longer period, over a week, with the trap removed, but did not notice a change in the base pressure.

While outgassing from surfaces internal to the chamber is often the main gas load, other sources, such as leaks make a significant contribution as well. There are 8 viewports on the experimental chamber, one electrical feed-through and one regular CF flange connection. The maximum leak rate of our viewports is 10^{-9} mbar l/s for He gas. For the feedthroughs, this is less than $2 \cdot 10^{-10}$ mbar l/s and for the CF flanges it is less than 10^{-11} mbar l/s. CF flanges use a soft metal gasket such as (oxygen free) copper; each flange face has a circular sharp edge, called a knife edge, that digs into the gasket and provides a seal sufficient for attaining UHV and XHV [51]. The plastic deformation of the copper that occurs when the flange is bolted down hardens the copper and as a result, these gaskets must be replaced each time the seal is broken [10]. Further, heating a chamber beyond 450 °C for long periods causes the gasket to partially anneal, potentially resulting in the development of leaks as the temperature is lowered [51, 10]. This is why for the prebake step, we did not exceed 400 °C.

For more details on vacuum systems and the design of this chamber, refer to [51].

5.5 Trapping Electronics

As discussed in chapter 2, by using a combination of radio frequency and DC voltages, an effective pseudopotential can be generated that is trapping in all three dimensions despite Ernshaw's theorem. This potential is approximately harmonic, with frequency:

$$\nu_{sec} = \frac{eV_0}{\sqrt{2}m\Omega_{rf}r_0^2} \tag{5.1}$$

where V_0 is the amplitude of the RF signal and ω_{rf} is the frequency. From this it is clear that to obtain a deep trapping potential, which leads to long chain lifetimes, we require a large RF voltage. The large secular frequency that comes from having a large RF voltage results in more efficient cooling of the motional modes as well as faster entangling gate speeds [126]. These voltages cannot be too large, otherwise RF breakdown occurs, causing the electrodes to short and rendering the trap useless. Given the electrode-electrode separation of our surface trap, a safe operating voltage is around 250 V. Even if breakdown was not a problem, a separate upper bound is placed by the necessity to minimize micromotion, that is, have a small Mathieu q parameter.

Most RF sources and amplifiers have a 50 Ω resistive impedance, on the other hand, the ion trap has primarily a reactive impedance. Maximum power transfer occurs when the source and load have equal impedances where the amount of reflected power due to an impedance mismatch is given by $|\Gamma|^2 = |\frac{Z_t - Z_0}{Z_t + Z_0}|^2$. Here Z_t is the trap impedance and $Z_0 = 50\ \Omega$. So for stable trapping of ions, we require a circuit that amplifies the RF voltage and impedance matches the source to the ion trap. Both of these are done with a helical coil resonator circuit, which is effectively a series RLC circuit. This is shown in figure 5.3 (a). The inductance is provided by the larger helical coil. The capacitance of the circuit is a combination of the self-capacitance of the coil, the capacitance between the coil and the shield surrounding the coil as well as the capacitance of the trap and the associated wiring. An RF signal is inductively coupled to the RLC circuit through a smaller coil. By modifying the pitch, diameter, number of turns of the coil, as well as the distance between the two coils, an impedance match between the RF source and the trap can be achieved [126].

The design guides provided in references [126, 87, 39] can be used to construct such a resonator given a desired resonance frequency. This is determined by the number of turns of the coil, the pitch between the turns of the coil, the coil and shield diameter, as well as the coil and shield height. The resonator is connected to the trap using a feed through on the experimental chamber. It is important to keep the length of the wires connecting the resonator to the trap short, to minimize the amount of added capacitance. This is because $Q = \frac{1}{R}\sqrt{\frac{L}{C}}$ and so any added capacitance and resistance will reduce the Q factor of the device. The amplitude of the RF voltage provided by the resonator is proportional to $V_0 \propto \sqrt{2PQ}$, where P is the power coupled into the circuit [126]. Thus the higher the Q, the larger the RF voltage delivered to the trap. However, if the Q is too large, then fluctuations in the resonance frequency of the circuit due to for example vibrations or thermal effects can result in significant fluctuations in the delivered voltage. With the typical Qs of < 1000 attained with such circuits in ion trap experiments, this is not a major concern however, to maximize two qubit gate fidelities, stabilization of the secular frequency, through stabilization of the voltage provided by the resonator to the trap, is necessary [64]. Figure 5.3 (b) shows an image of our resonator, including the main resonator coil and the coupling coil. Finger stocks surround the cap of the resonator to improve the quality of the connection to the main body of the device. The main coil was constructed by wrapping an AWG 4 bare copper wire around a 3D printed scaffolding. The antenna wire was made by wrapping a thinner piece of copper wire around a Thorlabs pedestal. The main coil is shorted at one end to the shield using a copper lug and then soldered to reduce the joint resistance. We use a RF drive of around 45 MHz for our experiments, so our helical resonator has a loaded resonance frequency (i.e., the resonance frequency of the circuit when the device is connected to the trap) around this value. The device was designed with an unloaded resonance near 80 MHz as the trap and the associated wires were estimated to add roughly an additional 16 pF which will cause the resonance frequency to drop to around 45 MHz.

To determine the resonance frequency of the built circuits, a vector network analyzer (VNA) can be used to measure the scattering parameters of the device. If a VNA is not available, a spectrum analyzer along with a directional coupler can be used to measure the S_{11} coefficient, or the reflected power, by measuring the signal from the coupled port of the directional coupler. Resonances appear as sharp dips in the reflected signal. This technique can also be used to monitor the resonance frequency of the device when the resonator is connected to the trap. Connecting this reflected signal to an oscilloscope instead, can be used to monitor for RF breakdown [141]. To avoid break down and the formation of catastrophic shorts between the electrodes, the voltage should be ramped up slowly, while monitoring the transient signature of RF breakdown on an oscilloscope. Figure 5.3 (c) shows a plot of the reflected signal which we use to determine the unloaded resonance frequency and Q factor of the device. We measure a resonance frequency of around 74 MHz, which is slightly lower than the target 80 MHz. As a result, the loaded frequency will be slightly lower, depending on how accurate the 16 pF estimate is. We measure an unloaded Q factor of 340, which is more than enough to provide the required 250 V RF signal. By adjusting the height and pitch of the input coupling coil, the amount of reflected signal on resonance was suppressed by -22 dB. Therefore, less than 1% of the input power is reflected due to the impedance match provided by the coupling coil.

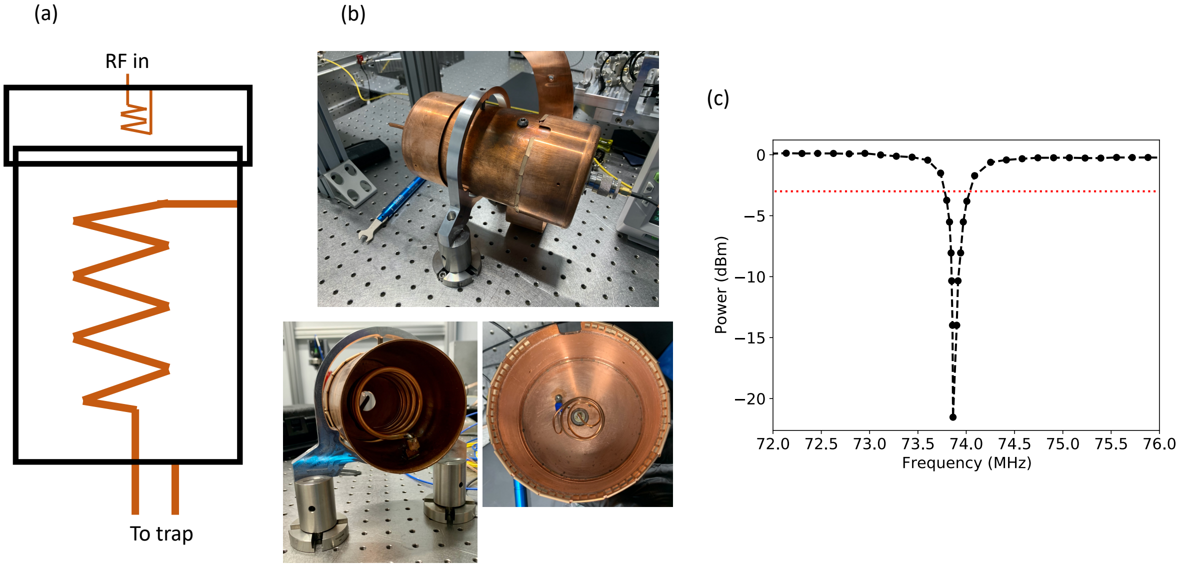

Figure 5.3: (a) Schematic of a helical coil resonator. The device consists of a larger coil, grounded at one end to a cylindrical shield surrounding it. A smaller coil is used to couple RF power into the circuit from an amplifier as well as to impedance match the 50 Ω resistance of the source to the trap. (b) Images of our resonator and (c) plot of the signal reflected from the resonator as measured on a spectrum analyzer. The resonance frequency is around 74 MHz. The dashed red line is used to mark the full width at half maximum (FWHM) point (-3 dB). The FWHM is around 217 kHz, yielding a Q factor of 340.

5.6 Conclusion

This chapter covered the elements of our vacuum chamber used to measure and achieve UHV conditions. We discussed the theory of operation of each element and the role each plays in our system. We further discussed the heat treatment procedures followed to obtain low outgassing rates from all internal surfaces of the vacuum chamber. This chapter also covered the resonator circuit used to deliver a high amplitude RF voltage to the trap. The resonator has a Q factor of 340 which is more than enough to supply the required 250 V RF amplitude to the trap.

Chapter 6

Conclusion and Outlook

This thesis discussed the construction and bring-up of an ion trap quantum computer, focusing primarily on the optical requirements necessary to make quantum information processing and quantum simulation possible with ions. Chapter 2 discussed how a linear chain of ions can be trapped and cooled in a radio frequency Paul trap. We discussed how the shared normal modes of the chain effectively wires each ion in the chain to all others and how this can be used to implement two qubit entangling gates to realize universal quantum computation with ions. We also covered how the same interaction can be used to realize arbitrary spin models, given control over the amplitude and frequencies of light shining on each ion. Chapter 3 focused on the optical manipulation of ions for laser cooling, state preparation and quantum state detection. These operations are implemented using continuous wave lasers near 493, 614, and 650 nm with 405 nm and 553 nm used for photoionization. We discussed the atomic physics requirements that were considered when designing the optical systems used to deliver these wavelengths to the ions and characterized their performance by taking high dynamic range images of the beam profile at the location of the ions. In the next chapter we discussed how frequency combs can be used to implement Raman transitions for performing single and two qubit gate operations on ions. We also discussed and characterized our unique individual addressing system, based on laser written waveguide technology, that allows for the implementation of two qubit gates between arbitrary pairs of ions in the chain. Our novel approach exhibits low intensity cross talk, on the order of 10^{-4} while allowing for parallel and independent control over frequency, phase and amplitude of each channel. Finally, in chapter 5 we discussed the construction of our vacuum system as well as the helical resonator used to provide a high voltage RF signal to the trap.

At the time of writing this thesis we have just moved our vacuum chamber out of the clean-room and placed it on the optical table. The immediate next step for the project is to align the imaging system and try to image the trap electrodes on our imaging camera. Simultaneously we are working on determining what went wrong with our vacuum system as the measured base pressure is currently too high ($\sim 10^{-9}$ mbar). We suspect outgassing from the soldered connections is part of the problem. Currently there are no radioactive sources in our chamber. We are preparing and characterizing several sources and will add these once the issues with the vacuum pressure have been resolved. Once the system is fully functional, many avenues of novel research can be explored. Some examples include demonstration of robust loading of long chains of $^{133}\mathrm{Ba}^{+}$, demonstration of entangling gates between pairs of ions in such a chain using our novel individual addressing system or the demonstration of entanglement between multiple isotopes of barium.

This thesis covered the design and construction of the optical systems required to build a 16 qubit ion trap quantum computer based on barium ions. Our design, while perfectly fine for addressing a single small array of ions, makes use of bulk optical elements outside the vacuum chamber and as such, is not easily extensible to a large number of ions trapped in multiple zones on a single chip trap, and/or in multiple disparate chip traps, connected through photons. To optically address such a complex network of ions, advances in integrated photonic technologies that combine light delivery, modulation, collection, and detection with the trapping electronics will be necessary. Certain elements of such an approach have already been demonstrated including ion light delivery using photonic waveguides and focusing grating couplers [91]. The authors of [102] demonstrate on chip delivery of all the wavelengths required to ionize, cool, and perform state preparation and detection as well as implement quantum logic gates on a single $^{88}\mathrm{Sr}^{+}$ ion. The authors of [93] demonstrate entangling gates between two trapped $^{40}\mathrm{Ca}^{+}$ ions however, the shorter wavelengths required for Doppler cooling, detection and photoionization are delivered in free-space, due to the larger losses at these wavelengths. Beyond scalability, a major advantage of this approach over the use of free-space beams is that the system is not susceptible to fluctuations in beam position due to vibrations as both the trap and the delivery optics move together. Other fundamental demonstrations in this area include the on chip integration of detectors. Reference [136] for example integrated a single superconducting nano wire single-photon detector into their trap, achieving a readout fidelity of 99.91% with a 46 μs measurement time.

These demonstrations focus on a single or a handful of ions in the trap and significant challenges lie ahead for scaling such an architecture. Foremost are losses in the waveguides as well as the grating couplers, especially at shorter wavelengths. Further, while diffraction limited performance has been achieved using grating couplers [92], these devices are not dynamically re-configurable, which can be useful if one needs to sweep a single focused source across an ion chain for individual addressing. Additionally, the use of such diffractive elements for the generation of arbitrary or tailored beam profiles at the ions is largely unexplored [98]. Integrated beam steering may be accomplished using chip based optical phased arrays, demonstrated for the first time at blue wavelengths in [28] or using a grid of micro-ring emitters placed beneath a lens [24]. Further, diffractive grating couplers may be combined with or replaced by meta-surfaces for greater control over the optical field at the ions. The authors of [147] place a meta-lens with 0.8 NA on top of a grating coupler, achieving a diffraction limited spot of 473 nm at a wavelength of 780 nm. Another design uses light evanescently coupled to the metasurface from a slab waveguide to focus in free-space or generate an arbitrary intensity profile [43]. The use of metasurfaces have relatively recently been exploited in atomic physics experiments. For example, [149] uses a single metasurface to generate 5 of the 6 beams required for a magneto optical trap (MOT). The sixth beam is generated through reflection off of a mirror of one of the five beams. This significantly reduces the size of the system and the quantity of optical elements necessary to create a MOT. Reference [61] uses it as an in-vacuum objective, mounted on the inside of a Pyrex vacuum cell, to focus the tweezer beams generated by a two-axis AOD and to collect fluorescence from neutral ^{87}Rb atoms. The metalens is UHV compatible and can handle temperatures > 200 °C when baking the chamber. To the best of my knowledge no ion-trap experiment has yet made use of this technology.

One challenge with the high density integration of on chip optical elements is the photo-induced charging of the dielectrics that make up the integrated elements. This introduces stray DC electric fields that perturb the trapping potential and result in excess micromotion [16]. Such driven motion cannot be cooled, results in Doppler shifts of the atomic transitions and makes individual ion addressing difficult. This problem is reduced by placing the dielectric elements in openings beneath the surface of electrodes [30] and coating these apertures with a transparent conductor [102] such as ITO to shield the ions from the field of the accumulated charges. This can be further reduced and eliminated by applying DC voltages to the trapping electrodes to offset the remaining stray DC field at the location of the ions. A related problem is anomalous heating of the ion's motional modes due to electric field noise whose spectrum has some overlap with these modes. It is called anomalous since its exact origin is unknown but the dominant source of this noise appears to be from patches of contaminants adsorbed on the electrode's surface [59]. The heating scales as d^{-4}, where d is the ion-electrode distance, and is one factor hindering the further miniaturization ion traps [59].

In current proof of principle demonstrations in integrated optics, beam splitting and modulation are done outside the chamber and multiple sources are delivered to integrated waveguides via optical fibers [91, 92, 93, 102]. For true scalability, beam splitting as well as, parallel and independent frequency, phase and amplitude modulation should also be done on chip. Many relevant transitions in ions are in the blue and UV region of the spectrum and the development of high quality modulators and other active devices for such wavelengths, exhibiting low loss, high extinction ratio and allowing for precise frequency control, is currently an open area of research [98]. Developments in this area will require the exploration of novel nonlinear materials compatible with blue/UV wavelengths. One example material under exploration is Aluminum nitride (AlN) which shows promise due to its large band gap (6.2 eV), making it transparent at ultraviolet and longer wavelengths. AlN also exhibits a large second order nonlinear optical susceptibility [82]. This quality can be used to implement on chip EOMs and can also be used for second harmonic generation [146].

Despite many years of research, the development of a large scale, fault-tolerant quantum computer is still an elusive and daunting goal. Many challenges for scaling the number of qubits lie ahead. Technological developments in integrated optics and nanophotonics will most likely be vital for the success of this platform.

References

[1] Acousto-optical illumination modules. https://www.l3harris.com/all-capabilities/acousto-optical-illumination-modules.

[2] How do ion pumps work? https://www.leybold.com/en/knowledge/vacuum-fundamentals/vacuum-generation/pump-typeshow-do-ion-pumps-work#:~:text=Operating%20principle%20of%20sputter%2Dion,nitrogen%2C%20oxygen%2C%20hydrogen).

[3] A simple guide to vacuum measurement. *Vacuum Science World*.

[4] Technotes: Mismatch / na mismatch and overlap. https://www.sukhamburg.com/support/technotes/fiberoptics/cablebasics/mismatch.html.

[5] Texas instruments dlp9500uv. https://www.ti.com/product/DLP9500UV.

[6] Working with ion getter pumps: Everything you need to know. https://www.vacuumscienceworld.com/blog/working-with-ion-getter-pumps#:~:text=Ion%20getter%20pumps%20require%20a,burial%20of%20the%20ions%20produced.

[7] Residual gas analysers (rga) explained. https://www.vacuumscienceworld.com/blog/residual-gas-analysers-explained, 2019.

[8] Ionq announces new barium qubit technology, laying foundation for advanced quantum computing architectures, Dec 2021.

[9] Ultra-high vacuum systems. https://vaccoat.com/blog/ultra-high-vacuum-systems/, 2021.

[10] Conflat® (cf) uhv flanges components technical notes. https://www.lesker.com/newweb/flanges/flanges_technicalnotes_conflat_1.cfm, n.d.

[11] D. T. C. Allcock, W. C. Campbell, J. Chiaverini, I. L. Chuang, E. R. Hudson, I. D. Moore, A. Ransford, C. Roman, J. M. Sage, and D. J. Wineland. Omg blueprint for trapped ion quantum computing with metastable states. *Applied Physics Letters*, 119(21):214002, November 2021.

[12] Fangzhao Alex An, Anthony Ransford, Andrew Schaffer, Lucas R. Sletten, John Gaebler, James Hostetter, and Grahame Vittorini. High fidelity state preparation and measurement of ion hyperfine qubits with I $>$ 1/2, 2022.

[13] J. M. Arrazola, V. Bergholm, K. Brádler, T. R. Bromley, M. J. Collins, I. Dhand, A. Fumagalli, T. Gerrits, A. Goussev, L. G. Helt, J. Hundal, T. Isacsson, R. B. Israel, J. Izaac, S. Jahangiri, R. Janik, N. Killoran, S. P. Kumar, J. Lavoie, A. E. Lita, D. H. Mahler, M. Menotti, B. Morrison, S. W. Nam, L. Neuhaus, H. Y. Qi, N. Quesada, A. Repingon, K. K. Sabapathy, M. Schuld, D. Su, J. Swinarton, A. Száva, K. Tan, P. Tan, V. D. Vaidya, Z. Vernon, Z. Zabaneh, and Y. Zhang. Quantum circuits with many photons on a programmable nanophotonic chip. *Nature*, 591(7848):54–60, March 2021.

[14] C. J. Ballance, T. P. Harty, N. M. Linke, M. A. Sepiol, and D. M. Lucas. High-fidelity quantum logic gates using trapped-ion hyperfine qubits. *Physical Review Letters*, 117(6), August 2016.

[15] D. J. Berkeland and M. G. Boshier. Destabilization of dark states and optical spectroscopy in zeeman-degenerate atomic systems. *Physical Review A*, 65(3), February 2002.

[16] D. J. Berkeland, J. D. Miller, J. C. Bergquist, W. M. Itano, and D. J. Wineland. Minimization of ion micromotion in a paul trap. *Journal of Applied Physics*, 83(10):5025–5033, May 1998.

[17] S. Blinov, B. Wu, and C. Monroe. Comparison of cloud-based ion trap and superconducting quantum computer architectures. *AVS Quantum Science*, 3(3):033801, September 2021.

[18] R. Bowler, J. Gaebler, Y. Lin, T. R. Tan, D. Hanneke, J. D. Jost, J. P. Home, D. Leibfried, and D. J. Wineland. Coherent diabatic ion transport and separation in a multizone trap array. *Physical Review Letters*, 109(8), August 2012.

[19] Brendan Bramman. Measuring trapped ion qudits. Master's thesis, University of Waterloo, 2019.

[20] Kenneth R Brown, Jungsang Kim, and Christopher Monroe. Co-designing a scalable quantum computer with trapped atomic ions. *npj Quantum Information*, 2(1), November 2016.

[21] E. A. Burt, J. D. Prestage, R. L. Tjoelker, D. G. Enzer, D. Kuang, D. W. Murphy, D. E. Robison, J. M. Seubert, R. T. Wang, and T. A. Ely. Demonstration of a trapped-ion atomic clock in space. *Nature*, 595(7865):43–47, June 2021.

[22] Eric A. Burt. *Demonstration of trapped single laser cooled indium ions.* PhD thesis, University of Washington, 1995.

[23] Allison Levin Carter. *DESIGN AND CONSTRUCTION OF A THREE-NODE QUANTUM NETWORK.* PhD thesis, University of Maryland, College Park, 2021.

[24] You-Chia Chang, Min Chul Shin, Christopher T. Phare, Steven A. Miller, Euijae Shim, and Michal Lipson. 2d beam steerer based on metalens on silicon photonics. *Opt. Express*, 29(2):854–864, Jan 2021.

[25] T. Choi, S. Debnath, T.A. Manning, C. Figgatt, Z.-X. Gong, L.-M. Duan, and C. Monroe. Optimal quantum control of multimode couplings between trapped ion qubits for scalable entanglement. *Physical Review Letters*, 112(19), May 2014.

[26] Justin E. Christensen. *High-fidelity operation of a radioactive trapped ion qubit, 133Ba+.* PhD thesis, University of California Los Angeles, 2020.

[27] Justin E. Christensen, David Hucul, Wesley C. Campbell, and Eric R. Hudson. High-fidelity manipulation of a qubit enabled by a manufactured nucleus. *npj Quantum Information*, 6(1), Apr 2020.

[28] Min Chul Shin, Aseema Mohanty, Kyle Watson, Gaurang R Bhatt, Christopher T Phare, Steven A Miller, Moshe Zadka, Brian S Lee, Xingchen Ji, Ipshita Datta, and Michal Lipson. Chip-scale blue light phased array. *Opt. Lett.*, 45(7):1934–1937, April 2020.

[29] J. I. Cirac and P. Zoller. Quantum computations with cold trapped ions. *Physical Review Letters*, 74(20):4091–4094, 1995.

[30] Craig R. Clark, Chin-wen Chou, A. R. Ellis, Jeff Hunker, Shanalyn A. Kemme, Peter Maunz, Boyan Tabakov, Chris Tigges, and Daniel L. Stick. Characterization of fluorescence collection optics integrated with a microfabricated surface electrode ion trap. *Phys. Rev. Applied*, 1:024004, Mar 2014.

[31] Stephen Crain, Clinton Cahall, Geert Vrijsen, Emma E. Wollman, Matthew D. Shaw, Varun B. Verma, Sae Woo Nam, and Jungsang Kim. High-speed low-crosstalk detection of a 171yb qubit using superconducting nanowire single photon detectors. *Communications Physics*, 2(1), August 2019.

[32] Clayton Crocker. *High Purity Single Photons Entangled with Barium ions for Quantum Networking*. PhD thesis, University of Maryland, College Park, 2018.

[33] Phil Danielson. Desorbing water in vacuum systems: Bakeout or uv? 2001.

[34] M. Day. *Microfabricated Optics for Quantum Control of Trapped Ions*. PhD thesis, University of Bristol, 2018.

[35] Matthew Day. Quantumion splitter waveguide chip operation manual (internal document), 2021.

[36] Yvette de Sereville. Towards dual-isotope entangling gates for trapped-ion quantum computing. Master's thesis, University of Waterloo, 2022.

[37] S. Debnath, N. M. Linke, C. Figgatt, K. A. Landsman, K. Wright, and C. Monroe. Demonstration of a small programmable quantum computer with atomic qubits. *Nature*, 536(7614):63–66, August 2016.

[38] Shantanu Debnath. *A Programmable Five Qubit Quantum Computer Using Trapped Atomic Ions*. PhD thesis, University of Maryland College Park, 2016.

[39] K. Deng, Y. L. Sun, W. H. Yuan, Z. T. Xu, J. Zhang, Z. H. Lu, and J. Luo. A modified model of helical resonator with predictable loaded resonant frequency and q-factor. *Review of Scientific Instruments*, 85(10):104706, October 2014.

[40] X.-L. Deng, D. Porras, and J. I. Cirac. Effective spin quantum phases in systems of trapped ions. *Physical Review A*, 72(6), December 2005.

[41] David Deutsch. Quantum theory, the church-turing principle and the universal quantum computer. *Proceedings of the Royal Society of London. A. Mathematical and Physical Sciences*, 400(1818):97–117, 1985.

[42] M. R. Dietrich, N. Kurz, T. Noel, G. Shu, and B. B. Blinov. Hyperfine and optical barium ion qubits. *Physical Review A*, 81(5), May 2010.

[43] Yimin Ding, Xi Chen, Yao Duan, Haiyang Huang, Lidan Zhang, Shengyuan Chang, Xuexue Guo, and Xingjie Ni. Metasurface-dressed two-dimensional on-chip waveguide for free-space light field manipulation. *ACS Photonics*, 9(2):398–404, February 2022.

[44] M. V. Gurudev Dutt, L. Childress, L. Jiang, E. Togan, J. Maze, F. Jelezko, A. S. Zibrov, P. R. Hemmer, and M. D. Lukin. Quantum register based on individual electronic and nuclear spin qubits in diamond. *Science*, 316(5829):1312–1316, June 2007.

[45] D. Edwards. Methane outgassing from a ti sublimation pump. *Journal of Vacuum Science and Technology*, 17(1):279–281, January 1980.

[46] Laird Nicholas Egan. *Scaling Quantum Computers With Long Chains of Trapped Ions*. PhD thesis, University of Maryland, College Park, 2021.

[47] Christopher J. Foot. *Atomic Physics*. Oxford University Press, 2005.

[48] Austin G. Fowler, Matteo Mariantoni, John M. Martinis, and Andrew N. Cleland. Surface codes: Towards practical large-scale quantum computation. *Physical Review A*, 86(3), September 2012.

[49] J P Gaebler, T R Tan, Y Lin, Y Wan, R Bowler, A C Keith, S Glancy, K Coakley, E Knill, D Leibfried, and D J Wineland. High-fidelity universal gate set for $^9\text{Be}^+$ ion qubits. *Phys. Rev. Lett.*, 117(6):060505, August 2016.

[50] Todd J. Green and Michael J. Biercuk. Phase-modulated decoupling and error suppression in qubit-oscillator systems. *Phys. Rev. Lett.*, 114:120502, Mar 2015.

[51] Noah Greenberg. Vacuum and optical designs for an open-access trapped ion quantum processor. Master's thesis, University of Waterloo, 2020.

[52] Oswald Gröbner. UHV technology. 2004.

[53] S. Halama, T. Dubielzig, N. Orlowski, C. Torkzaban, and C. Ospelkaus. Real-time capable ccd-based individual trapped-ion qubit measurement, 2022.

[54] S. Hannig, L. Pelzer, N. Scharnhorst, J. Kramer, M. Stepanova, Z. T. Xu, N. Spethmann, I. D. Leroux, T. E. Mehlstäubler, and P. O. Schmidt. Towards a transportable aluminium ion quantum logic optical clock. *Review of Scientific Instruments*, 90(5):053204, May 2019.

[55] Aram W. Harrow, Avinatan Hassidim, and Seth Lloyd. Quantum algorithm for linear systems of equations. *Physical Review Letters*, 103(15), oct 2009.

[56] T. P. Harty, D. T. C. Allcock, C. J. Ballance, L. Guidoni, H. A. Janacek, N. M. Linke, D. N. Stacey, and D. M. Lucas. High-fidelity preparation, gates, memory, and readout of a trapped-ion quantum bit. *Physical Review Letters*, 113(22), November 2014.

[57] David Lee Hayes. *Remote and Local Entanglement of Ions using Photons and Phonons*. PhD thesis, University of Maryland, College Park, 2012.

[58] E. Hedlund. The need for more outgassing data of materials for accelerators and storage ring experiments.

[59] D. A. Hite, Y. Colombe, A. C. Wilson, K. R. Brown, U. Warring, R. Jördens, J. D. Jost, K. S. McKay, D. P. Pappas, D. Leibfried, and D. J. Wineland. 100-fold reduction of electric-field noise in an ion trap cleaned with in situ argon-ion-beam bombardment. *Phys. Rev. Lett.*, 109:103001, Sep 2012.

[60] Jonathon P. Home. Quantum science and metrology with mixed-species ion chains. In *Advances In Atomic, Molecular, and Optical Physics*, pages 231–277. Elsevier, 2013.

[61] Ting-Wei Hsu, Wenqi Zhu, Tobias Thiele, Mark O. Brown, Scott B. Papp, Amit Agrawal, and Cindy A. Regal. Single atom trapping in a metasurface lens optical tweezer. 2021.

[62] Kazi Rajibul Islam. *Quantum Simulation of Interacting Spin Models With Trapped Ions*. PhD thesis, University of Maryland, College Park, 2012.

[63] D.F.V. James. Quantum dynamics of cold trapped ions with application to quantum computation. *Applied Physics B: Lasers and Optics*, 66(2):181–190, February 1998.

[64] K G Johnson, J D Wong-Campos, A Restelli, K A Landsman, B Neyenhuis, J Mizrahi, and C Monroe. Active stabilization of ion trap radiofrequency potentials. *Rev. Sci. Instrum.*, 87(5):053110, May 2016.

[65] K. Jousten. Ultrahigh vacuum gauges, 2007.

[66] RATTAKORN KAEWUAM. *Development of an Optical Atomic Clock Based on Trapped Lutetium Ions*. PhD thesis, National University of Singapore, 2020.

[67] D. Kielpinski, C. Monroe, and D. J. Wineland. Architecture for a large-scale ion-trap quantum computer. *Nature*, 417(6890):709–711, June 2002.

[68] K. Kim, M.-S. Chang, S. Korenblit, R. Islam, E. E. Edwards, J. K. Freericks, G.-D. Lin, L.-M. Duan, and C. Monroe. Quantum simulation of frustrated ising spins with trapped ions. *Nature*, 465(7298):590–593, June 2010.

[69] Morten Kjaergaard, Mollie E. Schwartz, Jochen Braumüller, Philip Krantz, Joel I.-J. Wang, Simon Gustavsson, and William D. Oliver. Superconducting qubits: Current state of play. *Annual Review of Condensed Matter Physics*, 11(1):369–395, March 2020.

[70] Jens Koch, Terri M. Yu, Jay Gambetta, A. A. Houck, D. I. Schuster, J. Majer, Alexandre Blais, M. H. Devoret, S. M. Girvin, and R. J. Schoelkopf. Charge-insensitive qubit design derived from the cooper pair box. *Physical Review A*, 76(4), October 2007.

[71] Florian Kranzl, Manoj K. Joshi, Christine Maier, Tiff Brydges, Johannes Franke, Rainer Blatt, and Christian F. Roos. Controlling long ion strings for quantum simulation and precision measurements. *Physical Review A*, 105(5), May 2022.

[72] H Kurisu, K Ishizawa, S Yamamoto, M Hesaka, and Y Saito. Application of titanium materials to vacuum chambers and components. *Journal of Physics: Conference Series*, 100(9):092002, mar 2008.

[73] H Kurisu, K Ishizawa, S Yamamoto, M Hesaka, and Y Saito. Application of titanium materials to vacuum chambers and components. *Journal of Physics: Conference Series*, 100(9):092002, March 2008.

[74] Regina Lechner. *Multi-mode cooling techniques for trapped ions*. PhD thesis, Innsbruck,, 2016.

[75] Regina Lechner, Christine Maier, Cornelius Hempel, Petar Jurcevic, Ben P. Lanyon, Thomas Monz, Michael Brownnutt, Rainer Blatt, and Christian F. Roos. Electromagnetically-induced-transparency ground-state cooling of long ion strings. *Physical Review A*, 93(5), May 2016.

[76] Patricia J. Lee. *Quantum Information Processing with Two Trapped Cadmium Ions*. PhD thesis, University of Maryland, College Park, 2006.

[77] D. Leibfried, R. Blatt, C. Monroe, and D. Wineland. Quantum dynamics of single trapped ions. *Reviews of Modern Physics*, 75(1):281–324, March 2003.

[78] M.-A. Lemonde, S. Meesala, A. Sipahigil, M. J. A. Schuetz, M. D. Lukin, M. Loncar, and P. Rabl. Phonon networks with silicon-vacancy centers in diamond waveguides. *Physical Review Letters*, 120(21), May 2018.

[79] G. Leschhorn, T. Hasegawa, and T. Schaetz. Efficient photo-ionization for barium ion trapping using a dipole-allowed resonant two-photon transition. *Applied Physics B*, 108(1):159–165, June 2012.

[80] Pak Hong Leung, Kevin A. Landsman, Caroline Figgatt, Norbert M. Linke, Christopher Monroe, and Kenneth R. Brown. Robust 2-qubit gates in a linear ion crystal using a frequency-modulated driving force. *Phys. Rev. Lett.*, 120:020501, Jan 2018.

[81] Harry Levine, Alexander Keesling, Giulia Semeghini, Ahmed Omran, Tout T. Wang, Sepehr Ebadi, Hannes Bernien, Markus Greiner, Vladan Vuletić, Hannes Pichler, and Mikhail D. Lukin. Parallel implementation of high-fidelity multiqubit gates with neutral atoms. *Physical Review Letters*, 123(17), October 2019.

[82] Nanxi Li, Chong Pei Ho, Shiyang Zhu, Yuan Hsing Fu, Yao Zhu, and Lennon Yao Ting Lee. Aluminium nitride integrated photonics: a review. *Nanophotonics*, 10(9):2347–2387, jun 2021.

[83] G.-D. Lin, S.-L. Zhu, R. Islam, K. Kim, M.-S. Chang, S. Korenblit, C. Monroe, and L.-M. Duan. Large-scale quantum computation in an anharmonic linear ion trap. *EPL (Europhysics Letters)*, 86(6):60004, June 2009.

[84] Norbert M. Linke, Dmitri Maslov, Martin Roetteler, Shantanu Debnath, Caroline Figgatt, Kevin A. Landsman, Kenneth Wright, and Christopher Monroe. Experimental comparison of two quantum computing architectures. *Proceedings of the National Academy of Sciences*, 114(13):3305–3310, March 2017.

[85] Seth Lloyd, Silvano Garnerone, and Paolo Zanardi. Quantum algorithms for topological and geometric analysis of big data, 2015.

[86] Daniel Loss and David P. DiVincenzo. Quantum computation with quantum dots. *Physical Review A*, 57(1):120–126, January 1998.

[87] W. Macalpine and R. Schildknecht. Coaxial resonators with helical inner conductor. *Proceedings of the IRE*, 47(12):2099–2105, December 1959.

[88] Paolo Manini. Cern accelerator school: Seminar on getter pumps. 2017.

[89] T. A. Manning. *Quantum information processing with trapped ion chains.* PhD thesis, University of Maryland College Park, 2014.

[90] Tom Manovitz, Yotam Shapira, Lior Gazit, Nitzan Akerman, and Roee Ozeri. Trapped-ion quantum computer with robust entangling gates and quantum coherent feedback. *PRX Quantum*, 3(1), March 2022.

[91] Karan K Mehta, Colin D Bruzewicz, Robert McConnell, Rajeev J Ram, Jeremy M Sage, and John Chiaverini. Integrated optical addressing of an ion qubit. *Nat. Nanotechnol.*, 11(12):1066–1070, December 2016.

[92] Karan K Mehta and Rajeev J Ram. Precise and diffraction-limited waveguide-to-free-space focusing gratings. *Sci. Rep.*, 7(1):2019, May 2017.

[93] Karan K Mehta, Chi Zhang, Maciej Malinowski, Thanh-Long Nguyen, Martin Stadler, and Jonathan P Home. Integrated optical multi-ion quantum logic. *Nature*, 586(7830):533–537, October 2020.

[94] Jonathan Albert Mizrahi. *Ultrafast Control of Spin and Motion in Trapped Ions.* PhD thesis, University of Maryland, College Park, 2013.

[95] C. Monroe, D. M. Meekhof, B. E. King, W. M. Itano, and D. J. Wineland. Demonstration of a fundamental quantum logic gate. *Physical Review Letters*, 75(25):4714–4717, 1995.

[96] C. Monroe, R. Raussendorf, A. Ruthven, K. R. Brown, P. Maunz, L.-M. Duan, and J. Kim. Large-scale modular quantum-computer architecture with atomic memory and photonic interconnects. *Physical Review A*, 89(2), February 2014.

[97] Christopher Monroe. Primer on mølmer-sørensen gates in trapped ions, June 2020.

[98] Galan Moody, Volker J Sorger, Daniel J Blumenthal, Paul W Juodawlkis, William Loh, Cheryl Sorace-Agaskar, Alex E Jones, Krishna C Balram, Jonathan C F Matthews, Anthony Laing, Marcelo Davanco, Lin Chang, John E Bowers, Niels Quack, Christophe Galland, Igor Aharonovich, Martin A Wolff, Carsten Schuck, Neil Sinclair, Marko Lončar, Tin Komljenovic, David Weld, Shayan Mookherjea, Sonia Buckley, Marina Radulaski, Stephan Reitzenstein, Benjamin Pingault, Bartholomeus Machielse, Debsuvra Mukhopadhyay, Alexey Akimov, Aleksei Zheltikov, Girish S Agarwal, Kartik Srinivasan, Juanjuan Lu, Hong X Tang, Wentao Jiang, Timothy P

McKenna, Amir H Safavi-Naeini, Stephan Steinhauer, Ali W Elshaari, Val Zwiller, Paul S Davids, Nicholas Martinez, Michael Gehl, John Chiaverini, Karan K Mehta, Jacquiline Romero, Navin B Lingaraju, Andrew M Weiner, Daniel Peace, Robert Cernansky, Mirko Lobino, Eleni Diamanti, Luis Trigo Vidarte, and Ryan M Camacho. 2022 roadmap on integrated quantum photonics. *J. Phys. Photonics*, 4(1):012501, January 2022.

[99] Y. Nakamura, Yu. A. Pashkin, and J. S. Tsai. Coherent control of macroscopic quantum states in a single-cooper-pair box. *Nature*, 398(6730):786–788, 1999.

[100] Yunseong Nam, Jwo-Sy Chen, Neal C. Pisenti, Kenneth Wright, Conor Delaney, Dmitri Maslov, Kenneth R. Brown, Stewart Allen, Jason M. Amini, Joel Apisdorf, Kristin M. Beck, Aleksey Blinov, Vandiver Chaplin, Mika Chmielewski, Coleman Collins, Shantanu Debnath, Kai M. Hudek, Andrew M. Ducore, Matthew Keesan, Sarah M. Kreikemeier, Jonathan Mizrahi, Phil Solomon, Mike Williams, Jaime David Wong-Campos, David Moehring, Christopher Monroe, and Jungsang Kim. Ground-state energy estimation of the water molecule on a trapped-ion quantum computer. *npj Quantum Information*, 6(1), April 2020.

[101] Michael A Nielsen and Isaac L Chuang. *Quantum Computation and Quantum Information*. Cambridge University Press, Cambridge, England, December 2010.

[102] R J Niffenegger, J Stuart, C Sorace-Agaskar, D Kharas, S Bramhavar, C D Bruzewicz, W Loh, R T Maxson, R McConnell, D Reens, G N West, J M Sage, and J Chiaverini. Integrated multi-wavelength control of an ion qubit. *Nature*, 586(7830):538–542, October 2020.

[103] Brando Okolo. 3d printed peek for vacuum technology, 2016.

[104] Steven Matthew Olmschenk. *Quantum Teleportation Between Distant Matter Qubits*. PhD thesis, University of Maryland, College Park, 2009.

[105] R. Ozeri, W. M. Itano, R. B. Blakestad, J. Britton, J. Chiaverini, J. D. Jost, C. Langer, D. Leibfried, R. Reichle, S. Seidelin, J. H. Wesenberg, and D. J. Wineland. Errors in trapped-ion quantum gates due to spontaneous photon scattering. *Physical Review A*, 75(4), April 2007.

[106] G Pagano, P W Hess, H B Kaplan, W L Tan, P Richerme, P Becker, A Kyprianidis, J Zhang, E Birckelbaw, M R Hernandez, Y Wu, and C Monroe. Cryogenic trapped-ion system for large scale quantum simulation. *Quantum Science and Technology*, 4(1):014004, October 2018.

[107] J. M. Pino, J. M. Dreiling, C. Figgatt, J. P. Gaebler, S. A. Moses, M. S. Allman, C. H. Baldwin, M. Foss-Feig, D. Hayes, K. Mayer, C. Ryan-Anderson, and B. Neyenhuis. Demonstration of the trapped-ion quantum CCD computer architecture. *Nature*, 592(7853):209–213, April 2021.

[108] I. Pogorelov, T. Feldker, Ch. D. Marciniak, L. Postler, G. Jacob, O. Krieglsteiner, V. Podlesnic, M. Meth, V. Negnevitsky, M. Stadler, B. Höfer, C. Wächter, K. Lakhmanskiy, R. Blatt, P. Schindler, and T. Monz. Compact ion-trap quantum computing demonstrator. *PRX Quantum*, 2(2), June 2021.

[109] John Preskill. Quantum computing in the NISQ era and beyond. *Quantum*, 2:79, aug 2018.

[110] Mu Qiao, Zhengyang Cai, Ye Wang, Botao Du, Naijun Jin, Wentao Chen, Pengfei Wang, Chunyang Luan, Erfu Gao, Ximo Sun, Haonan Tian, Jingning Zhang, and Kihwan Kim. Observing frustrated quantum magnetism in two-dimensional ion crystals, 2022.

[111] Anthony Ransford, Conrad Roman, Thomas Dellaert, Patrick McMillin, and Wesley C Campbell. Weak dissipation for high-fidelity qubit-state preparation and measurement. *Phys. Rev. A (Coll. Park.)*, 104(6), December 2021.

[112] Melissa C. Revelle. Phoenix and peregrine ion traps, 2020.

[113] Martin Ringbauer, Michael Meth, Lukas Postler, Roman Stricker, Rainer Blatt, Philipp Schindler, and Thomas Monz. A universal qudit quantum processor with trapped ions, 2021.

[114] Robin.materese@nist.gov. Beam splitters/combiners, Jan 2011.

[115] Robin.materese@nist.gov. The second quantum revolution, Apr 2022.

[116] Daniel Rotter. *Quantum feedback and quantum correlation measurements with a single Barium ion*. PhD thesis, Fakultät der Leopold-Franzens-Universität Innsbruck, 2008.

[117] V. M. Schäfer, C. J. Ballance, K. Thirumalai, L. J. Stephenson, T. G. Ballance, A. M. Steane, and D. M. Lucas. Fast quantum logic gates with trapped-ion qubits. *Nature*, 555(7694):75–78, March 2018.

[118] L. Schulz. Sputter-ion pumps.

[119] Makfir Sefa, James A. Fedchak, and Julia Scherschligt. Investigations of medium-temperature heat treatments to achieve low outgassing rates in stainless steel ultra-high vacuum chambers. *Journal of Vacuum Science &amp Technology A: Vacuum, Surfaces, and Films*, 35(4):041601, July 2017.

[120] Crystal Senko. *Dynamics and Excited States of Quantum Many-Body Spin Chains with Trapped Ions*. PhD thesis, University of Maryland, College Park, 2014.

[121] Chung-You Shih. *Holographic Optical Manipulation of Trapped Ions for Quantum Simulation*. PhD thesis, University of Waterloo, 2019.

[122] Chung-You Shih, Sainath Motlakunta, Nikhil Kotibhaskar, Manas Sajjan, Roland Hablützel, and Rajibul Islam. Reprogrammable and high-precision holographic optical addressing of trapped ions for scalable quantum control. *npj Quantum Information*, 7(1), April 2021.

[123] Peter W. Shor. Fault-tolerant quantum computation, 1996.

[124] Peter W. Shor. Polynomial-time algorithms for prime factorization and discrete logarithms on a quantum computer. *SIAM Journal on Computing*, 26(5):1484–1509, 1997.

[125] I Siemers, M Schubert, R Blatt, W Neuhauser, and P. E Toschek. The "trapped state" of a trapped ion-line shifts and shape. *Europhysics Letters (EPL)*, 18(2):139–144, feb 1992.

[126] J. D. Siverns, L. R. Simkins, S. Weidt, and W. K. Hensinger. On the application of radio frequency voltages to ion traps via helical resonators. *Applied Physics B*, 107(4):921–934, January 2012.

[127] Anders Sørensen and Klaus Mølmer. Quantum computation with ions in thermal motion. *Physical Review Letters*, 82(9):1971–1974, March 1999.

[128] K. Sosnova, A. Carter, and C. Monroe. Character of motional modes for entanglement and sympathetic cooling of mixed-species trapped-ion chains. *Physical Review A*, 103(1), Jan 2021.

[129] Ksenia Sosnova. *Mixed-Species Ion Chains for Quantum Networks*. PhD thesis, University of Maryland, College Park, 2020.

[130] F Splatt, M Harlander, M Brownnutt, F Zähringer, R Blatt, and W Hänsel. Deterministic reordering of $^{40}\mathrm{Ca}^{+}$ions in a linear segmented paul trap. *New Journal of Physics*, 11(10):103008, October 2009.

[131] A. Steane. The ion trap quantum information processor. *Applied Physics B: Lasers and Optics*, 64(6):623–643, June 1997.

[132] D. A. Steck. Rubidium 87 d line data, 2001.

[133] Yi Hong Teoh. Machine learning and optimization techniques for trapped-ion quantum simulators. Master's thesis, University of Waterloo, 2020.

[134] Yi Hong Teoh, Marina Drygala, Roger G Melko, and Rajibul Islam. Machine learning design of a trapped-ion quantum spin simulator. *Quantum Science and Technology*, 5(2):024001, January 2020.

[135] Gregor Thalhammer, Richard W. Bowman, Gordon D. Love, Miles J. Padgett, and Monika Ritsch-Marte. Speeding up liquid crystal SLMs using overdrive with phase change reduction. *Optics Express*, 21(2):1779, January 2013.

[136] S L Todaro, V B Verma, K C McCormick, D T C Allcock, R P Mirin, D J Wineland, S W Nam, A C Wilson, D Leibfried, and D H Slichter. State readout of a trapped ion qubit using a trap-integrated superconducting photon detector. *Phys. Rev. Lett.*, 126(1):010501, January 2021.

[137] Nikolay Videnov. Optical design for an open access trapped ion quantum processor. Master's thesis, University of Waterloo, 2021.

[138] Pengfei Wang, Chun-Yang Luan, Mu Qiao, Mark Um, Junhua Zhang, Ye Wang, Xiao Yuan, Mile Gu, Jingning Zhang, and Kihwan Kim. Single ion qubit with estimated coherence time exceeding one hour. *Nature Communications*, 12(1), January 2021.

[139] Ye Wang, Mark Um, Junhua Zhang, Shuoming An, Ming Lyu, Jing-Ning Zhang, L.-M. Duan, Dahyun Yum, and Kihwan Kim. Single-qubit quantum memory exceeding ten-minute coherence time. *Nature Photonics*, 11(10):646–650, September 2017.

[140] Brendan M. White, Pei Jiang Low, Yvette de Sereville, Matthew L. Day, Noah Greenberg, Richard Rademacher, and Crystal Senko. Isotope-selective laser ablation ion-trap loading of $^{137}\mathrm{Ba}^{+}$ using a BaCl_2 target. *Physical Review A*, 105(3), March 2022.

[141] Joshua M. Wilson, Julia N. Tilles, Raymond A. Haltli, Eric Ou, Matthew G. Blain, Susan M. Clark, and Melissa C. Revelle. iin situ/i detection of RF breakdown on microfabricated surface ion traps. *Journal of Applied Physics*, 131(13):134401, apr 2022.

[142] D. J. Wineland, M. Barrett, J. Britton, J. Chiaverini, B. DeMarco, W. M. Itano, B. Jelenković, C. Langer, D. Leibfried, V. Meyer, T. Rosenband, and T. Schätz. Quantum information processing with trapped ions. *Philosophical Transactions of the Royal Society of London. Series A: Mathematical, Physical and Engineering Sciences*, 361(1808):1349–1361, July 2003.

[143] D.J. Wineland, C. Monroe, W.M. Itano, D. Leibfried, B.E. King, and D.M. Meekhof. Experimental issues in coherent quantum-state manipulation of trapped atomic ions. *Journal of Research of the National Institute of Standards and Technology*, 103(3):259, May 1998.

[144] K. Wright, K. M. Beck, S. Debnath, J. M. Amini, Y. Nam, N. Grzesiak, J.-S. Chen, N. C. Pisenti, M. Chmielewski, C. Collins, K. M. Hudek, J. Mizrahi, J. D. Wong-Campos, S. Allen, J. Apisdorf, P. Solomon, M. Williams, A. M. Ducore, A. Blinov, S. M. Kreikemeier, V. Chaplin, M. Keesan, C. Monroe, and J. Kim. Benchmarking an 11-qubit quantum computer. *Nature Communications*, 10(1), November 2019.

[145] Hao Wu, Michael Mills, Elizabeth West, Michael C Heaven, and Eric R Hudson. Increase of the barium ion-trap lifetime via photodissociation. *Phys. Rev. A (Coll. Park.)*, 104(6), December 2021.

[146] Chi Xiong, Wolfram H P Pernice, Xiankai Sun, Carsten Schuck, King Y Fong, and Hong X Tang. Aluminum nitride as a new material for chip-scale optomechanics and nonlinear optics. *New Journal of Physics*, 14(9):095014, sep 2012.

[147] Alexander Yulaev, Wenqi Zhu, Cheng Zhang, Daron A Westly, Henri J Lezec, Amit Agrawal, and Vladimir Aksyuk. Metasurface-integrated photonic platform for versatile free-space beam projection with polarization control. *ACS Photonics*, 6(11):2902–2909, November 2019.

[148] Jiajia Zhou. *Building A Magnesium Ion Trap For Quantum Computation.* PhD thesis, McMaster University, 2007.

[149] Lingxiao Zhu, Xuan Liu, Basudeb Sain, Mengyao Wang, Christian Schlickriede, Yutao Tang, Junhong Deng, Kingfai Li, Jun Yang, Michael Holynski, Shuang Zhang,

Thomas Zentgraf, Kai Bongs, Yu-Hung Lien, and Guixin Li. A dielectric metasurface optical chip for the generation of cold atoms. *Sci. Adv.*, 6(31), July 2020.